THE APPLICATION OF SYNTHETIC APERTURE RADAR FOR THE DETECTION AND MAPPING OF SMALL-SCALE MINING IN GHANA

By

MARIA GABRIELLE DENNER

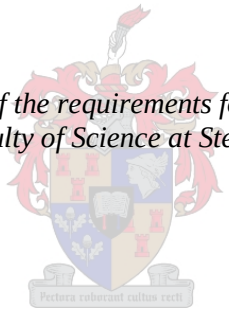

Thesis presented in fulfilment of the requirements for the degree of Master of Geoinformatics in the Faculty of Science at Stellenbosch University.

Supervisor: Dr Jaco Kemp

December 2020

DECLARATION

By submitting this thesis electronically, I declare that the entirety of the work contained therein is my own, original work, that I am the sole author thereof (save to the extent explicitly otherwise stated), that reproduction and publication thereof by Stellenbosch University will not infringe any third party rights and that I have not previously in its entirety or in part submitted it for obtaining any qualification.

December 2020

SUMMARY

Artisanal and small-scale mining (SSM) is a cause of major environmental concern in developing countries. In Ghana, SSM is a mixture of legal and illegal operations where illegal mining is referred to as “galamsey”. Earth observation techniques can assist local governments in regulating SSM activities by providing specific spatial information on the whereabouts of SSM mines. The tropical climate in Ghana, however, hinders the regular flow of useful optical imagery due to a high percentage of cloud cover for most parts of the year. Synthetic aperture radar (SAR) can overcome this limitation. The study area includes a portion of the Ofin River near the mining town of Obuasi, Ghana. The area is tropical in climate, rural and dominated by forests.

This study aims to assess the accuracy and reliability of applying SAR for the detection and mapping of small-scale mining in Ghana with classification and change detection analysis. A literature review on remote sensing and image processing literature was conducted. The satellite imagery collected for the study included single-date C-band Sentinel-1, a time series of Sentinel-1 and a single-date X-band KompSAT-5 image for the SAR analysis with Sentinel-2 and Landsat-8 imagery as ground truth datasets. Classification analysis was conducted in two experiments which included the analysis of two classification schemes, i.e. multi-class- and a binary-water classification scheme. The first experiment assessed the accuracy of random forest classification applied to single-date Sentinel-1, KompSAT-5 and multi-temporally filtered Sentinel-1 databases. The second experiment was a comparison of five machine learning supervised classification methods applied to the multi-temporally filtered Sentinel-1 database. The potential of change detection on Sentinel-1 time series data was analysed in the third experiment for the detection of SSM. Image differencing was applied and two threshold methods were tested for producing the most accurate change maps.

The classification with the object-based image analysis approach was successful in classifying water bodies associated with SSM. The multi-temporally filtered Sentinel-1 dataset was the most reliable with kappa coefficients at 0.65 and 0.82 for the multi-class classification scheme and binary-water classification scheme respectively. The single-date Sentinel-1 dataset has the highest overall accuracy at 90.93% for the binary water classification scheme. The KompSAT-5 dataset only achieved the lowest accuracy at an overall accuracy of 80.61% and a kappa coefficient of 0.61 for the binary-water classification scheme. The results of the change detection analysis indicated that the Sentinel-1 imagery was able to detect and map SSM. The change detection analysis also showed the potential of discerning active from abandoned mines, but this has to be further investigated.

In conclusion, SAR can detect illegal mining activity in tropical areas such as Ghana when focussing on the SSM activities surrounding rivers and the use of high-resolution commercial imagery is not necessary. The change detection analysis detected SSM where the classification methods only detected water bodies associated with SSM. Further research includes exploring the use of thresholding for the binary-water classification analysis, refining the change detection technique by applying segmentation and machine learning to create the change maps.

KEYWORDS

Small-scale mining, SAR, galamsey, machine learning, OBIA, classification, change detection, remote sensing, earth observation.

OPSOMMING

Ambags- en kleinskaalse mynbou (SSM) veroorsaak groot kommer oor die negatiewe impak daarvan in ontwikkelende lande. In Ghana, kom SSM voor as ‘n mengsel van wettige en onwettige bedrywighede. Die onwettige mynbou word in Ghana “galamsey” genoem. Aardwaarnmingstegnieke kan spesifieke ruimtelike inligting van die plekke waar SSM bedrywighede plaasvind bied om plaaslike regerings te help om die SSM aktiwiteite te reguleer. Die hoë persentasie van wolkbedekking wat in Ghana voorkom vir groot dele van die jaar, as gevolg van Ghana se tropiese klimaat, verhoed dat gereelde bruikbare optiese beelde beskikbaar is. Die gebruik van sintetiese apertuur radar (SAR) kan hierdie limitasie oorkom. Die studie gebied sluit ‘n deel van die Ofin Rivier in wat naby aan die myndorp Obuasie, Ghana geleë is. Die gebied het ‘n tropiese klimaat en is in ‘n landelike gebied wat oorheers word met woude.

Die doel van die studie is om die akkuraatheid en betroubaarheid van SAR toe met betrekking tot klassifikasie en verandering-opsporing te assesseer vir die opsporing en kartering van SSM. ‘n Literatuuroorsig op afstandswaarneming en beeldverwerking was gedoen. Die satellietbeelde wat ingesamel is sluit ‘n enkel-datum C-band Sentinel-1, ‘n tydreeks van Sentinel-1 en ‘n enkel-datum X-band KompSAT-5 beeld in vir die SAR analise saam met Sentinel-2 en Landsat-8 beelde wat as grondwaarheid gebruik is. Klassifikasie analise was uitgevoer in twee eksperimente wat die analise van twee klassifikasie skemas ingesluit het, naamlik multi-klas- en binêre-water klassifikasie skemas. Die eerste eksperiment het die akkuraatheid van ewikansige woud toegepas op die enkel-datum Sentinel-1, KomSAT-5 en multi-temporaal gefilterde Sentinel-1 databasisse geassesseer. Die tweede eksperiment was ‘n vergelyking tussen vyf masjienleer toesig-klassifikasie metodes wat toegepas was op die multi-temporaal gefiterde Sentinel-1 databasis. Die potensiaal van verandering-opsporing op die Sentinel-1 tydreeks data om SSM op te spoor was geanaliseer in die derde eksperiment. Beeldaftrekking was toegepas en twee drumpel metodes was getoets vir die akkuraatste verandering kaarte.

Die resultate toon aan dat die klassifikasie, met die objekgebaseerde beeldanalise benadering, suksesvol was om die waterliggame wat met SSM geassosieer word te klassifiseer. Die multi-temporaal gefilterde Sentinel-1 datastel was die mees betroubare met kappa koëffisiënte van 0.65 en 0.82 vir die multi-klas klassifikasie skema en die binêre-water klassifikasie skema onderskeidelik. Die enkel-datum Sentinel-1 datastel het die hoogste algehele akkuraatheid van 90.93% vir die binêre-water klassifikasie skema behaal. Die resultate van die verandering-opsporing analise toon dat die Sentinel-1 beelde die SSM kon opspoor en karteer. Die verandering-opsporing het ook gewys dat daar potensiaal is om die aktiewe en die verlate myne van mekaar te kan onderskei, maar dié benodig verdere ondersoek.

Die samevatting is dat SAR onwettige mynbou aktiwiteite in ‘n tropiese gebied soos Ghana kan opspoor en dat die gebruik van hoë-resolusie kommersiële beelde nie nodig is nie. Die verandering-opsporing analise het SSM opgespoor waar die klassifikasie metodes net die water wat geassosieer word met SSM kon opspoor. Verdere navorsing sluit die ondersoek van die gebruik van drempeltegnieke vir die binêre-water klassifikasie in, en om die verandering-opsporing te verbeter deur segmentering en masjienleer toe te pas om die verandering-kaarte te maak.

TREFWOORDE

Ambags- en kleinskaalse mynbou, SAR, galamsey, masjienleer, OBIA, klassifikasie, verandering-opsporing, afstandswaarneming.

ACKNOWLEDGEMENTS

I would sincerely like to thank:

- My supervisor, Dr Jaco Kemp for his continual guidance, support and encouragement;
- My boyfriend, for continual encouragement, love and support;
- My parents for affording me the opportunity to study, and their love and support;
- Space Advisory Company for the grant for my first year of study;
- The Council for Geoscience for the part-time bursary for my second year of study as well as the funding for my trip in presenting a poster on the work of this thesis at the Living Planet Symposium 2019 in Milan;
- Dr Janine Cole and Dr Patrick Cole for their guidance and support at the Council for Geoscience;
- SI-Imaging for providing me with the KompSAT-5 data.

CONTENTS

TABLES

FIGURES

APPENDICES

LIST OF ACRONYMS AND ABBREVIATIONS

ASM	Angular second moment
CSV	Comma-separated values
C-SVM	Kernel support vector machine
dB	Decibel
DEM	Digital elevation model
DT	Decision trees
EC	Error of commission
EMR	Electromagnetic radiation
ENVI	Environment for visualising images
EO	Error of omission
ES Standard	Enhanced Standard
ESA	European Space Agency
GLCM	Grey-level co-occurrence matrix
GLDV	Grey level difference vectors
GRD	Ground range detected
IDAN	Intensity driven adaptive-neighbourhood
IW	Interferometric Wide Swath
JERS-1	Japanese Earth Resource Satellite-1
K5	KompSAT-5
KNN	K-nearest neighbour
KompSAT	Korea Multi-Purpose SATellite
MRS	Multiresolution segmentation
NDI	Normalized difference index
OA	Overall accuracy
OBIA	Object-based image analysis
PA	Producer’s accuracy
PBIA	Pixel-based image analysis
RBF	Radial basis function
RF	Random forest
RGB	Red-green-blue
ROC	Receiver Operating Characteristic
S1	Sentinel-1

S1-MT	Sentinel-1 multitemporal filtered
S1-omnibus	Sentinel-1-omnibus
S1TBX	Sentinel-1 toolbox
SAR	Synthetic aperture radar
SLC	Single look complex
SNAP	Sentinel Application Platform
SSM	Small-scale mining
SVM	Support vector machine
UA	User’s accuracy
VH	Vertical transmit, horizontal receive
VV	Vertical transmit, vertical receive

1 CHAPTER 1: INTRODUCTION

Small-scale mining has devastating impacts on the natural environment when not regulated properly and many small-scale mining operations are operated illegally. Small-scale mining is a low cost, labour-intensive method of mining in areas where gold is easily accessible such as on the river banks where alluvial gold deposits can be found. The application of earth observation in detecting these mining sites is explored in this study to potentially assist governments in mitigating the effects of small-scale mining.

1.1 SMALL-SCALE MINING AND ITS IMPACT

Artisanal and small-scale mining (SSM) is described by Hilson (2016) as a labour-intensive means of the extraction and processing of minerals with limited technological use and is commonly occurring in developing countries. In Ghana, a mining operation is classified as small-scale mining when mining operations are low-cost, labour-intensive that can be operated by either an individual or a group of persons not exceeding nine (GhanaLegal 2018). Mining operations are only allowed a certain size claim and the use of explosives is not permitted (Aryee, Ntibery & Atorkui 2003; GhanaLegal 2018). For this study, artisanal and small-scale mining will only be referred to as small-scale mining (SSM) as these terms are used interchangeably in Ghana (Aubynn 2009; Mantey et al. 2017).

The mining of gold in the Gold Coast has taken place since the fourth century (Gbireh, Cobblah & Suglo 2007). Indigenous miners were the only mining operators until the British colonial establishment banned SSM in 1905. Regardless of the authorities' decision to declare SSM illegal, the indigenous miners still continued their operations (Gbireh, Cobblah & Suglo 2007). The Government of Ghana formalised the SSM sector by the end of the 1980s after recognising the economic significance of the SSM sector (Hilson 2001; Yankson & Gough 2019) but still treated the industry as an informal sector (Hilson 2016). The mining policy frameworks have undergone various modifications in the attempt to attract foreign investment but were unsuccessful until 1986 when the Minerals and Mining Law was established (Gbireh, Cobblah & Suglo 2007; GhanaLegal 2018). Up until the formalization of the SSM sector indigenous miners received little to no support from the government and regulations and the control of the operations of small-scale miners were practically inactive (Hilson 2001). The failure to regulate these laws has had a negative impact on the hydrosphere, land cover, biodiversity, atmosphere, and people in gold mining regions (Aryee, Ntibery & Atorkui 2003; Mantey et al. 2017; Owusu-Koranteng & Owusu-Koranteng 2017). The

spatial distribution patterns of SSM have to be understood so that a flexible solution to a new formalization strategy can be created (Yankson & Gough, 2019).

"Galamsey" is a term commonly used to describe the illegal mining activity in Ghana. Mantey et al. (2017) and Owusu-Nimo et al. (2018) suggest that galamsey operations are an illegal or unregulated form of SSM and processing of gold that lies at or below soil and water surfaces in Ghana. Galamsey operations have historically only been associated with simple tools and manual labour (Aryee, Ntibery & Atorkui 2003; Owusu & Dwomoh 2012) but the use of mechanised equipment like excavators have recently also come into play (Emmanuel O 2013; Mantey et al. 2017) most probably due to the influx of foreign nationals that changed the operational dynamics of galamsey operations (Mantey et al. 2017). The precious minerals are gathered discreetly and sold in contravention of state laws (Aubynn 2009; Mantey et al. 2017). Galamseyers also do not pay tax, many mines are in delicate or prohibited areas and often human safety is put at risk (Crawford et al. 2015; Today Newspaper 2016; Daily Graphic 2018; Owusu-Nimo et al. 2018).

The majority of the gold in Ghana originate from the rocks of the Birimian Supergroup and the Tarkwaian Group (Oberthür et al. 1997; Smith, Henry & Frost-Killian 2016). The gold mined by the galamsey operations is mostly found in the placer gold deposits that are also known as alluvial gold deposits (Hilson 2001). Placer deposits formed due to a series of erosional events, caused by the workings of water, which was accelerated by Ghana's tropical climate (Smith, Henry & Frost-Killian 2016), that transported the gold down the slopes of the Birimian- and Tarkwaian rocks through river channels and deposited the gold downstream. Large deposits of gold are found along with the alluvial formations of the major rivers in Ghana such as the Ofin, Pra, and Birim rivers (Hilson 2001). Some of these alluvial formations include terraces, floodplains, channels and river beds (Hilson 2001). Therefore, the major mining operations, large-scale and small-scale are found along these rivers concentrating in the lower Western sections of Ghana.

1.2 REMOTE SENSING OF SMALL-SCALE MINING

Galamsey operations are generally located in remote locations such as forests, farmlands and community settlements (Hilson 2001; Mantey et al. 2017). Attempts have been made to better understand the spatial distribution patterns of galamsey activities by Mantey et al. (2017) and Owusu-Nimo et al. (2018). However, their techniques primarily rely on ground surveys based on interviews to gather information regarding SSM in Ghana (Yankson & Gough, 2019). Ground surveys are expensive and dangerous due to the nature of the SSM operations. Remote sensing makes it possible to monitor the activities in these remote locations. To date, limited studies have

been done that utilises remote sensing techniques to monitor SSM (e.g. Almeida-filho & Shimabukuro 2000; Asner et al. 2013; Kranz, Lang & Schoepfer 2017).

One of the challenges in using remote sensing for SSM mapping is that many of the SSM operations take place in countries with tropical climates such as Ghana and Peru. Southern Ghana specifically, is classified as tropical and prolonged cloud cover exists throughout the year (GhanaWeb 2018), therefore, the amount of usable optical imagery is restricted. However, with the launch of the Copernicus Sentinel Program free remote sensing data such as Synthetic Aperture Radar (SAR) Sentinel-1 is now available. SAR is able to image through clouds(Mansourpour, Rajabi & Blais 2006) and regular usable data can now be used to assess the potential of creating an effective monitoring system. A reliable system that can monitor SSM is important because the information can assist with regulations and environmental rehabilitation of the areas most affected by these operations.

Remote sensing approaches that have the potential of detecting SSM include image classification with machine learning and change detection. Studies that utilised classification for the mapping of deforestation in tropical areas such as Asner et al. (2013) and Kranz, Lang & Schoepfer (2017) could add value to the detecting SSM. An example of a change detection approach that may assist in detecting SSM is related to flood monitoring with SAR such as the study done by Schlaffer et al. (2015), however, other studies that use thresholding for inundation mapping, such as Hess et al. (2003) and Shen et al. (2019) could also be related to SSM detection.

1.3 PROBLEM FORMULATION

The SSM operations that have taken place over the years have left their footprint in Ghana. The nature of the SSM operations has devastating environmental impacts and it is believed that almost every major waterbody has been affected either directly or indirectly (Aubynn 2009; Alhassan 2014; Mantey et al. 2017). The galamsey miners tend to leave behind many wastelands in the form of pits flooded with water, deforested lands and polluted water bodies (GhanaWeb 2016; Owusu-Nimo et al. 2018), which is hazardous to the local people, livestock and wildlife. Accessing SSM sites is difficult due to their remote locations and extremely dangerous (Asner et al. 2013; Owusu-Nimo et al. 2018).

Remote sensing provides a way to monitor such remote locations on a regular basis, but the use of optical imagery is restricted because of the tropical climate of Southern Ghana. Snapir, Simms & Waine (2017) who attempted to map the expanding areas of galamsey had difficulty in obtaining cloud-free imagery to evaluate change detection. They only found one cloud-free Landsat-8 image and was unable to find suitable Landsat images for multi-temporally compositing for their study

in Ghana. The effective monitoring of such large-scale unregulated mining activity requires a continuous supply of data that is available year-round and as well as during night time.

SAR images present a solution due to the active nature of SAR sensors that emit microwaves which can penetrate through clouds and also sense during the night-time (Mansourpour, Rajabi & Blais 2006; Joshi et al. 2016; Reiche et al. 2018). Except for one recently published study by Forkuor, Ullmann & Griesbeck (2020), SAR has not yet been considered for the mapping and monitoring of SSM in Ghana. SAR can provide valuable insights into the specific locations of SSM and the growth rate of galamsey throughout the year. Questions such as 'in which seasons SSM is most active?' have not yet been answered. Having an uninterrupted supply of usable, easily obtainable imagery, as provided by Sentinel-1, could provide the government with strategic information to improve regulation efforts to address the issues associated with galamsey (Mantey et al. 2017; Owusu-Nimo et al. 2018).

SSM sites around rivers typically comprise of extensive, intermixed areas of bare soil and water pools from the mining process (Asner et al. 2013). A typical pool of water, where the mining process takes place, is about 20 m in diameter which challenges the spatial resolution limits of Sentinel-1. However, using multi-date imagery often produces more accurate results than single-date imagery (Asner et al. 2013). The application of multi-temporally filtering of SAR for monitoring SSM has not yet been tested. SAR flood monitoring also provides insight into mapping the water pools of the alluvial SSM sites with change detection (e.g. Schlaffer et al. 2015, 2017).

Different machine learning classifiers have not yet been compared for the classification of SSM with SAR imagery. Classifying SAR imagery is more challenging than classifying optical imagery because ground features are harder to distinguish with the human eye than that which can be seen in optical imagery. Knowing which classifier produces the most accurate and reliable results is important for an effective monitoring system.

Taking into consideration which remote sensing methods and imagery has been used for the mapping of small-scale mining the following research questions were formulated:

1. How do different SAR sensors compare for the mapping of SSM when applying classification?
2. How does single-product speckle filtered SAR compare with multi-temporally filtered SAR when applying classification?
3. Which classification algorithm is best suited for the mapping of SSM with SAR imagery?
4. Can change detection with SAR time-series data detect SSM?

1.4 AIM AND OBJECTIVES

The aim of this study is to assess the accuracy and reliability of applying SAR for the detection and mapping of small-scale mining in Ghana.

To achieve the research aim, the following objectives have been set:

1. Review the remote sensing and image processing literature to assess whether these approaches can be used for small-scale mining detection and mapping.
2. Collect and acquire appropriate satellite imagery for the selected study area as well as training and reference data.
3. Determine the accuracy and reliability of random forest classification applied to C-band Sentinel-1 single-date compared to X-band KompSAT-5 single-date images, for detecting small-scale mines.
4. Determine the influence of multi-temporally filtering on the accuracy and reliability of random forest classification applied to Sentinel-1 imagery, for detecting small-scale mines.
5. Determine which classification algorithms are the most effective for detecting small-scale mining, with multi-temporally filtered Sentinel-1 imagery.
6. Analyse the potential of change detection on Sentinel-1 time series data for the detection of small-scale mines.

1.5 METHODOLOGY AND RESEARCH DESIGN

An overview of the research design is presented in Figure 1.1. This study follows an empirical approach using primary quantitative data to achieve the objectives listed in Section 1.4. Data acquisition comprises of multiple Sentinel-1 images and one KompSAT-5 image. Sentinel-1 is freely available through the Copernicus Open Access Hub and the KompSAT-5 image was sponsored by SI-Imaging. For ground truth validation open access Sentinel-2 and Landsat-8 imagery were used.

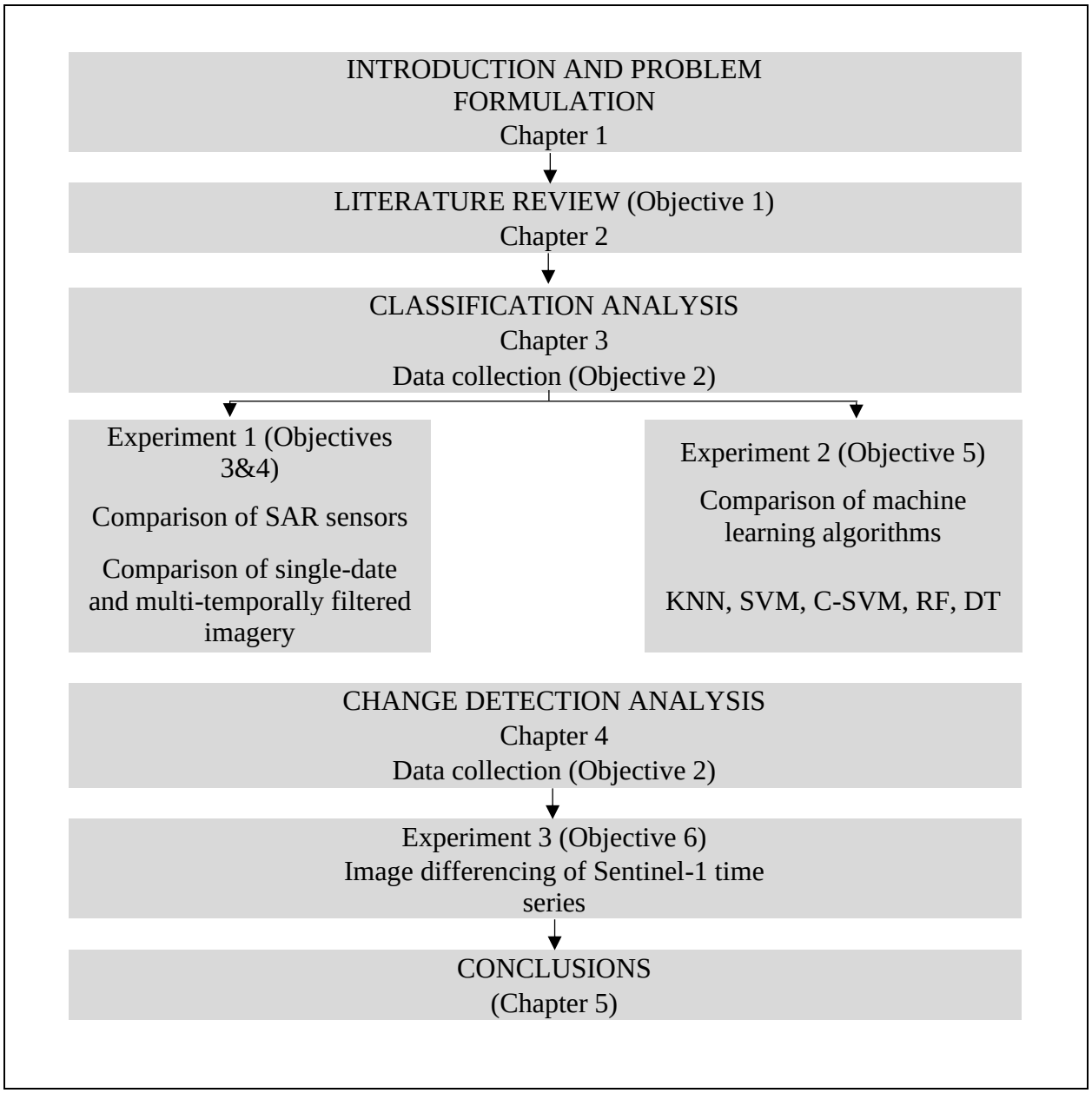

Figure 1.1 The research design.

The methods were split into two sections where the first is classification and the second is change detection. The classification experiments were done in Experiments 1 and 2 and the change detection experiments in Experiment 3. Experiment 1 addressed Objectives 3 and 4 by comparing three datasets. The three datasets were single-date Sentinel-1, single-date KompSAT-5 and multi-temporally filtered Sentinel-1. Experiment 1 followed an object-based image analysis (OBIA) approach and the random forest classifier was used. Experiment 2 addressed Objective 5 where different machine learning algorithms were compared. The machine learning classification algorithms were decision trees (DT), random forest (RF), support vector machine (SVM), kernel support vector machine (C-SVM), and k-nearest neighbour (KNN). The same object-based approach was applied to Experiment 2. The accuracy and reliability of the classification methods were assessed using statistics derived from confusion matrices. Experiment 3 addressed Objective 6 by analysing the potential for change detection to detect SSM. A simple image differencing method was used for change detection. The accuracy assessment for Experiment 3 was performed using the same method as in Experiments 1 and 2, i.e. with the use of confusion matrices.

1.6 STUDY SITE

The study area comprises of the footprint of the KompSAT-5 image over the Ofin River near the town of Obuasi, Ghana (Figure 1.2). Obuasi is an old mining urban centre and the principal mining settlement in Ghana (Yankson & Gough 2019).

The study area is rural and dominated by forests. The absence of large buildings in the scattered rural settlements is beneficial for remote sensing with SAR since the buildings will not interfere with the radar signal. Buildings produce a double-bounce effect that reflects the microwave energy back to the sensor very strongly. Southern Ghana has a tropical climate with daytime temperatures ranging between 25 to 35 degrees Celsius (World weather & climate information 2019). The most rainfall occurs between July and September and the average annual rainfall 736.6mm (GhanaWeb 2019). Figure 1.3 shows the footprints of all the satellite imagery used in this study. The largest footprint is that of Sentinel-1. The KompSAT-5 image falls completely within all of the satellite imagery footprints and was therefore used as the reference for the study area.

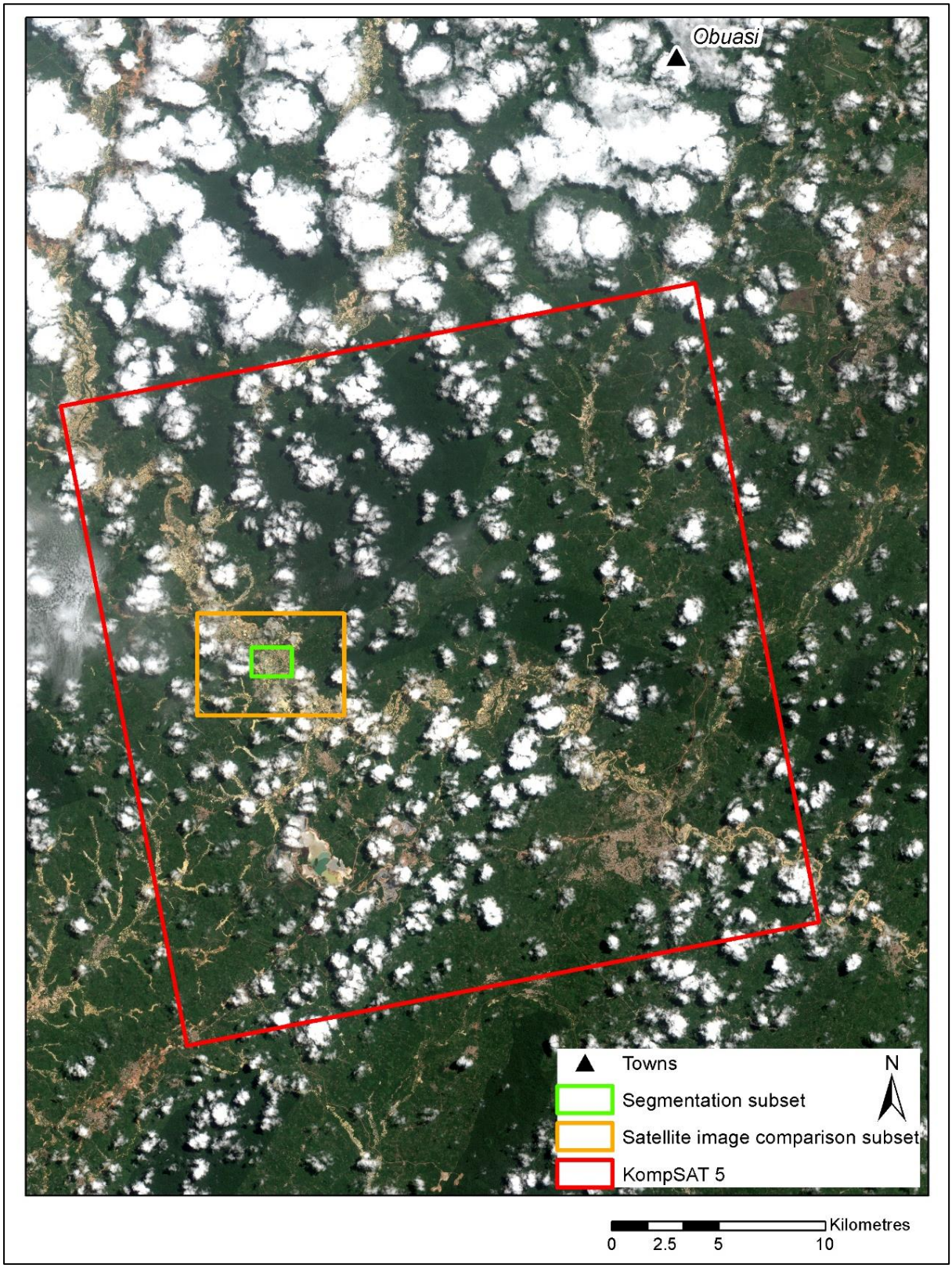

Figure 1.2 The study area is shown as the KompSAT-5 image footprint overlain on Sentinel-2 true colour image.

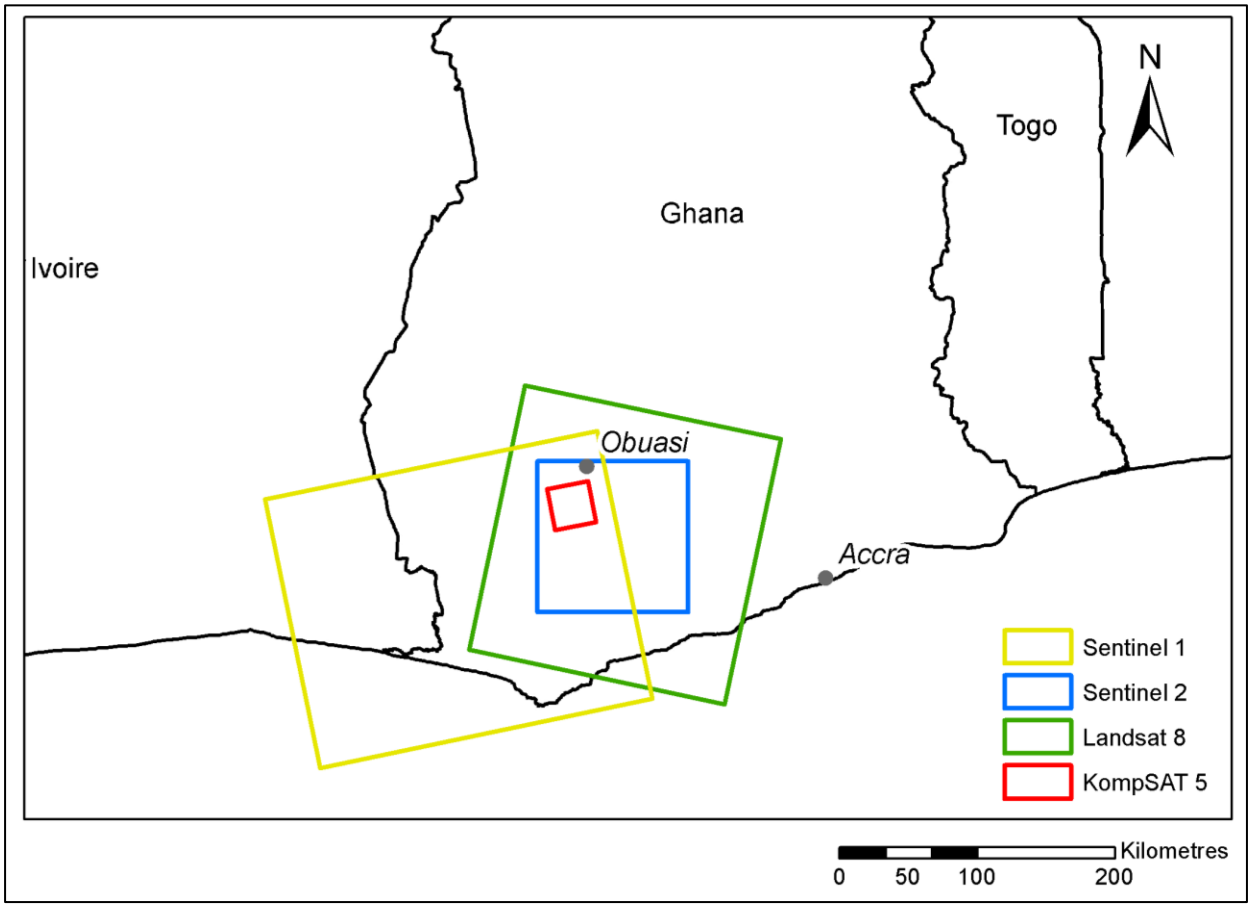

Figure 1.3 The footprints of the satellite imagery used in this study. All of the imagery was cropped to the KompSAT-5 footprint that delineates the study area.

1.7 STRUCTURE OF THE THESIS

The remainder of the thesis is structured as follows: Chapter 2 provides an overview of the literature. Chapter 3 consists of the evaluation of the classification analysis. Here the data acquisition, methods, results and discussion of Experiments 1 and 2 are discussed that addresses Objectives 3 and 4. Chapter 4 is the data acquisition, methods, results and discussion of the change detection analysis in Experiment 3 that addressed Objective 5. In Chapter 5 the research is evaluated by revisiting the aim and objectives, drawing conclusions and giving recommendations for future work.

2 CHAPTER 2: LITERATURE REVIEW

This chapter provides an overview of small-scale mining, and how remote sensing and image processing have been used in the mapping and detection thereof. First, a review of how remote sensing techniques have been used to monitor illegal mining activities is done. The backscatter properties of synthetic aperture radar and the importance of pre-processing is discussed next. Then image processing methods of classification and change detection is explained. In terms of the former, the focus is placed on feature extraction and object-based image analysis for the training of the classifiers. In terms of the latter, image differencing and the use of thresholds is discussed. The chapter concludes with a summary of the literature review.

2.1 SMALL-SCALE MINING AND GALAMSEY

Small-scale mining (SSM) is operated illegally in many countries (Teschner 2012) including Ghana where this illegal activity is referred to as “galamsey” (Hilson 2016; Mantey et al. 2017; Snapir, Simms & Waine 2017; Owusu-Nimo et al. 2018). SSM causes significant destruction because mining mostly takes place on the surface (Snapir, Simms & Waine 2017). The environmental destruction is in the form of deforestation, the removal of soil, and the diversion and sedimentation of rivers, affecting nearly every water body in their perimeter (Kusimi 2008; Aubynn 2009; Asner et al. 2013; Alhassan 2014; Mantey et al. 2017; Snapir, Simms & Waine 2017). Significant mercury pollution also takes place which contaminates the soil and rivers (Serfor-Armah et al. 2004) and mercury contamination has also been found in domestic homes (Gyamfi et al. 2020).

Galamsey operations are generally located in remote locations, forests, farmlands as well as community settlements (Hilson 2001; Mantey et al. 2017). Owusu-Nimo et al. (2018) noted that galamsey operations that are located in community settlements can take place adjacent to schools, churches and residential houses. Three crucial aspects dictate the positioning of galamsey mining and processing operations i.e. the ore grade, the nature of the operation and the availability of supporting resources (Andrew 2003; Mantey et al. 2017). Due to the lack of law enforcement and regulation on the SSM sector over the years (Hilson 2001; Mantey et al. 2017; Owusu-Nimo et al. 2018), SSM and galamsey operations have increased dramatically and are associated with violence and a high level of crime (Alhassan 2014; Micklethwaite 2016; Owusu-Nimo et al. 2018). Snapir, Simms & Waine (2017) have found that the galamsey activity has more than tripled between 2011 and 2015 in the cocoa region of Ghana. The total area of galamsey in the cocoa growing area in Southern Ghana in 2013 was 27,839 ha with an impact zone of 551,496 ha.

The most recent studies of galamsey operations have narrowed into the specifics of the types of galamsey operations taking place to gain a better understanding of the operational dynamics that may assist in the regulation attempts by the Ghanaian Government (Mantey et al. 2017; Owusu-Nimo et al. 2018). Galamsey has been categorised into alluvial, underground mining, mill house, chamfi or surface operations, and pilfering mining (Mantey et al. 2017) where the most destructive of the galamsey types to the environment is the alluvial galamsey. For an exhaustive discussion on various types of galamsey, the reader is referred to Mantey et al. (2017). Mantey et al. (2017) found that all of the alluvial/placer galamsey operations require a constant water supply and require extensive use of land. These operations are thus set up close to or along riverbanks, which causes a negative environmental impact such as a change in the river's course (Zhu et al. 2015). This study will, therefore, only focus on alluvial galamsey or SSM in close proximity to rivers. Major rivers affected are the Tano, Ankobra, Ofin and Pra rivers where great increases in sediment loads in rivers change the dynamics of the river and have a secondary ecological effect on the biodiversity surrounding the river (Asner et al. 2013). Asner et al. (2013) also found by visual inspection of aerial photos that the effect of increased sediment loads in the rivers affects the rivers even hundreds of kilometres downstream. In terms of this study, it is important to note that operational galamsey mining sites and legally operated small-scale mining sites cannot be distinguished from each other with satellite imagery only with current knowledge, ground survey data will have to be incorporated. This study attempts to detect SSM that includes both operational galamsey and legally operated mining sites.

Most of the literature with regards to illegal mining or small-scale mining globally is about policymaking, such as Hilson (2001, 2016), Aryee, Ntibery & Atorkui (2003), Teschner (2012), Corbett, O'Faircheallaigh & Regan (2017), Hilson et al. (2017), Vogel, Musamba & Radley (2018), Hilson, Goumandakoye & Diallo (2019), Pedersen et al. (2019), and Otamonga & Poté (2020) or the environmental impacts or health assessments that involves manual sampling methods, for example Veiga, Maxson & Hylander (2006), Emmanuel A (2013), Clifford (2017), Gyamfi, Appiah-Adjei & Adjei (2019), Moody et al. (2019), and Knoblauch et al. (2020). The socio-economical status or the mapping of the types of operations of SSM operations involves interviews or fieldwork (Ferring, Hausermann & Effah 2016; Mantey et al. 2017; Bansah et al. 2018; Owusu-Nimo et al. 2018; Obeng et al. 2019; Yankson & Gough, 2019). Only a few examples exist of where remote sensing is used to map or monitor SSM and these include Asner et al. (2013), Elmes et al. (2014) Kranz, Lang & Schoepfer (2017), and Snapir, Simms & Waine (2017) who used optical imagery. Maowei et al. (2011) used SAR to map illegal mining of iron ore in China but these were not SSM operations.

Almeida-filho & Shimabukuro (2000) have published the only study in using the backscatter values of SAR to map the degeneration caused by SSM. The aim of their study was to investigate the possibility of SAR to detect degradation areas caused by independent gold miners, "garimpeiros", in the Amazon because of the regular cloud cover in the region. Almeida-filho & Shimabukuro (2000) used three 18 m resolution, L-band, HH polarization Japanese Earth Resource Satellite-1 (JERS-1) images from the years 1993 (dry season), 1994 (rainy season), and 1996 (rainy season). Speckle filtering was applied with a 7x7 window kernel and the images were resampled to 30 m resolution to match the resolution of Landsat TM, acquired in 1994, used as the reference image. Their study area was the Tepequém plateau, situated in northern Brazil, that consisted of savannah grass that was surrounded by tropical rain forest. They found that the low grassland vegetation produced subtle tonal contrast in the SAR imagery compared to the high contrast produced by deforestation in studies done in the forested areas (e.g. Saatchi et al. 1997, Shimabukuro et al. 1998, Dutra et al. 1999). Due to the similar responses between eroded areas and the savannah grass the degraded areas from the gold mining could not be identified in the single-date JERS-1 SAR imagery. Their change detection normalized difference index (NDI) technique showed that was possible to detect land cover change even with the low tonal contrast of the grasslands. Due to the lack of a reliable classifier for SAR imagery Almeida-filho & Shimabukuro (2000) were unable to produce a thematic map of the degradation areas found in their 1993-1994 NDI image.

From the study done by Almeida-filho & Shimabukuro (2000), it is clear that SAR has the potential to detect SSM. Their challenge of detecting the degradation areas in single-date imagery can be tested over forested areas where gold mining takes place, such as in Ghana. The recent publication of Forkuor, Ullmann & Griesbeck (2020) proved that SSM in Ghana can be detected with SAR. They used Sentinel-1 time series data and compared the mean, minimum and maximum backscatter difference images of both polarizations. They found that the minimum backscatter images where the most sensitive to detecting changes caused by mining-induced land cover changes in Ghana and that the threshold value of +1.65 dB was suitable to classify this change.

Since the year 2000, machine learning classification algorithms such as random forest have been tested and found to give reliable classification results on SAR imagery (e.g. Fu et al. 2017; Mahdianpari et al. 2017; Bangira et al. 2019). The change detection analysis can be improved by using imagery in the same season and thematic maps can also be created. The concepts of SAR, classification, machine learning and change detection is explained in more detail in the next sections.

2.2 REMOTE SENSING WITH SYNTHETIC APERTURE RADAR

The radiation from satellite synthetic aperture radar has the unique ability to penetrate through cloud cover which is essential for this study. Regularly available reliable remote sensing imagery is required to detect or map SSM, therefore this section explains the concepts of remote sensing and SAR for detecting SSM.

Remote sensing is the science of observing phenomena of interest with the use of a sensor, enhancing the human capability of studying objects in a wider spectrum than the visible electromagnetic spectrum (Campbell 2006). Earth observation entails the analysis of the electromagnetic radiation (EMR) that is reflected from a target of interest to be measured by instruments based on satellites or aerial platforms (Lillesand, Chipman & Kiefer 2008; Mather & Koch 2011). Earth observation instruments are broadly divided into two categories: active or passive. Active instruments emit their own energy such as synthetic aperture radar (SAR). Passive instruments measure the reflection or radiation of electromagnetic energy of a target and rely on the energy of the sun (Campbell 2006). In earth observation, these passive instruments are typically optical sensors. Optical sensors detect EMR in the visible and near-infrared (VNIR) (0.4 to 1.2 µm), mid-infrared (MIR) (1.2 to 8 µm) or thermal infrared regions (TIR) (8 to 14 µm) while SAR sensors measure EMR in the microwave region (>1 mm) (Campbell 2006). Optical sensors are limited by cloud cover where the microwaves of SAR sensors can penetrate through clouds, smoke, and snow (Lillesand, Chipman & Kiefer 2008; Flores et al 2019).

2.2.1 The backscatter properties of SAR

SAR imagery is produced by an active emittance of microwaves from a satellite sensor to the earth's surface. The intensity of the microwaves that are scattered back i.e. backscatter is then measured by the sensor. Microwaves interact differently with different surfaces on the earth. Smooth surfaces such as calm water and roads act as specular reflectors, producing a very low backscatter signal return. Surfaces such as vegetation induce volume scattering and return medium backscatter signal. In urban areas where many vertical features exist, double-bounce occurs resulting in a very high backscatter signal (Figure 2.1). Radar images, therefore, represents an estimate of the radar backscatter where low backscatter is displayed as dark areas and high backscatter as bright areas (ESA Earthnet Online 2019). Dry, bare sand can also be confused with water because of low backscatter (Woodhouse 2005; Schlaffer et al. 2015). Another factor, other than the geometry of the objects, that also has an influence on the backscatter signal is the dielectric constant. The dielectric constant is a measure of the reflectivity and conductivity of a material (ESA Earthnet Online 2019). Water has a very high dielectric constant, at approximately 80, which

reflects the microwaves strongly. Thus, the presence of water in soils or vegetation increases their dielectric constant which results in significantly higher reflectivity (ESA Earthnet Online 2019). As a rule of thumb, a rough surface will scatter microwaves more strongly when wet.

A - Reflection off a smooth surface and a rough surface.

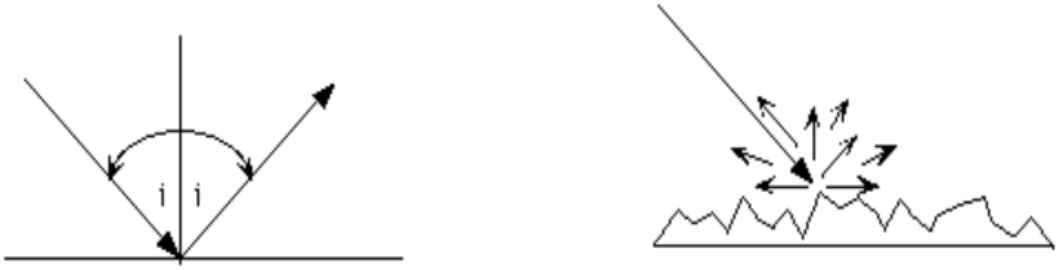

B - The double-bounce effect.

C - Volumetric scattering.

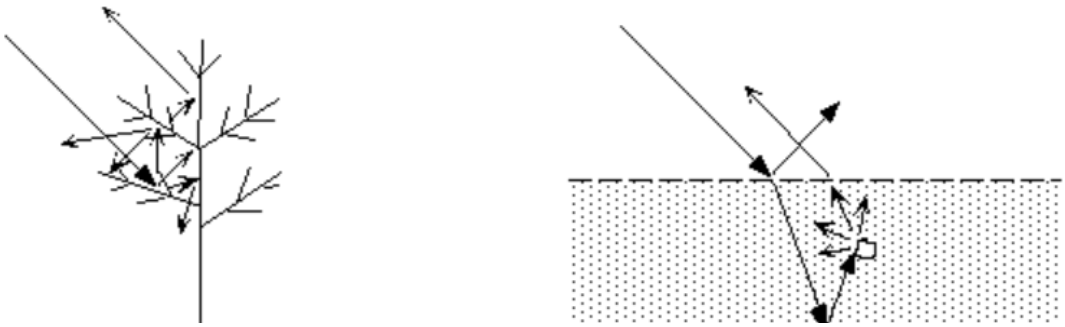

Figure 2.1 SAR scattering mechanisms [Adapted from ESA Earthnet Online 2019].

Different SAR sensors operate at different wavelengths. The shorter the wavelength the higher the scattering effect since the microwaves interact with objects of their wavelength size (ESA Earthnet Online 2019). Common SAR wavelengths are X-band, C-band and L-band SAR (Figure 2.2). X-band SAR has a wavelength of about three centimetres and interact with leaves and do not pass further than the leaf canopy of trees (Martinis & Rieke 2015). C-band SAR typically has a

wavelength of around six centimetres and can pass through the leaf canopy of trees and can interact with the twigs. L-band SAR ranges around 23-centimetre wavelength and can pass completely through the leaves and twigs of the tree canopy and reach the ground.

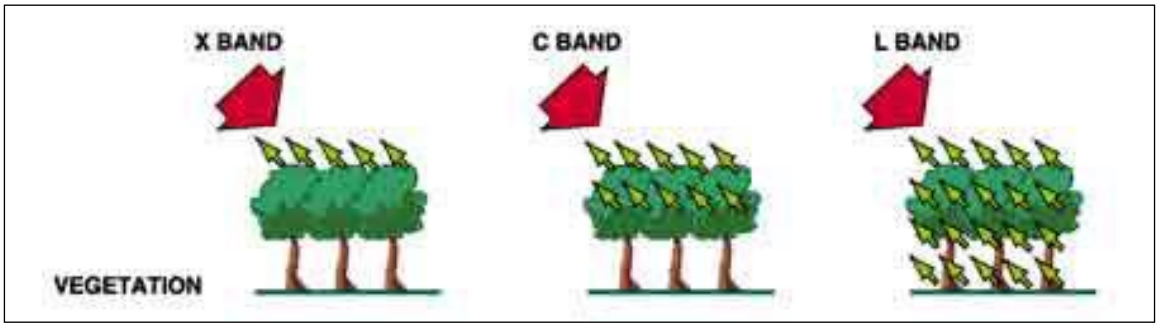

Figure 2.2 How different SAR wavelengths interact with trees where X-band has the shortest wavelength and L-band the longest [Adapted from ESA Earth Online (2019)].

The effect of incidence angle should also be considered. Water in open spaces is easily detectable with shallow incidence angles because the microwave signal is strongly reflected off the surface. For the mapping of water bodies in forested areas studies have shown that steep incidence angles produce better results for flood mapping since the signal from sensor with a shallow incidence angle is absorbed by the trees (Richards, Woodgate & Skidmore 1987; Bourgeau-Chavez et al. 2001; Lang, Townsend & Kasischke 2008; Hess et al. 2003; Wang & Imhoff 1993; Wang et al. 1995; Martinis & Rieke 2015). The theory is that the SAR signal has a shorter path through the forest canopy at a higher incidence angle, as a result, more microwave energy reaches the ground and trunks of the trees, in turn, increases the volume scattering (Lang, Townsend & Kasischke 2008; Hess et al. 2003; Martinis & Rieke 2015).

2.2.2 The pre-processing of SAR

Pre-processing is a necessary step to correct for errors and the removal of flaws present in satellite imagery (Mather & Koch 2011). Pre-processing is done before the satellite imagery can be analysed. The common pre-processing steps of SAR imagery are radiometric correction, geometric and terrain correction, and speckle filtering.

Radiometric correction is the conversion of digital numbers of each pixel measured at the sensor to radiometrically calibrated backscatter such as sigma-nought or beta-nought. During this step, the relative phase of the received and transmitted signals and the correlation between the polarization bands are extracted.

Geometric terrain correction usually follows where a digital elevation model (DEM) is used to correct terrain distortions that were introduced because of topographical variations (Hu, Ghamisi & Zhu 2018). Geometric correction is necessary to account for inherent geometry distortions that

occur due to the oblique view of the SAR sensor. These distortions include foreshortening, layover and shadow that occur at surface slopes (Chen, Sun & Hu 2018; Flores et al. 2019). Geometric terrain correction is conducted to remove these image distortions by incorporating a DEM to correct for the location of the topographically inclined pixels (Flores et al. 2019).

Another SAR image characteristic is speckle, which can be described as a grainy appearance that resembles "salt and pepper" noise (Lee et al. 1994). Speckle degrades the quality of the SAR image (Mansourpour, Rajabi & Blais 2006) and increases the difficulty of interpreting features in the SAR image (Coltuc, Trouvé & Bolon 2001; SNAP 2017). Speckle occurs as a result of interference from the many scattering echoes within a resolution cell and produce a seemingly random pattern of brighter and darker pixels (Lee et al. 1994; Flores et al. 2019; Rana & Suryanarayana 2019) and can be minimized with speckle filtering. Common speckle filters include Refined Lee, LeeSigma7x7 and Intensity Driven Adaptive-Neighbourhood (IDAN). Speckle reduction can be done before or after the geometric terrain correction step.

An appropriate speckle filter depends on the requirements of the application and the characteristics of the SAR imagery (Rana & Suryanarayana 2019). Rana & Suryanarayana (2019) also noted that speckle filters with good noise removal capabilities compromise on the spatial and radiometric resolution of an image that results in the loss of image details which may not be acceptable for applications that involve the interpretation of small features and subtle changes in the image. They recommend selecting a speckle filter that retains the subtle structures if an image where the speckle noise suppression is balanced with the filter's effectiveness to preserve the fine details. This is important for the case of mapping small-scale mining. Rana & Suryanarayana (2019) tested multiple speckle filters for their effect on inundation mapping with Sentinel-1 imagery and found that the Lee filter with 3x3 kernel size provided a good balance in feature preservation.

Another commonly used speckle-noise reduction method is by applying a multi-temporal speckle filter (Quegan et al. 2000, SNAP 2017). By using multi-temporal SAR imagery both the temporal and the spatial resolution can be filtered (Quegan et al. 2000). Quegan et al. (2000) tested their multi-temporal speckle filter on the application of forest monitoring and noted that C-band SAR displays very little sensitivity to the spatial or temporal forest variations, especially in high biomass forests. This is because shorter wavelengths of SAR get saturated at a biomass level of 30-50 tons/ha where forest biomass typically have a biomass level of more than 500 tons/ha. Quegan et al. (2000) mentioned that there are multiple reasons that the effective monitoring of forests or drastic changes that take place in forests such as clearcutting, with the available C-band SAR imagery is hindered. One of these reasons is that single-date C-band SAR images often show little differentiation between forest and other types of vegetation cover. Quegan et al. (2000) noted that

other multi-temporal studies such as Lopez et al. (1993) and Ribbes et al. (1997), applied spatial filtering that assumed a gamma-distributed texture of the data, which is not an appropriate model for their C-band SAR data at their scales of interest. Lopez et al. (1993) and Ribbes et al. (1997)'s filtering models left noise in the output image, which made the images appear sharper and the output image required further filtering to reduce the classification error (Ribbes et al. 1997). Single-date SAR speckle filtered images have not been compared with multi-temporally filtered SAR imagery for the possibility that the multi-temporally filtered SAR image can produce a more accurate classification image, especially over forested areas (Quegan et al. 2000).

2.3 LAND COVER CLASSIFICATION FOR MAPPING SMALL-SCALE MINING

Remote sensing has been widely used for the application of land cover classification (Chen et al. 1996) as a method for mapping and monitoring (Rodriguez-Galiano et al. 2012). Land cover mapping is essential for the estimation of land cover change because land cover change is directly related to human and natural health and growth (Pierce, Dobson & Ulaby 1994; Bala et al. 2007; Rodriguez-Galiano et al. 2012). Typical applications of land cover classification are in the estimation of deforestation, analysing the extent of flood events and determining areas for biodiversity conservation (Lambin et al. 2001; Mas et al. 2004; Turner, Lambin & Reenberg 2007; Rodriguez-Galiano et al. 2012). Additionally, it can be used for monitoring of illegal logging and mining activities in remote locations (Asner et al. 2013; Elmes et al. 2014; Owusu-Nimo et al. 2018).

Land cover mapping using remote sensing is driven by the need for knowledge of the spatial distribution of land use and land cover (LULC) (Parihar et al. 2014). Remote sensing data has become easily accessible and the advancement of computers and algorithms has caused immense growth in the field of land cover classification (Waske & Van der Linden 2008). Classified images are then used to assist in policymaking and decision making on the effects of urbanization and industrial development, illegal activities, protecting important natural areas, human settlement planning, food security and more (Ban & Wu 2005; Ban, Hu & Rangal 2010; Pierce, Dobson & Ulaby 1994; Hilson et al. 2017) especially in remote areas where data is scarce. Classification is, therefore, a potential approach to map SSM in remote areas. This section describes the different approaches to image classification such as supervised and unsupervised classification, the extraction of additional features from an image such as texture, the classification scheme design and the accuracy assessment of the classification output.

2.3.1 Image classification

Image classification is the process where pixels or objects in an image is assigned to a class (Lillesand, Chipman & Kiefer 2008). Image classification can take place without the intervention of an analyst or with prior defined classes created by an analyst. Parametric and non-parametric classifiers are available, however non-parametric classifiers, such as the machine learning classifiers, have been known to produce more accurate and reliable results than parametric classifiers. In this section unsupervised classification and the use of machine learning for supervised classification is described.

Supervised classification involves user input by means of training data to assist the classifier in assigning information classes to the pixels or objects. Unsupervised classification is the assignment of pixels to a class without prior knowledge of the class and without initial input from the user. An advantage of supervised classification over unsupervised classification is that the analyst has more control over the output of the classification algorithm. This is because the informational categories used as input for the classifier are defined prior to the analysis. A second advantage is that spectral classes are automatically matched to information classes during the classification process (Campbell & Wynne 2011). Supervised classification is, however, only as accurate as of the level of expertise available during the training-set selection and still proves a major challenge to automate (Manavalan 2017; Shen et al. 2019). Machine learning is the ability of computer systems to perform specific tasks without explicit instructions but relying on patterns for prediction (Bishop 2006). Machine learning is considered a subset of artificial intelligence, where the mathematical models rely on sample data for the training of the algorithms through pattern recognition (Bishop 2006). Classification falls in the category of machine learning.

The five most popular machine learning algorithms used for classification in remote sensing are decision trees (DT), random forest (RF), k-nearest neighbour (KNN), support vector machine (SVM) and kernel support vector machine (C-SVM) (Bangira et al. 2019). The popularity of the use of these algorithms for remote sensing applications is because of their flexibility, simplicity and computational efficiency (Myburgh & Van Niekerk 2014). Each classification algorithm uses a different mathematical model as an approach to pattern recognition and prediction of classes. The classification algorithm that is the most popularly used in remote sensing is RF due to the algorithm's robustness with respect to noise (Breiman 2001), however, the appropriate classification algorithm to be used depends on the research question as well as the type of input data. Therefore, understanding the differences in the classification approaches together with the advantages and disadvantages is important.

Decision trees are a non-parametric supervised learning method used for classification and regression (Scikit-learn developers 2012). DT create a model that predicts the value of a target by learning simple decision rules that are inferred from the data input features (Pedregosa et al. 2011).

Random forest is a classifier that fits a number of decision tree classifiers on various subsamples of the dataset. RF then uses averaging to improve the predictive accuracy and to control overfitting. Breiman (2001:5) defines RF as a "combination of tree predictors such that each tree depends on the values of a random vector sampled independently and with the same distribution for all trees in the forest." RF selects the best solution from all the predictive sets by means of a voting parameter and RF stores the significance of the input features (Han et al. 2017).

Neighbours-based classification, such as k-nearest neighbour, is a type of instance-based learning or non-generalizing learning that does not attempt to construct an internal model (Scikit-learn developers 2012). The algorithm only stores instances of the training data. Classification is computed from a major vote of the nearest neighbour of each point based on e.g. Euclidean distance between points (Pedregosa et al. 2011).

Support vector machines can be used for classification and regression problems where input vectors are non-linearly mapped to a very high-dimension feature space (Cortes & Vapnik 1995) and are very useful for non-linear data (Cortes & Vapnik 1995; Hwang & Jung 2018). SVM classifies data by defining a hyperplane that maximizes the Euclidean distance between the two groups. When a hyperplane cannot separate the two groups while maximizing the margin, C-SVM is used (Chen, Lin & Schölkopf 2005) where C is the regularization parameter that has an inverse relationship with the margin. SVM utilises kernel functions that map the input data to a higher dimension where the optimal hyperplane can be defined to separate two or more classes when the margin between the vectors in each class is at the maximum (Cortes & Vapnik 1995). Different types of kernels exist such as linear, polynomial, radial basis function (RBF) and sigmoid. The RBF-kernel is most commonly used in many applications (Hsu, Chang & Lin 2003). SVM is a highly accurate classifier compared to classifiers such as decision trees (DataCamp 2019).

2.3.2 Feature extraction

Feature extraction is the process of transforming the original input data to maximize the variance of the data for the differentiation between classes for classification (Fukunaga 1990; Benediktsson & Sveinsson 1997). Feature extraction is important so that the representation of the data can enhance the design and performance of the classifier (Benediktsson & Sveinsson 1997). The feature extraction methods in this study involved the extraction of image texture and geometric feature from the objects created with segmentation, which are discussed below.

2.3.2.1 Pixel-based and object-based image analysis

Pixel-based image analysis (PBIA) is the traditional method used in classifying images where each pixel is assigned to a class. Object-based image analysis (OBIA) is an approach where objects, groups of pixels with similar intensity, are classified (Gilbertson & Van Niekerk 2017; Ma et al. 2017). Objects can either be created by means of digitising or by using a segmentation algorithm. The latter is more accurate and faster (Blaschke 2010). OBIA has in many cases increased the accuracy of classification of remote sensing imagery (e.g. Walker et al. 2010; Longepe et al. 2011; Jin, Mountrakis & Stehman 2014; Gilbertson & Van Niekerk 2017; Ma et al. 2017).

OBIA techniques have become widespread since high-resolution imagery has become more available (Blaschke 2010; Belward & Skøien 2015; Ma et al. 2017). The high-resolution imagery produced a new challenge in image processing which OBIA addresses (Ma et al. 2017). The challenge is that high-resolution images have a significant increase in the within-class spectral variability that decreases the potential of a purely pixel-based approach to classification because of the confusion of classes that takes place (Blaschke et al. 2014). The result is that OBIA has largely replaced the traditional PBIA technique for high-resolution image analysis (Blaschke et al. 2014; Ma et al. 2017). OBIA is derived from image analysis techniques such as segmentation, edge detection, feature extraction and classification that has been used in remote sensing for decades (Kettig & Landgrebe 1976; Levine & Nazif 1985; Strahler et al. 1986; McKeown et al. 1989; Pal and Pal 1993; Câmara et al. 1996; Hay, Niemann & McLean 1996; Lobo, Chick & Casterad 1996; Ryherd & Woodcock 1996; Wulder 1998; Aplin, Atkinson & Curran 1999; Baltsavias 2004; Blaschke 2010). Ma et al. (2017) reviewed supervised object-based image classification and summarize the different classification processes. They found that classification accuracy is dependent on the sensor, segmentation scale, training size set, classification algorithm and land-cover types. Ma et al. (2017) also found that a negative correlation exists between the overall accuracy of the classification and the number of defined classes, the spatial resolution correlates negatively with the optimal segmentation scale and study area and that random forest has shown the best performance in object-based classification so far followed by SVM.

Using segmentation to create objects for OBIA requires the appropriate segmentation algorithm. Image segmentation algorithms can be divided into four categories i.e. point-based, edge-based, region-based and combined (Schiewe 2002). The segmentation algorithm divides the image into segments or objects which are regions of pixels that are grouped together by one or more criteria of homogeneity. Segments also provide additional spectral information such as the mean spectral values for that object (Blaschke 2010). The most commonly used segmentation algorithm is the multiresolution segmentation (MRS) algorithm (Baatz & Schape 2000; Belgiu & Drăguţ 2014;

Gilbertson, Kemp & Van Niekerk 2017), which rely on the parameters shape, scale and compactness to segment an image. Belgiu & Drăguţ (2014) found that OBIA can be automated without sacrificing on classification accuracy, however, it remains good practice to test the parameters of MRS that best suits the input data.

Gilbertson, Kemp & Van Niekerk (2017) tested six OBIA scenarios for the effect of good, over- and under-segmentation. Under-segmentation (using a scale factor that is too large) has a negative effect on classification because of the mixing of pixels that occur due to the objects being too large for the actual field. Over-segmentation also reduces the accuracy of MRS, but less than under-segmentation. The ideal MRS results, according to Gilbertson, Kemp & Van Niekerk (2017) as shown in Figure 2.3, where scenario 'G' is the ideal scenario where slight over-segmentation is acceptable and the boundaries are mapped accurately.

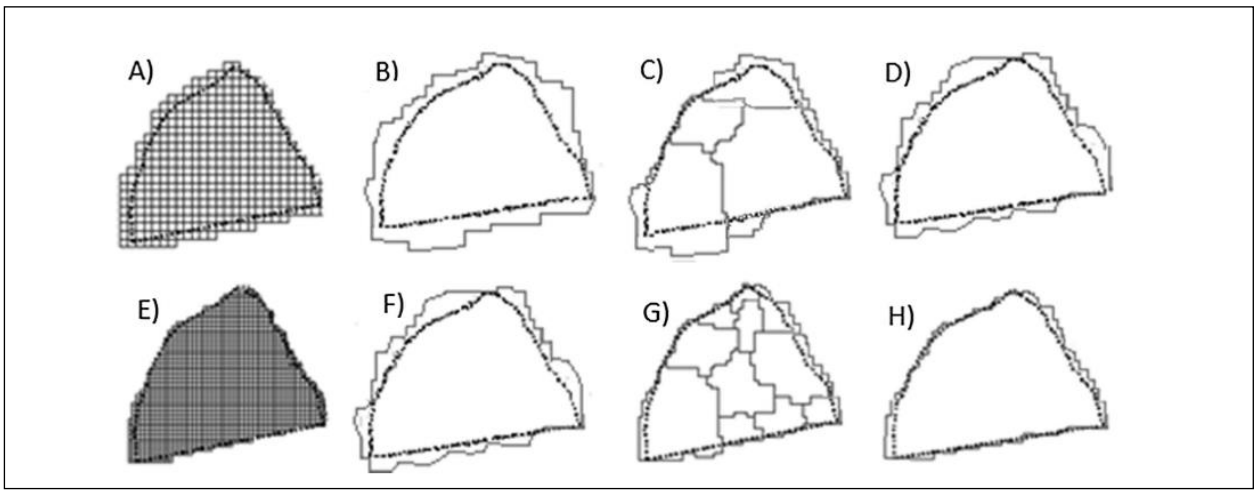

Figure 2.3 Figure illustrating the eight different segmentation scenarios possible with multiresolution segmentation as shown in Gilbertson, Kemp & Van Niekerk (2017). The segmentation results of 'G' are ideal.

Normally segmentation is performed on optical imagery that may or may not include additional features such as texture bands or indices such as in (Gilbertson, Kemp & Van Niekerk 2017). Due to the high percentage of cloud cover in Ghana finding a suitable optical image with low cloud cover was not possible. Instead, segmentation was done on the synthetic aperture radar (SAR) imagery. Only a few examples of literature exist where segmentation was done on SAR such as in El-Zaart (2015), Sephton et al. (1994), and Xu, Tian & Ding (2008) and Zhang & Ju (2011) is the only example where MRS was performed on SAR imagery using a novel method. These studies only evaluated the performance of their segmentation algorithms and the segmentation results were not applied as an object-based approach to classification. Therefore, the application of segmentation on SAR imagery for land-cover classification has not been tested before. Zhang & Ju (2011) noted that the speckle of SAR imagery reduces the segmentation performance significantly, therefore, it can be expected that the segmentation results on SAR imagery will be

of a lesser quality than segmentation performed on optical imagery. For the purpose of this study, segmentation on SAR is the only way to ensure that the classification of all of the imagery on the different dates is comparable.

2.3.2.2 Image texture

Jin, Mountrakis & Stehman (2014) found in their study for land cover classification that even though only using the intensity backscatter values of the SAR imagery produced accurate classification results, the addition of features such as image texture improved their overall accuracy with 7%. This study relies solely on SAR imagery and no indices were incorporated from optical imagery, because of the high percentage of cloud cover in the region for most of the year, therefore the addition of image texture as input features for the classification process potentially increases the accuracy of mapping SSM.

Texture is a statistical or structural measure that quantitively describes the relationship of digital values of neighbouring pixels in an image (Long, Zhang & Feng 2003; Hall-Beyer 2017). Texture is a representation of the surface and structure of an image that is derived from the intensity values of the image. Texture is often defined as patterns of elements, repetitions or surfaces (Srinivasan & Shobha 2008). Haralick created the important grey level co-occurrence matrix (GLCM) texture approach which is fundamental for texture for image interpretation (Haralick, Shanmugam & Dinstein 1973; Haralick 1979; Hall-Beyer 2017). GLCM and grey level difference vectors (GLDV) are the most commonly used texture methods for the application of image processing in remote sensing (Clausi 2002; Srinivasan & Shobha 2008). GLCM has been used for many image classification applications and is known to improve the classification accuracies (Myburgh & Niekerk 2013; Hall-Beyer 2017). The most commonly used texture measures used are homogeneity, contrast, correlation, angular second moment, entropy for GLCM and correlation, entropy, and mean for GLDV (Clausi 2002; Myburgh & Niekerk 2013; Hall-Beyer 2017).

2.3.3 Classification scheme design

To analyse the potential for the detection of small-scale mining two classification schemes were considered in this study. A multi-class classification scheme is popularly used for land cover classification applications (e.g. Quegan et al. 2000; Mahdianpari et al. 2017; Verhulp & Van Niekerk 2017). The other classification scheme of interest is a binary classification scheme commonly used for inundation mapping such as in Shen et al. (2019). Both are of interest for this study to compare the accuracy and robustness of the classification algorithms.

Binary classification schemes are simple and highly accurate where the classification scheme merely consists of, for example, water and non-water. After several studies attempted to take advantage of the very low backscatter received from water bodies (Hirose et al. 2001; Yamada 2001; Matgen et al. 2011; Giustarini et al. 2013) it has been identified that when mapping large water-bodies the simple single threshold method did not produce good results (Tan et al. 2004) because of the variability of the environment such as wind-roughening and satellite parameters (Martinis, Twele & Voigt 2009; Shen et al. 2019). Spatial and temporal variety in backscatter also occurred for permanent water bodies in Martinis & Rieke (2015). The SSMs in this study are considered as small water bodies, therefore, the single threshold method might still hold. The threshold-based approach has greater potential for automation (Giustarini et al. 2013) and can easily be applied in change detection. Important to note is that when the histogram of the backscatter pixels is not bimodal, training with regions of interests is recommended but this approach is not easily automated (Shen et al. 2019). Both methods are tested in this study. Important to note is that threshold values separating flooded and non-flooded (or water and non-water) regions are hardly transferable from one area to the next due to the dependence on environmental and system parameters (Martinis & Rieke 2015). In these studies, Hirose et al. (2001), Yamada (2001), Bazi et al. (2005), Matgen et al. (2011), Santoro & Wegmüller (2012), Giustarini et al. (2013), and Lu et al. (2014), change detection was used to select only pixels that were significant to flooding as to reduce false classification of water. This approach is further discussed in Section 2.4.

2.3.4 Accuracy Assessment

The most common method for the accuracy assessment of classification analysis is by using a confusion matrix (Congalton, Oderwald & Mead 1983). The confusion matrix compares predicted values with the test dataset values and counts the number of times an object was classified as correct and incorrect per class (Figure 2.4). From the confusion matrix the overall accuracy, user- and producer's accuracies can be derived (Congalton 1991). These measures are standard error metrics that are used to quantify the accuracy measurement.

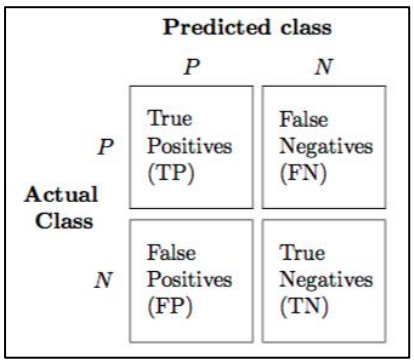

Figure 2.4 Example of a confusion matrix.

The producer's accuracy is a measure that indicates the probability of a reference pixel being correctly classified where the producer of the classification can know how well a certain area is classified (Congalton 1991). The user's accuracy indicates the probability that a pixel classified on the image actually represents the true class on the ground (Story & Congalton 1986).

The kappa coefficient is also an important metric often used in the accuracy assessment of classification results in remote sensing applications (Congalton, Oderwald & Mead 1983; Foody 2020). The kappa coefficient is not an index of accuracy, but rather an indication of agreement beyond chance and has recently been evaluated as irrelevant and inappropriate for typical remote sensing applications (Foody 2020). Despite this recent evaluation, the kappa coefficient was used in this study as a measure of reliability as it has been used by many remote sensing studies for the accuracy assessment of the production of thematic maps (e.g. Congalton, Oderwald & Mead 1983; Gilbertson & Van Niekerk 2017; Bangira et al. 2019).

2.4 CHANGE DETECTION FOR DETECTING SSM

Small-scale mining in tropical regions is associated with a loss in the forest canopy as well as an increase in standing pools and bare ground. Therefore, studies that are associated with deforestation monitoring or flood mapping is applicable to the detection of SSM. Much work has been done in mapping forests and floods with SAR imagery due to the advantage of microwaves that penetrate through the cloud cover. A substantial advancement in the development of algorithms for flood delineation in SAR imagery has taken place over the past decade (Schlaffer et al. 2015). These algorithms are divided into the single-image analysis (traditional analysis) and change detection analysis. The issue that arises with traditional image analysis techniques on single-date SAR imagery is that it is not possible to distinguish between permanent and transient water bodies (Schlaffer et al. 2015). Distinguishing between permanent and transient water bodies is important in the case of detecting SSM. Quegan et al. (2000) noted that the application of SAR for forest studies is one of the most active applications, this is because of the ability to map biomass

with SAR imagery. Drastic changes in biomass such as changes in the forest cover due to deforestation can be detected with SAR. Forests exhibit temporal stability (particularly the older forests) which can be distinguished from non-forest areas by using time-series imagery. The ability to map the loss in forest cover with change detection using SAR is important for detecting SSM.

Change detection is the process of identifying differences of a phenomenon in a satellite image with the application of multi-temporally datasets (Singh 1989; Lu et al. 2004). A change-image, in its simplest form, can be produced by subtracting the backscatter values of a SAR scene at a time of interest with a reference SAR scene (Schlaffer et al. 2015). Afterwards, classification, thresholding (Martins, Twele & Voight 2009) or region growing (Matgen et al. 2011, Giustarini et al. 2013) can be applied. A few factors that should be taken into consideration when applying change detection is that the SAR scenes should have the same viewing geometry, polarization configuration and the time period (Schlaffer et al. 2015). The acquisition of the SAR images should be during the same season to reduce the impact of seasonal and phenological variability (Lu et al. 2004; Crowson, Hagensieker & Waske 2019). The most important consideration is that multi-temporally image registration and radiometric registration must be done before the change analysis begins (Lu et al. 2004). In the case of this study, the scenes should be of the dry season of Southern Ghana, which is from the middle of November to February (GhanaWeb 2019). During the wet season, flooding occurs which leads to increased variability in the change analysis.

Two major change detection approaches can be followed. The first is the post-classification comparison approach where two images are first classified separately and then compared afterwards (Radke et al. 2005; Haboudane & Bahri 2007; Gong et al. 2016). The second is the post-comparison analysis where the difference image first derived and the analysis is applied to gain change detection results (Gong, Zhou & Ma 2012). The post-classification approach accumulates classification error (Gong et al. 2016) and was not considered for this study. The post-comparison approach is the mainstream approach with excellent performance (Gong et al. 2016) and was, therefore, considered for this study.

Many studies have analysed change detection with SAR (e.g. Cihlar, Pultz & Gray 1992; Lê, Atto & Trouve 2015; Valarmathi & Suganya 2015; Gong et al. 2016; Muro et al. 2016; Cui et al. 2017; Garzelli & Zoppetti 2017) and found that SAR has great potential in this regard. An example of how SAR was implemented is where Gong et al. (2016) created a novel change detection approach which detects changed and unchanged areas without the process of first generating a difference image. Their aim was to produce a change detection map directly from two SAR images with the trained deep neural network. The reason for their study was to find a way to map changes quickly when scenarios such as natural hazards happen or disaster evaluation. SSM is an environmental

hazard where changes in the land cover take place quickly. A system such as Gong et al. (2016) is proposing is a promising system that should be explored for the detection of SSM. Muro et al. (2016) used a Sentinel-1-omnibus (S1-omnibus) method, as proposed by Conradsen, Nielsen & Skriver (2016), to test the potential of Sentinel-1 time-series imagery for detecting differences in water surface dynamics in wetlands. Muro et al. (2016) also used Landsat-8 imagery during the same period of time as a reference. They found that the S1-omnibus method was capable of capturing in space and time changes produced by water surface dynamics whether the changes were sudden or gradual. The results from Muro et al. (2016) prove that Sentinel-1 time-series imagery is useful for SSM monitoring where the water dynamics of the SSM pools can change suddenly, and the SSM sites which can suddenly occur or gradually spread into the surrounding regions. For the purpose of the study, it first needs to be tested whether change detection with SAR can detect SSM in a viable manner before applying complex algorithms such as the deep neural network or the S1-omnibus.

In addition to image differencing, a change detection classified image can be created from the difference image with thresholding. Thresholding is the process of classifying the pixels of a given image into two groups, normally objects and background (Tsai 1985). One class include the pixels with grey values above a certain threshold and the other equal to and below the threshold. This is called bilevel thresholding (Tsai 1985). Due to the simplicity of thresholding, a few automatic threshold methods have been proposed of which the Otsu method is commonly used for surface water mapping (e.g. Du et al. 2016; Bangira et al. 2017; Chini et al. 2017; Bangira et al. 2019). Automatic thresholding was evaluated by Martinis, Twele & Voigt (2009) for the mapping of flooding in England with high-resolution SAR imagery and their results yielded high classification accuracies. In the case of disaster management, the collection of ground truth data as input training samples for a supervised method is unfeasible. Therefore, an automatic thresholding method is suitable for the disaster management of floods when an accurate map of the flood has to be produced in a short period of time (Martinis, Twele & Voigt 2009). In the case of illegal mining, applying unsupervised automatic thresholding in conjunction with change detection may be very useful in the case of an emergency. Another method used for evaluating the accuracy of thresholds for classification is the Receiver Operating Characteristic (ROC) method (Hanley & McNeil 1982) that was also used for SAR target discrimination validation by Principe, Kim & Fisher (1998).

The Otsu threshold is a “nonparametric and unsupervised method of automatic threshold selection for picture segmentation” (Otsu 1979: 62). The method selects a threshold automatically from a grey level histogram that directly deals with the problem of evaluating the goodness of thresholds. An optimum threshold (or set of three thresholds) is selected by the discriminant criterion; namely,

by maximizing the discriminant measure (or the measure of separability of the resultant classes in grey levels). The Otsu method may be the most simple and standard method for automatic threshold selection that can be applied to various problems (Otsu 1979). Another threshold method used in remote sensing is the Tsai threshold. This method uses the moment-preserving principle (Tsai 1985). The threshold values are computed deterministically in such a way that the moments of an input picture is preserved in the output picture. The approach is described for global thresholding, but it is applicable to local thresholding as well (Tsai 1985).

2.5 LITERATURE SUMMARY

The literature reviewed in this chapter showed that remote sensing holds much potential for the detecting and mapping of SSM. More research is needed for the direct mapping of SSM with remote sensing. Attempts at mapping SSM with optical imagery have proven plausible but due to the presence of prolonged cloud cover in many of these regions regular monitoring has proven difficult. The mapping of SSM with SAR was last attempted in the year 2000 where degradation areas of SSM could be seen but in low resolution (Almeida-filho & Shimabukuro 2000). Change detection with optical imagery to detect SSM has also proven successful (Snapir, Simms & Waine 2017) but the method remains limited to the challenge of cloud coverage. With Sentinel-1, the regular acquisition of medium resolution SAR imagery is possible to map and monitor SSM. The classification of SSM with advanced machine learning classifiers and SAR has also not been attempted yet. The methods used for the classification of deforestation with SAR are a possible approach for the classification of SSM with SAR. The change detection methods used for flood monitoring with SAR that involves image differencing and thresholding is a possible approach for mapping the SSM regions because of the water characteristics of SSM pools.

Based on the literature three experiments were carried out to investigate these gaps in the current knowledge and are discussed in the following two chapters. Experiment 1 focusses on the effect of different SAR datasets on the classification accuracy to detect SSM. Experiment 2 presents a comparison of five machine learning algorithms applied to a single SAR dataset. Experiment 3 analyses the potential of a simple change detection approach with SAR imagery for the detection of SSM.

3 CHAPTER 3: THE EVALUATION OF SAR DATASETS AND CLASSIFICATION ALGORITHMS FOR DETECTING SMALL-SCALE MINING

This chapter is aimed at addressing Objectives 3, 4 and 5 with Experiments 1 and 2. Different SAR sensors, filtering levels and classification algorithms are compared. An overview of the data used for Experiments 1 and 2, as well as, the data transformation methods in preparation for analysis is given. The data preparation includes the pre-processing of the SAR data and the establishment of the training datasets. The classification methods are laid out and the results for each experiment are discussed. Figure 3.1 depicts a generalized flow chart of the methodology followed for supervised classification.

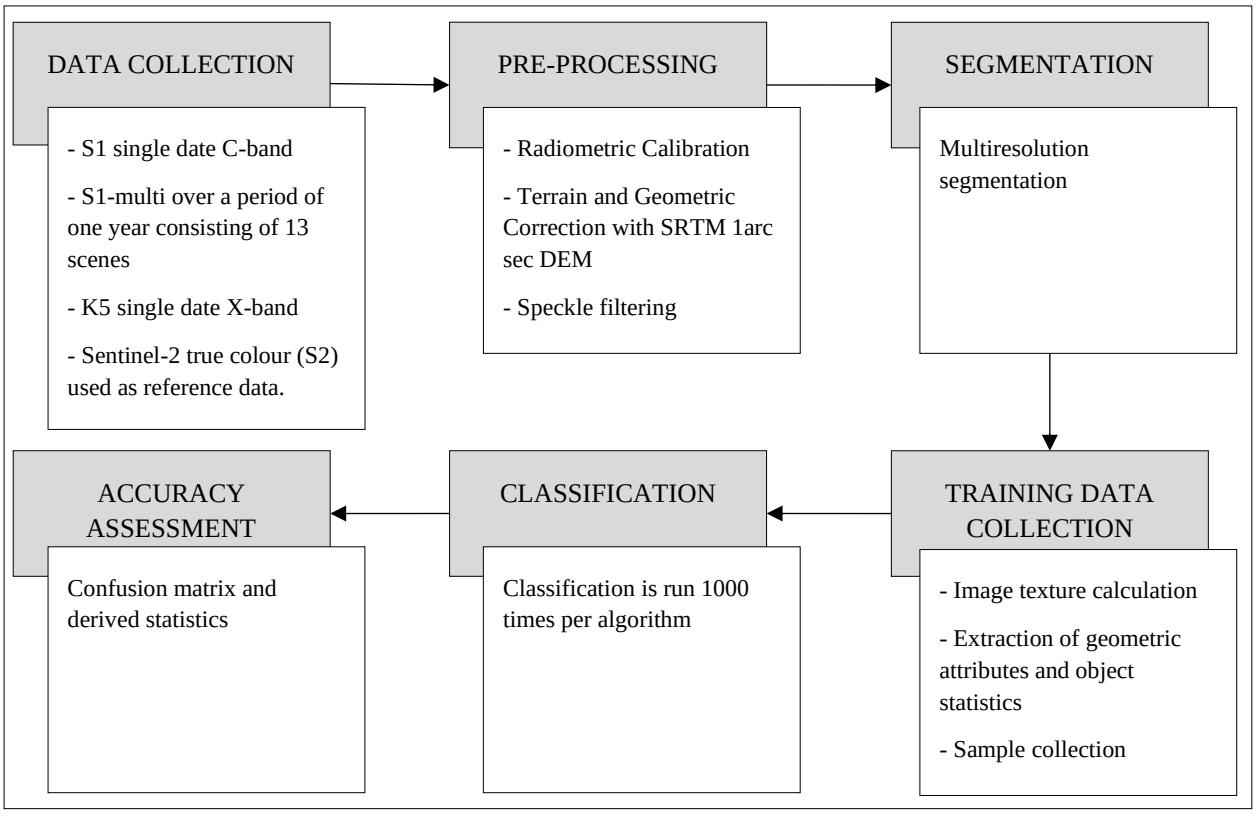

Figure 3.1 The generic workflow for supervised classification analysis.

3.1 DATA ACQUISITION

Experiment 1 was performed on both Sentinel-1 and KompSAT-5 imagery. The Sentinel-1 datasets are a single-date image (S1) and a multi-temporally filtered image (S1-MT). The KompSAT-5 dataset (K5) consisted of a single-date image. Experiment 2 utilised only the Sentinel-1 multi-temporally filtered dataset. The data preparation was, therefore, the same for both experiments. A summary of the imagery and their acquisition dates is given in Table 3.1.

Table 3.1 Summary of the satellite imagery for Experiments 1 and 2. Acquisition parameters of SAR data and optical imagery is listed.

Sensor	Mode	Polarization	Incidence angle	Acquisition date(s)	Resolution	Description
Sentinel-1	SLC IW	VH, VV	32.9º - 43.1º	2018/08/12, 2018/07/13, 2018/06/13, 2018/05/14, 2018/04/14, 2018/03/15, 2018/02/13, 2018/01/14, 2017/12/15, 2017/11/15, 2017/10/16, 2017/09/10, 2017/08/17	20 m	SLC IW C-band VH, VV
KompSAT-5	ES Standard	VH	28.8º - 55.0º	2018/07/12	3 m	ES Standard X-band VH
Sentinel-2	L1C	n/a	n/a	2018/08/05	10 m	L1C RGB (4-3-2)

The Sentinel-1 imagery is C-band (5.405 GHz) SAR backscatter with incidence angles ranging from 32.9º to 43.1º and the spatial resolution is 20 m. The Sentinel-1 imagery was accessed as Interferometric Wide Swath (IW) Single Look Complex (SLC) products from the Copernicus Open Access Hub. IW offers dual-polarization capability vertical transmit, horizontal receive (VH) and vertical transmit, vertical receive (VV). The range of dates for the Sentinel-1 imagery is from August 2017 to August 2018 and one image was selected for each month. While all 13 images were used for the multi-temporally filtering process, classification was only performed on the 12 August 2018 image.

The KompSAT-5 (Korea Multi-Purpose SATellite) X-band (9.66 GHz) image used in this experiment was provided by SI-Imaging Services. KompSAT-5's Enhanced Standard (ES Standard) mode is similar to Sentinel-1's IW mode, with single-polarization VH. The incidence angle ranges from 28.8º to 55º, the spatial resolution is 3 m and covers a swath of 30 km (SI-Imaging Services 2019). The date of acquisition is 12 July 2018.

Sentinel-2 optical imagery was used as the ground truth dataset for training and validation purposes. The aim was to retrieve an image with the least amount of cloud cover closest to the date of the single-date SAR imagery (July/August 2018). Sentinel-2 imagery is also freely available through the Copernicus Open Access Hub. Level-1C imagery was downloaded and only the true colour band combination (RGB 4-3-2) at 10 m spatial resolution was used. Figure 3.2 displays an example of each of the Sentinel-1 and the KompSAT-5 imagery over an area where abundant SSM

takes place surrounding the Ofin River. The ground truth Sentinel-2 image is also shown over the same area segment.

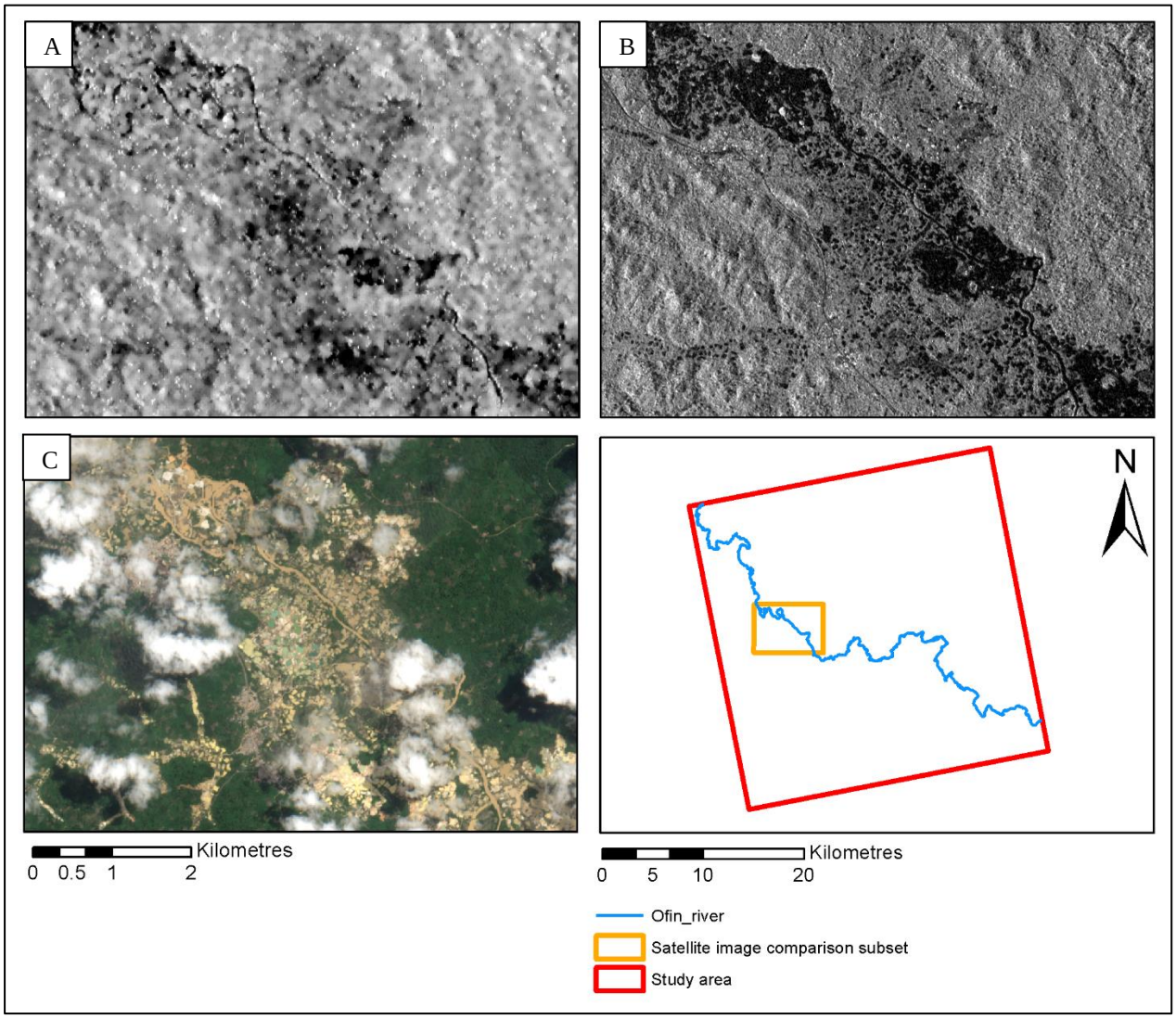

Figure 3.2 Example subsets of imagery used: A) Sentinel-1 VH backscatter on 8 August 2018, B) KompSAT-5 VH backscatter on 12 July 2018, and C) Sentinel-2 true colour image on 5 August 2018. The example area highlights a section of the Ofin River where abundant small-scale mining takes place.

3.2 DATA PREPARATION

The Sentinel-1 toolbox (S1TBX), available in SNAP, was used for the pre-processing of both the Sentinel-1 and KompSAT-5 datasets. The following pre-processing workflow was followed as shown in Figure 3.3.

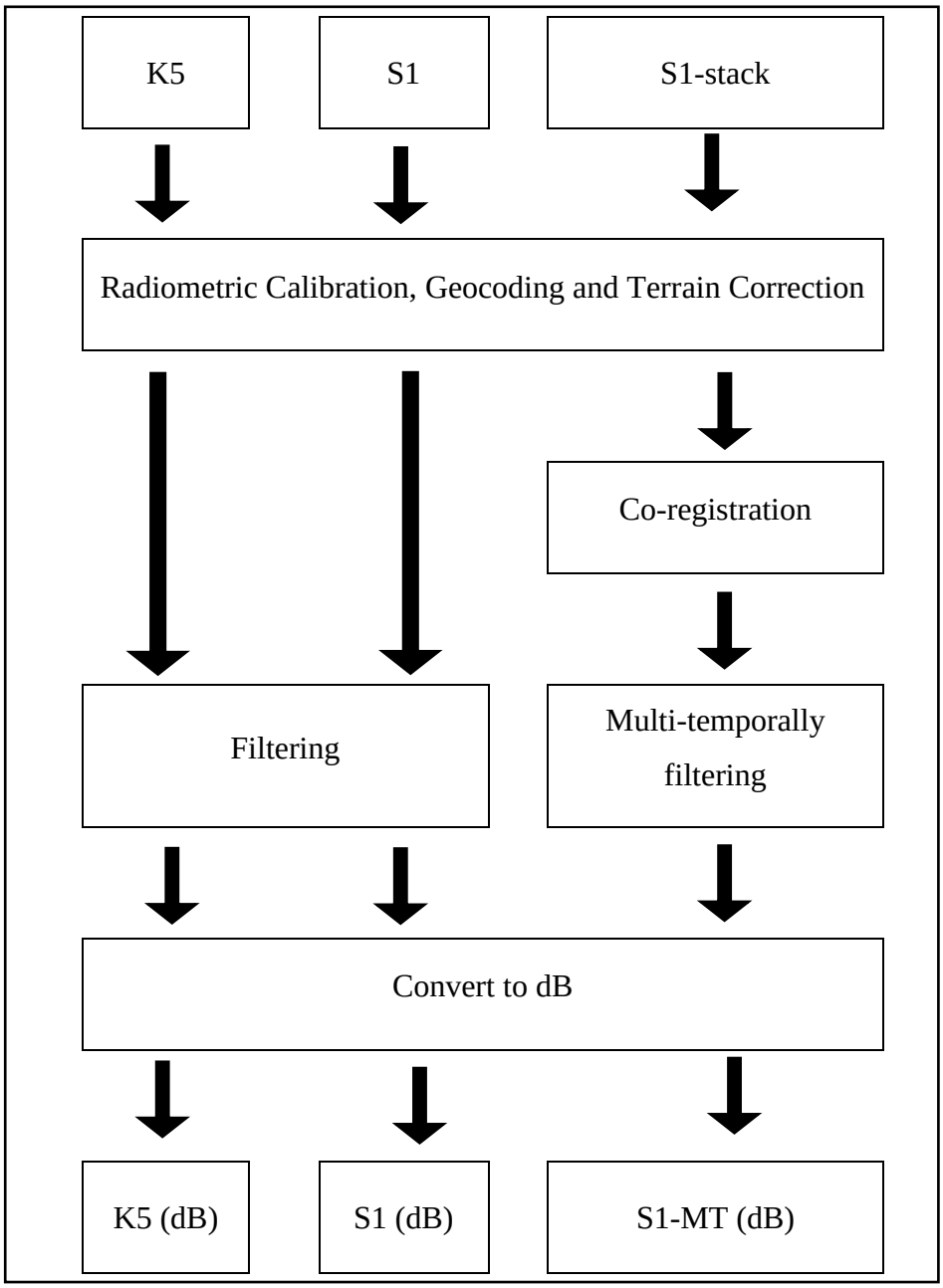

Figure 3.3 Pre-processing workflow for the preparation of the SAR data.

The pre-processing of KompSAT-5 and the single-date Sentinel-1 image (for Objective 3) was done separately from the pre-processing of the multi-temporally filtered Sentinel-1 image (for Objectives 4 and 5). All the backscatter bands underwent radiometric calibration where the image backscatter values are converted to sigma-0. Afterwards geocoding and terrain correction was performed using the Range Doppler method and the SRTM 1 arc-second DEM.

Several speckle filters were tested to determine which filters are most suited for the study area. According to Lee et al. (1994), speckle filters should be compared according to the following parameters: homogeneous and heterogeneous areas; speckle reduction; edge sharpness; thin feature preservation; point target retention. The speckle filters of interest were Refined Lee, Lee Sigma and IDAN. Visual inspection was performed in analysing each of the speckle filters as performed on the KompSAT-5 image. The conclusion was that the speckle reduction of the Lee Sigma (7x7) filter was better than the Refined Lee filter, where the latter looked noisier. The IDAN filter smoothed out almost all of the speckle but essential details of features appeared to be lost, especially details concerning the small-scale mines.

Single-date speckle filtering was applied to single-date Sentinel-1 and KompSAT-5 images, whereas a multi-temporal Lee Sigma (7x7) filtering was applied to the Sentinel-1 image of 12 August 2018 that incorporated the whole 13-image stack for Experiment 1. Experiment 2 incorporated the multi-temporally filtered Sentinel-1 image that was already prepared for Experiment 1. Speckle filtering was applied per polarization for each image and is summarized as follows: Sentinel-1 single-date on two polarizations (VH and VV), KompSAT-5 on one polarization (VH), and Sentinel-1 multi-temporally filtered on two polarizations (VH and VV). All the filtered backscatter bands were then converted to decibel (dB) for further analysis.

3.3 TRAINING AND REFERENCE DATA COLLECTION

Feature extraction was performed following the pre-processing procedures of the SAR data. The segmentation process, image texture calculation and the extraction of geometric attribute and statistics are explained below.

3.3.1 Multiresolution segmentation

Multiresolution segmentation (MRS) was performed on the backscatter bands (VH and VV) of the S1-MT database using eCognition (v9.1). Segmentation was done on the SAR imagery instead of the optical imagery because of the restriction of the availability of cloud-free optical imagery for the study area close to the date of interest. Segmentation was run six times to establish the best parameters to get the most useful objects. The parameters tested were shape, scale and

compactness. Visual inspection was applied to select the most suitable segmentation results which are the slight over-segmentation of the water pools. Examples of the segmentation results are shown in Figure 3.4. A)-C) were under segmented, D) was over segmented, and E) was deemed satisfactory with slight over-segmentation with the parameters shape, scale and compactness of 0.7, 3 and 0.8.

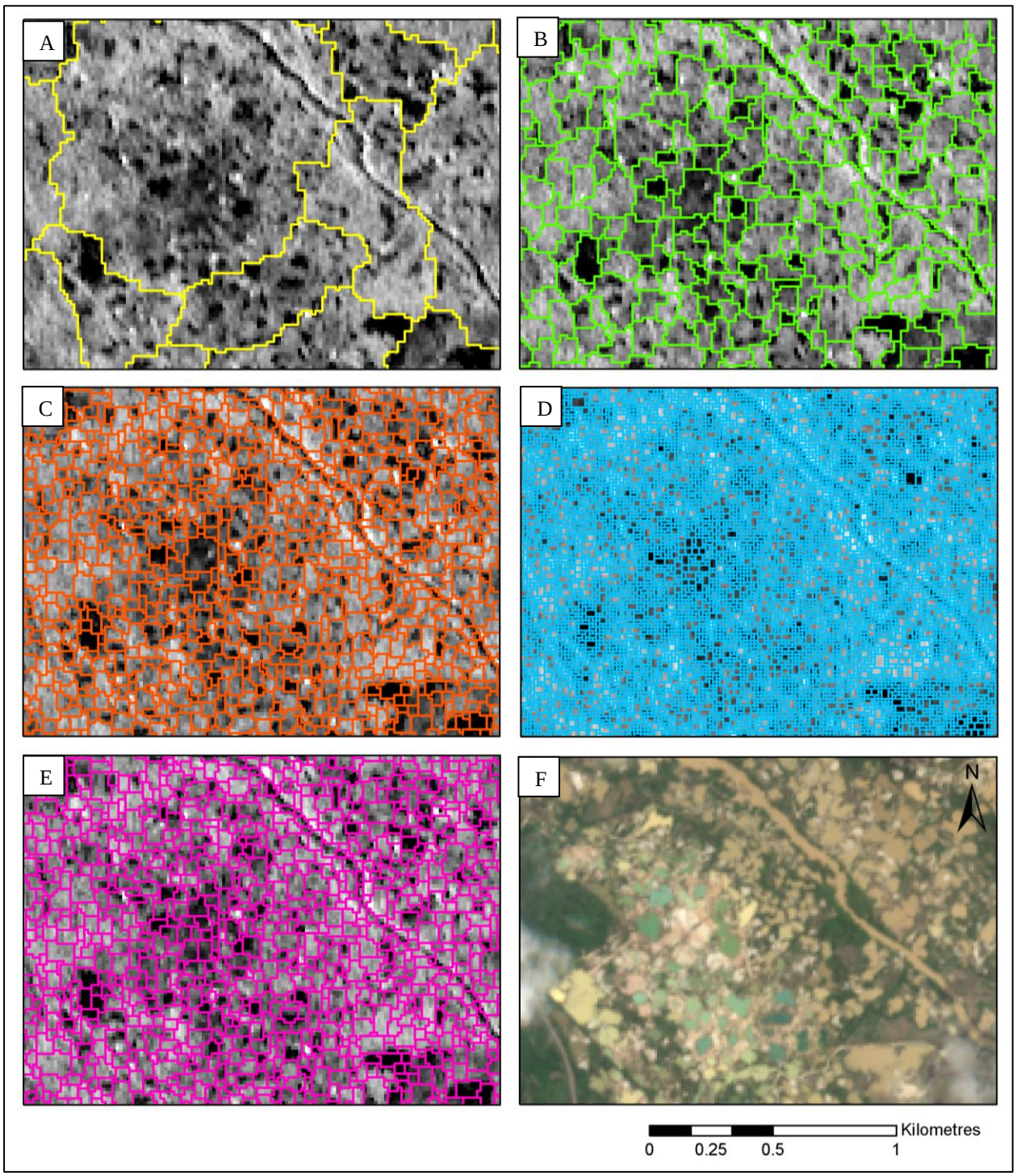

Figure 3.4 Comparison of different parameters of multiresolution segmentation performed on VH and VV of S1-multi on a zoomed-in subset of the image. Scale, shape and compactness values of A) 30, 0.5, 0.5 B) 5, 0.5, 0.5 C) 3, 0.5, 0.8 D) 1, 0.7, 0.8 E) 3, 0.7, 0.8. F is the true colour image of Sentinel-2 RGB 4-3-2 of the same area. A)-C) were under segmented, D) was over segmented, and E) was deemed satisfactory with slight over-segmentation.

3.3.2 Image texture

Image texture was derived from the different datasets to be included as additional features for the training of the classification algorithms. Image texture is a derived feature that is defined as the measure of the variation in the intensity of a surface. Grey-level co-occurrence matrix (GLCM) texture was calculated for each backscatter band using PCI Geomatica's TEX algorithm in the Modeler application. The following eight texture measures were calculated: homogeneity, contrast, dissimilarity, mean, variance, entropy, angular second moment (ASM), and correlation.

3.3.3 The extraction of geometric attribute and object statistics

The geometric attributes of the objects as derived from the multiresolution segmentation were also included as features within the dataset. These were count, rectangularity, length/width, compactness, and roundness, adding five features (per polarisation). A summary of the features used is presented in Table 3.2.

The mean value of each object was calculated with the Zonal Statistics tool in ArcMap (v1.5). In other words, the mean of the backscatter bands, texture bands and geometric attributes were calculated for each object from the segmentation results.

Table 3.2 Summary of the image features used as input for the classification analysis. (S1=single date Sentinel-1, K5=single date KompSAT-5, S1-MT=multi-temporally filtered Sentinel-1).

Image	Backscatter bands	Texture features	Geometric attributes	Total number of features
S1	VH, VV (n=2)	homogeneity, contrast, dissimilarity, mean, variance, entropy, ASM, and correlation (n=16)	Count, Rectangularity, Length/Width, Compactness, Roundness (n=5)	23
K5	VH (n=1)	homogeneity, contrast, dissimilarity, mean, variance, entropy, ASM, and correlation (n=8)	Count, Rectangularity, Length/Width, Compactness, Roundness (n=5)	14
S1-MT	VH, VV (n=2)	homogeneity, contrast, dissimilarity, mean, variance, entropy, ASM, and correlation (n=16)	Count, Rectangularity, Length/Width, Compactness, Roundness (n=5)	23

3.3.4 Sample collection

Samples were selected to use as input for the training and testing of the machine learning classifiers. Samples were collected on the S1-MT image by selecting objects from the segmentation results and visually confirming with the Sentinel-2 image to which class the object belongs. Two classification scheme designs were tested. The first classification scheme was a multi-class classification scheme that consisted of the following classes: water, bare ground, vegetation and built-up. The second classification scheme was a binary-water classification scheme consisting of the classes: water and non-water. The “non-water” class samples were derived from the “bare ground”, “vegetation” and “built-up” classes of the multi-class

classification scheme. The descriptions of each class are listed in Table 3.3. The number of samples collected was 197 per class. Thus, the multi-class classification database consisted of 788 samples and the binary-water classification database of 394 samples.

Table 3.3 Descriptions of each class.

Multi-class classes	**Binary-water classes**	**Description**
Water	Water	Uniform texture. Blue, green pixels.
Built-up	Non-water	Built structures such as roads, dam walls and buildings. Can be grey in colour or brown.
Vegetation		Forest: Densely packed trees usually of a dark green colour. Have a 'speckled' texture. Low vegetation: Usually located in patches of lighter green areas between darker green (forest/tree) areas. Vegetation refers to grass, bushes, low trees.
Bare ground		Open areas that contain no structures or vegetation. Typically a dark brown/brown/orange colour or grey colour.

3.4 EXPERIMENT 1: COMPARISON OF SAR DATASETS

Experiment 1 is aimed at evaluating various SAR datasets and filtering levels for the purpose of detecting small-scale mines and addressed Objectives 3 and 4. Objective 3 was to compare classifications based on single-date KompSAT-5 (K5) and Sentinel-1 (S1). Objective 4 was to evaluate the impact of multi-temporally filtering of Sentinel-1 (S1-MT).

3.4.1 Image classification

The classification was done using the Scikit-learn (sklearn) Python libraries. The workflow of Experiment 1 is as follows: First, the data is imported in CSV format then the features are split according to the training set (X) and the predictions vector (y) which is the "Class". The convention of using X and y means that the values in the X dataset are used to predict the values in the y dataset. The data contained in "Class" is categorical and needs to be converted to number format. The LabelEncoder class of sklearn was used to transform the data. The dataset is now ready to be split into the training and testing datasets. To split the data the train_test_split function is used from the model_selection class of sklearn. X and y are split into X_train, X_test, y_train and y_test

according to an assigned test size percentage. For this project, the test size was set to 40% where the samples were selected according to a stratified random approach. The dataset was split with each run of the classifier.

The classification was then applied by using the RandomForestClassifier class from Sklearn and the hyperparameters were set as follows: the number of estimators was set to 500, the tree splitting criterion was entropy and the oob_score was set to True. The RF classifier is then fitted to the X and y training datasets so that training of the classifier is initiated. The classifier was run 1000 times to get a representative range of the performance of classification for each dataset. The trained classifier is then used to predict the test dataset (y_test) by applying the learnt classification to the test dataset (X_test). Both the test results and training feature information are used for validation.

3.4.2 Accuracy Assessment

The accuracy assessment was done through a confusion matrix for each classifier. The average of each position in the confusion matrix was calculated from the 1000 iterations of the classifier to create a derived confusion matrix for each classification scheme.

Figure 3.5 demonstrated the positions calculated to populate the confusion matrices for each classification algorithm run on both classification schemes.

		Predicted class				
		Water	**Vegetation**	**Bare ground**	**Built-up**	**Total**
Reference class	**Water**	A	B	C	D	
	Vegetation	E	F	G	H	
	Bare ground	I	J	K	L	
	Built-up	M	N	O	P	
	Total					

		Predicted class		
		Water	**Non-water**	**Total**
Reference class	**Water**	A	B	
	Non-water	C	D	
	Total			

Figure 3.5 A demonstration of the positions calculated to populate the confusion matrices for each classification algorithm run on both classification schemes.

3.5 EXPERIMENT 2: COMPARISON OF CLASSIFICATION ALGORITHMS

Experiment 2 is aimed to address Objective 5 with the comparison of five machine learning classification algorithms to determine their relative performance in detecting SSM. The two classification schemes were also compared during this experiment. The Area Under the Curve (AUC) method was used to analyse the statistical significance between the different classification algorithms.

Image classification was done with the same methodology as in Experiment 1. Each classifier was run separately for both classification schemes and the test set size remained at 40%. The dataset was split with each run of the classifier and the classifier ran 1000 times. The outputs for the accuracy assessment are the average values compiled from each run. All classifiers were trained using the same set of input features of S1-multi as in Experiment 1 which included intensity bands, texture layers, and the geometric features. The classifiers tested were:

1. RF: Random forest (results were taken from Experiment 1);
2. DT: Decision trees;
3. SVM: Support vector machine (with linear kernel function);
4. C-SVM: Kernel support vector machine (with RBF kernel function); and
5. KNN: K-nearest neighbour

Confusion matrices were created for each classifier and classification scheme to measure the relative performance of each classifier. The values in the confusion matrices are average values derived from the 1000 iterations of each classification as explained in Section 3.4.2.

The statistical significance was measured with the area under the curve method (Equation 3.1) that is based on probability assessment. The standard normal value (z) together with the confidence level, which was set at 95%, is then used to get the probability from the probability tables that can be found at Statistics How To (2019). The higher the probability is, the larger is the area under the curve and thus the more significant the result is.

$$z = \frac{x - \mu}{\sigma}$$ Equation 3.1

where μ is the mean;

σ is the standard deviation

z is the standard normal

The z-scores were calculated using the means and standard deviations of the overall accuracy results of each classifier on the multi-class classification scheme.

3.6 RESULTS

3.6.1 Experiment 1: SAR dataset comparison

Figure 3.6 shows the overall accuracies and kappa values for the results of Experiment 1. The S1-MT dataset has the highest overall accuracy at 73.60% for the multi-class classification scheme and S1 has the highest overall accuracy at 90.93% for the binary water classification scheme. However, the S1-MT dataset has the highest kappa coefficients at 0.65 and 0.82 for the multi-class classification scheme and binary-water classification scheme respectively. The K5 dataset yielded the lowest overall accuracy and kappa coefficients at 80.61 and 0.61 respectively for the binary-water classification scheme.

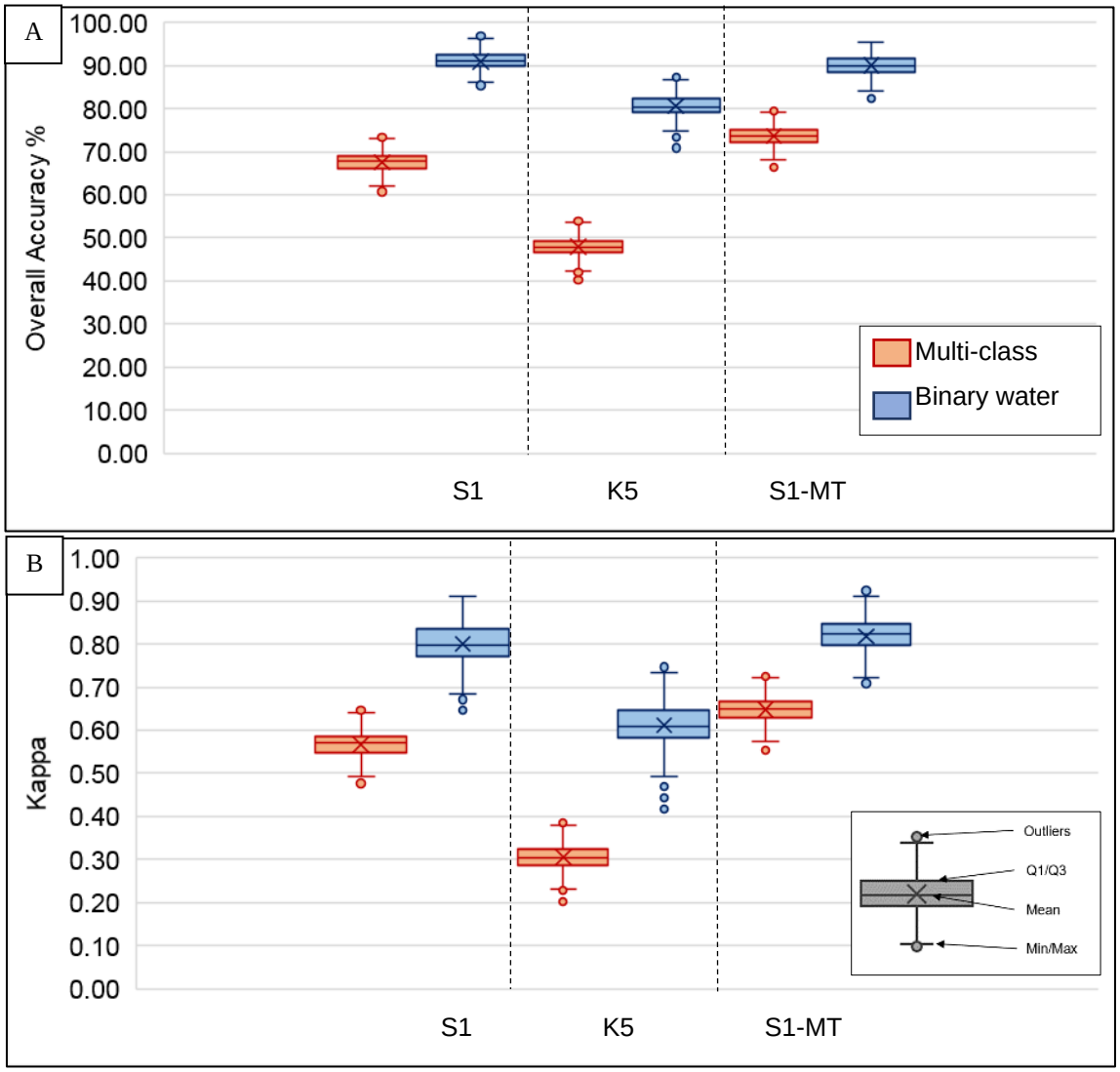

Figure 3.6 Graphs displaying the overall accuracy (A) and kappa coefficient (B) results for Experiment 1.

Table 3.4 summarizes the producer's and user's accuracies for the "water" class with RF between the datasets. The S1-MT dataset PA is 2.28% and 20.76% higher, and the UA 2.61% and 21.57% higher than S1 and K5 respectively for the "water" class of the multi-class classification scheme. The S1-MT dataset also outperformed the S1 and K5 datasets with the binary-water classification scheme at 1.58% and 11.05% higher PA, and 0.33% and 9.49% higher UA for S1 and K5 respectively.

Table 3.4 Producer's (PA) and user's accuracies (UA) of the "water" class for RF classification on the S1, K5, and S1-MT datasets. The highest PA results are highlighted in red.

Dataset	Classification scheme			
	Multi-class		Binary-water	
	PA %	UA %	PA %	UA %
S1	85.06	78.61	91.44	88.96
K5	66.58	59.65	81.97	79.80
S1-MT	87.34	81.22	93.02	89.29

The average error of omission and commission values summarized in Table 3.5 confirms why the multi-class classification scheme performed poorly compared to the binary-water classification scheme. For the S1-MT dataset 26.40% of reference sites were left out (omitted) and 26.26% of the objects were incorrectly classified (committed) for the multi-class classification scheme compared to 9.07% omission error and 9.00% commission error for the binary-water classification scheme. The individual confusion matrices for all three datasets and both classification schemes are listed in Appendix A.

Table 3.5 The average omission error and commission errors are presented in percentage for each dataset and classification scheme.

Dataset	Classification Scheme			
	Multi-class		Binary-water	
	OE %	CE %	OE %	CE %
RF S1	32.49	32.91	9.96	9.93
RF S1-MT	26.40	26.62	9.07	9.00
RF K5	52.10	52.72	19.39	19.39

3.6.2 Experiment 2: Classification algorithm comparison

Figure 3.7 shows the overall accuracies and kappa values for the results of Experiment 2. RF outperformed all the classifiers with an average overall accuracy of 73.60% and 90.04% for the multi-class classification scheme and binary-water classification scheme respectively. The second-best performing classifier was C-SVM with an average overall accuracy of 70.15% and 89.17% for the multi-class classification scheme and binary-water classification scheme respectively. SVM and C-SVM performed very similarly, and DT and KNN yielded the lowest overall accuracy

and kappa coefficients. RF was significantly better than the other classifiers according to the area under the curve method. Random forest has the highest probability score at 0.87 where decision trees have the lowest probability score of 0.12. The probability results are displayed in Table 3.6.

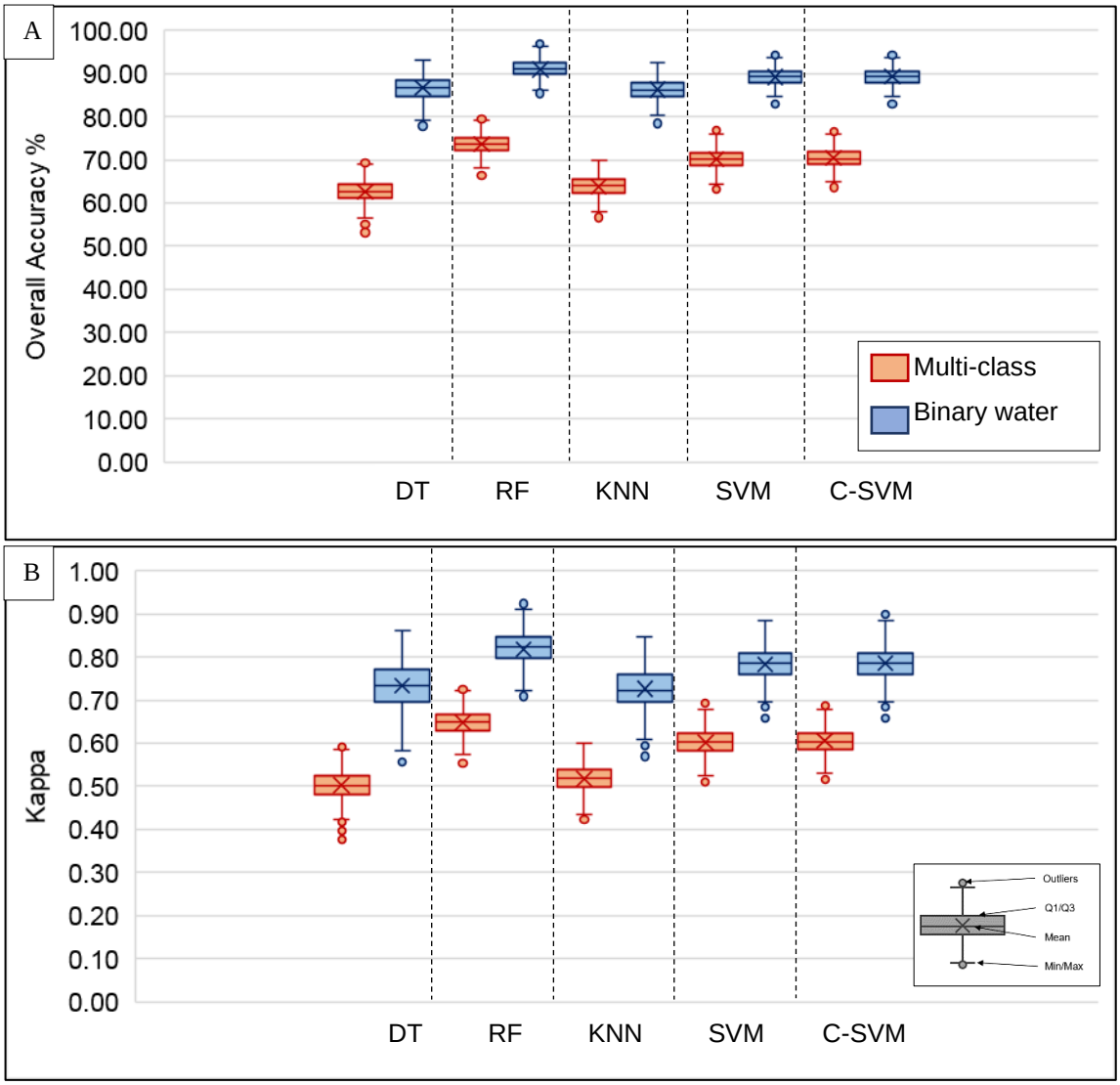

Figure 3.7 Graphs displaying the overall accuracy (A) and kappa coefficient (B) results for Experiment 2.

Table 3.6 The significance evaluation results for each classifier given in probability that was obtained through the area under the curve method. The highest probability is highlighted in red.

OA multi-class	DT	RF	KNN	C-SVM	SVM	MEAN (μ)	STD DEV (σ)
Ave OA of each classifier (x)	62.37	73.54	63.79	70.17	70.36	68.05	4.75
z-value	-1.19	1.16	-0.90	0.45	0.49		
Area (probability)	0.12	0.87	0.19	0.67	0.68		

Table 3.7 summarizes the producer's and user's accuracies of the "water" class classification on S1-MT of DT, RF, KNN, SVM, and C-SVM. RF had the highest PA and UA results except for the UA of the multi-class classification scheme that belongs to SVM. The RF classifier is 3.9% higher in PA than the second-best result of C-SVM for the multi-class classification scheme and 10.85% higher in PA than DT that has the lowest result. For the binary-water classification scheme, RF outperformed C-SVM with 1.67% in PA and DT again with the lowest result at 6.44% lower than the PA of RF. The UA in the multi-class classification scheme was the highest at 81.87% for SVM, 0.65% better than the UA of RF, the UA of SVM is also 10.95% higher than the UA of KNN that gave the lowest result. The UA in the binary-water classification scheme was the highest for RF at 89.29%, with a 0.25% difference to SVM and 3.35% difference to KNN, again the lowest result.

Table 3.7 Producer's (PA) and user's accuracies (UA) of the "water" class classification on S1-MT of DT, RF, KNN, SVM, and C-SVM. The highest PA results are highlighted in red.

Classifier	**Classification scheme**			
	Multi-class		**Binary-water**	
	PA %	**UA %**	**PA %**	**UA %**
DT	76.49	76.68	86.58	86.71
RF	87.34	81.22	93.02	89.29
KNN	81.65	70.97	86.81	85.94
SVM	82.03	81.87	89.69	89.04
C-SVM	83.44	76.94	91.35	87.53

Figure 3.8 visually shows the RF classification results on the multi-temporally filtered S1 dataset (S1-MT). Figure 3.8 (A) shows the multi-class land cover classification map where blue is water, green is vegetation, orange is bare ground and grey is built-up. The image indicates that built-up and bare-ground is incorrectly classified in the vegetation and river areas. The confusion matrix in Table 3.8 confirms high errors of commission for bare ground and built-up at 38.88% and 18.50% respectively. The water binary land cover classification map (B) clearly shows the extent of water pools along the river and stretching into the vegetated areas. The reduction of classes from four to two led to more accurate results. The confusion matrices for each classification algorithm and classification scheme is listed in Appendix A.

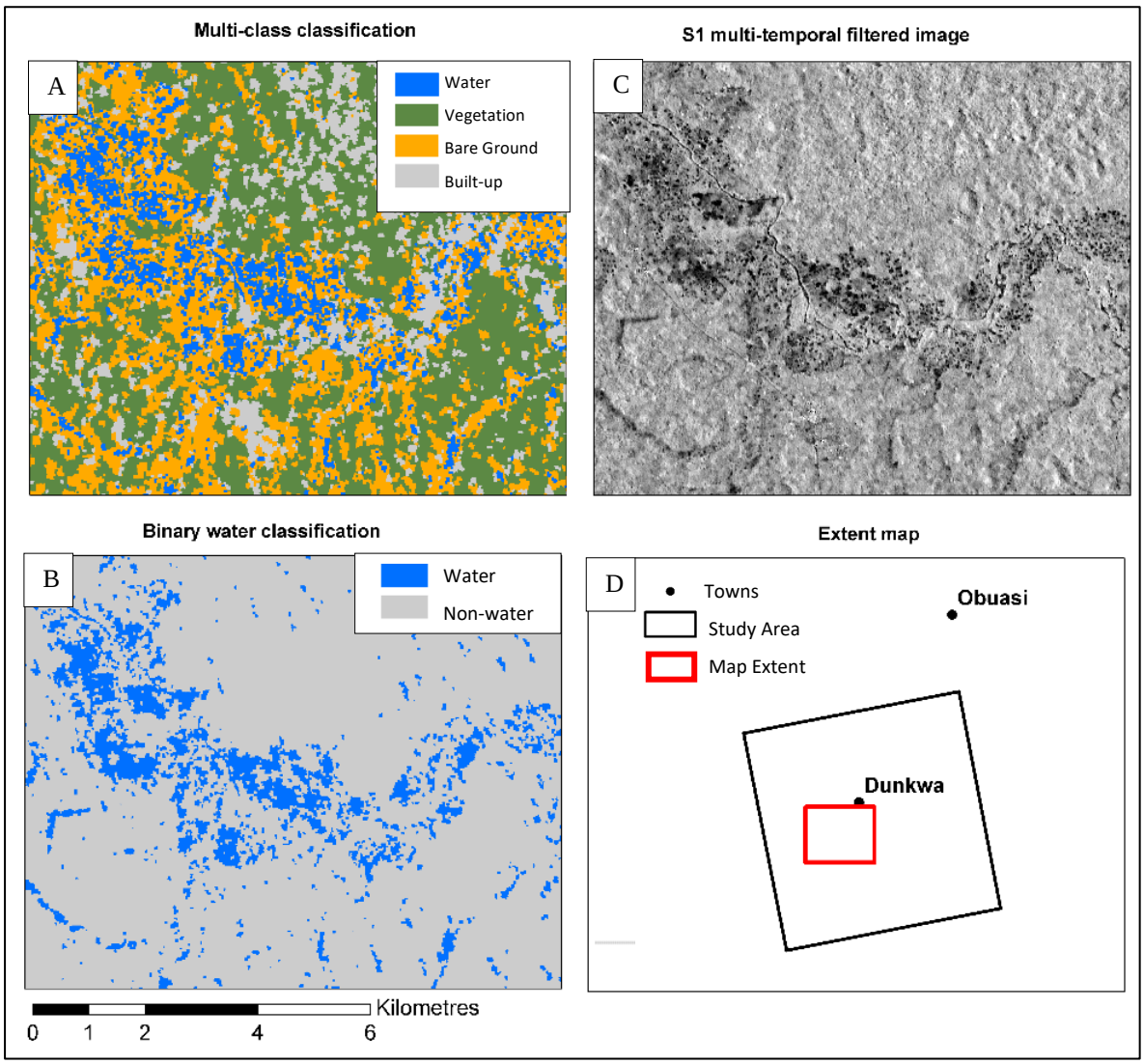

Figure 3.8 Example of visual RF results of S1-MT where: A) is the multi-class classification, B) the binary water classification, C) the intensity of S1-multi and D) the map showing the extent of the images in A, B, C. Blue is water, green is vegetation, orange is bare ground and grey is built-up.

Table 3.8 Random forest multi-class classification on S1-MT confusion matrix. EC % of bare ground and built-up is highlighted in red.

	Water	Vegetation	Bare ground	Built-up	TOTALS	PA %	EO %
Water	69	0	9	1	**79**	87.34	12.66
Vegetation	1	57	13	8	**79**	72.43	27.57
Bare ground	12	17	45	5	**79**	57.13	42.87
Built-up	3	8	7	61	**79**	77.47	22.53
TOTALS	**85**	**82**	**74**	**75**	**316**		
UA %	81.22	69.70	61.12	81.50			
EC %	18.78	30.30	38.88	18.50			
Overall accuracy	73.60						
Overall kappa	0.65						

3.7 DISCUSSION

For Experiment 1 the multi-class classification scheme yielded unreliable results where the average kappa coefficient for all datasets and classification algorithms was 0.54 as shown in Table 3.9. The binary-water classification scheme gave reliable results with an average kappa coefficient of 0.75. With the multi-class classification scheme mixing of the classes took place as can be seen in Figure 3.8, whereas the binary-water classification could clearly distinguish between the water objects and the non-water objects.

Table 3.9 A summary of the averaged values for the results of Experiment 1 and 2. The highest kappa values are highlighted.

Classifier/ dataset	Classification Scheme			
	Multi-class		Binary-water	
	OA %	K	OA %	K
RF K5	47.90	0.31	80.61	0.61
RF S1	67.51	0.57	90.93	0.80
RF S1-MT	73.60	0.65	90.04	0.82
DT	62.65	0.50	86.65	0.73
SVM	70.42	0.61	89.33	0.79
C-SVM	70.15	0.60	89.17	0.78
KNN	63.84	0.52	86.30	0.73
Average	65.15	0.54	87.58	0.75

By comparing the classification results of the full S1 sensor with those from K5 the difference in wavelength is evident. The X-band K5 imagery yielded significantly lower accuracies than the C-band S1 imagery which may be due to the shorter wavelength of K5 which is less sensitive to differences in roughness between the land cover classes. To test this, an additional classification was done with just the VH bands of S1, and S1-MT. The results showed that the overall accuracy and kappa coefficient results for Sentinel-1 are less accurate than the full sensor results but still more accurate than the K5 results. There is also a bigger difference in overall accuracy and kappa coefficient for the multi-class classification scheme than the binary-water classification scheme. This further supports the notion that C-band is better suited for this application than X-band, even at a lower resolution.

The radiometric calibration of K5 may also be of influence to the weak results. Comparing multi-temporally filtering with single date filtering showed that S1-MT performed more accurately with margins less than 3% producer's accuracy for the multi-class classification and margins less than 2% PA for the binary-water classification. Multi-temporal filtering reduces the amount of speckle but the difference in UA and PA between S1 and S1-MT is negligible.

Confusion exists within the multi-class classification scheme especially between water and bare ground. This is evident by the high omission and commission errors produced by this classification scheme. With the S1 imagery, the water class and the bare ground class are mixed at the ASM sites around the river due to lower resolution than the K5 imagery. Therefore, the binary-water classification scheme obtained significantly higher accuracies due to the elimination of the confusion. This is confirmed by the low omission and commission errors of the binary-water classification scheme.

The same trend as in Experiment 1 occurs in Experiment 2 where the binary-water classification scheme outperforms the multi-class classification scheme. The margins between the highest performing dataset and lowest-performing dataset for the multi-class classification scheme is around 21 % where the margins for the binary-water classification scheme is around 10%. The margins between the highest performing classifier for the multi-class classification scheme is less than 11 % and the margins for the binary-water classification scheme is less than 7%. The high margins of the multi-class classification scheme are because of the misclassification of classes that took place during the multi-class classification.

For Experiment 2 the random forest classifier was significantly more accurate than the other classifiers with a probability of 0.87 at 95% confidence level. Random forest is the most robust of the machine learning algorithms and deals very well with high dimensionality and complex data. C-SVM and SVM also achieved high overall accuracies where C-SVM outperformed SVM. This is likely because the data structure was of a higher dimensionality where the C-SVM kernel could find a better fit for the hyperplane to group the data. The decision trees classifier gave the least accurate as well as the least reliable results. This is because of how the trees are split in the algorithm that is not iterated through such as with random forest. KNN is the simplest of the algorithms and performed slightly better than decision trees. KNN is not robust with high dimensionality and complex data.

To conclude, for the comparison of the different SAR sensors the C-band Sentinel-1 image outperformed the X-band KompSAT-5 image in accuracy and reliability. The KompSAT-5 image performed substandard for both classification schemes with an OA of less than 60% and a kappa coefficient of less than 0.6. Both SAR sensors could only classify the waterbodies associated with SSM. Both single-product speckle filtered SAR and multi-temporally filtered SAR produced very accurate and reliable results, however, the S1-MT database had a smaller range in the difference between the results of the multi-class classification scheme and the binary-water classification scheme. For this reason, multi-temporal filtering improves the overall reliability of the classification results. The comparison of the machine learning classification algorithms showed

that RF is the best-suited algorithm to map SSM with SAR imagery, however, SVM came a close second. The influence of the custom kernel for SVM was insignificant, therefore can be deemed as unnecessary. The DT and KNN algorithms had the poorest performance and are not suitable for SSM mapping with SAR.

The classification methods proved that a multi-class classification approach for using SAR to map illegal mining in forested areas does not work well. The binary-water classification scheme gave highly accurate and reliable results especially with the multi-temporally filtered Sentinel-1 imagery and the random forest classifier. The resulting classifications only mapped the waterbodies in the image and the actual SSM activities were not mapped yet. This is however very useful because of the association of alluvial illegal mining with waterbodies.

4 CHAPTER 4: THE EVALUATION OF THE POTENTIAL OF CHANGE DETECTION FOR DETECTING SMALL-SCALE MINING

This chapter is aimed at addressing Objective 6 with Experiment 3 where change detection is applied to a time series of Sentinel-1 imagery. An overview of the data acquired is given, followed by the preparation of the data. The methodology of the experiment is given and lastly, the results are shown and discussed.

4.1 DATA ACQUISITION

The imagery was acquired during the dry season of Southern Ghana which is from middle November to February. The dry season was chosen to mitigate the effect of events such as floods and heavy rainfall on the SAR imagery change analysis. A secondary reason is that optical imagery used for validation have the least amount of cloud cover during the dry season. Even then acquiring images with a low amount of cloud cover was challenging.

Experiment 3 uses Sentinel-1 C-band ground range detection (GRD) interferometric wide swath (IW) images, with a swath width of 250 km and moderately high spatial resolution at 10 m as well as dual-polarization vertical transmit, horizontal receive (VH) and vertical transmit, vertical receive (VV). The Sentinel-1 GRD IW imagery was acquired through Google Earth Engine. The image dates of interest were the first available SAR image of the year from 2016 to 2019 to yield a collection of four images for change analysis.

The optical imagery used for validation in this experiment was Landsat-8. Landsat-8 had more cloud-free imagery available than Sentinel-2 for the validation. The Landsat-8 imagery was downloaded from the USGS Earth Explorer website. Level-2 atmospherically corrected Landsat-8 (L2A) can readily be downloaded, but the panchromatic band is not included. Therefore, the corresponding level-1 (L1A) imagery was downloaded for the panchromatic band. The bands used for validation was the L2A bands 2 to 5 at 30 m resolution and the L1A panchromatic band 8 at 15 m resolution. Both levels of Landsat-8 imagery were downloaded for each year of the time series, from 2016 to 2019, and cloud-free imagery closest to the date of the Sentinel-1 imagery was selected. This resulted in eight stacks of imagery for the four years. The SAR and optical imagery are summarized in Table 4.1.

Table 4.1 Summary of the satellite imagery for Experiment 3. Acquisition parameters of the SAR data and optical imagery is listed.

Sensor	Mode	Polarization	Incidence angle	Dates acquired	Resolution	Description
Sentinel-1	GRD IW	VH, VV	32.9º - 43.1º	2016 (2016/01/07) 2017 (2017/01/01) 2018 (2018/01/03) 2019 (2019/01/03)	10 m	GRD IW C-band VH, VV
Landsat-8	L2A, L1A	n/a	n/a	2016 (2015/12/29) 2017 (2016/12/31) 2018 (2018/01/03) 2019 (2019/01/06)	30 m, 15 m	L2A bands 2 to 5, L1A panchromatic band 8

4.2 DATA PREPARATION

This section describes the pre-processing procedures followed in order to prepare the SAR and optical data for the change detection analysis and validation. The time periods that were taken into account for the change detection analysis were 2016-2017, 2017-2018, 2018-2019, and 2016-2019. The purpose of the change detection analysis over each consecutive year as well as for the whole period is to have an estimate of the consistency of the changes over the four-year period. Each pair of years are referred to as a difference-year from this point forward.

4.2.1 Pre-processing methods

The Sentinel-1 imagery was already pre-processed before being loaded into Google Earth Engine (Gorelick et al 2017). The pre-processing was done using the S1-toolbox and the following steps were applied:

1. Thermal noise removal
2. Radiometric calibration
3. Terrain correction (using SRTM 30 DEM and ASTER DEM where SRTM is not available)
4. Converted to dB

Speckle filtering was not applied to this experiment. The imagery was clipped using Google Earth Engine and then downloaded.

For the Landsat-8 imagery, selected bands from the Landsat-8 imagery were stacked and pan-sharpened using ENVI. The bands that were stacked were bands two to five, and band eight was used for pan-sharpening. The Gram-Schmidt algorithm was used for the pan-sharpening process

which changed the resolution of bands two to five from 30 m to 15 m. The pan-sharpened stack was then clipped to the study area and exported to GeoTIFF format.

4.2.2 Ground truth database creation

The ground truth database consists of 100 samples for each year, where 50 samples were collected for the “change” class and 50 for the “no-change” class. This represents the actual class database. The samples were derived from the Landsat-8 imagery by manually digitizing polygons through visual analysis the polygon was assigned the class “change” or “no change”. The “change” class was assigned when a change of class occurred from one year to the other and the “no change” class was assigned when no change in the class took place from the one year to the other. The class definitions used in this experiment were urban, bare ground, vegetation, water and SSM. The SSM class is defined as a mixture of turned-up soil and water. Figure 4.1 shows examples of how the samples were derived. The class of the polygon in A) is SSM in 2016 and the class of the polygon in B) is SSM in 2019, hence a change of class did not occur and the “no change” class was assigned. The class of the polygon in C) is vegetation in 2016 and the class of the polygon in D) is SSM in 2019. A change of class occurred between C) and D) and therefore the “change” class was assigned. A vector file (shapefile) was created for each difference-year, resulting in four sets of ground truth vector files.

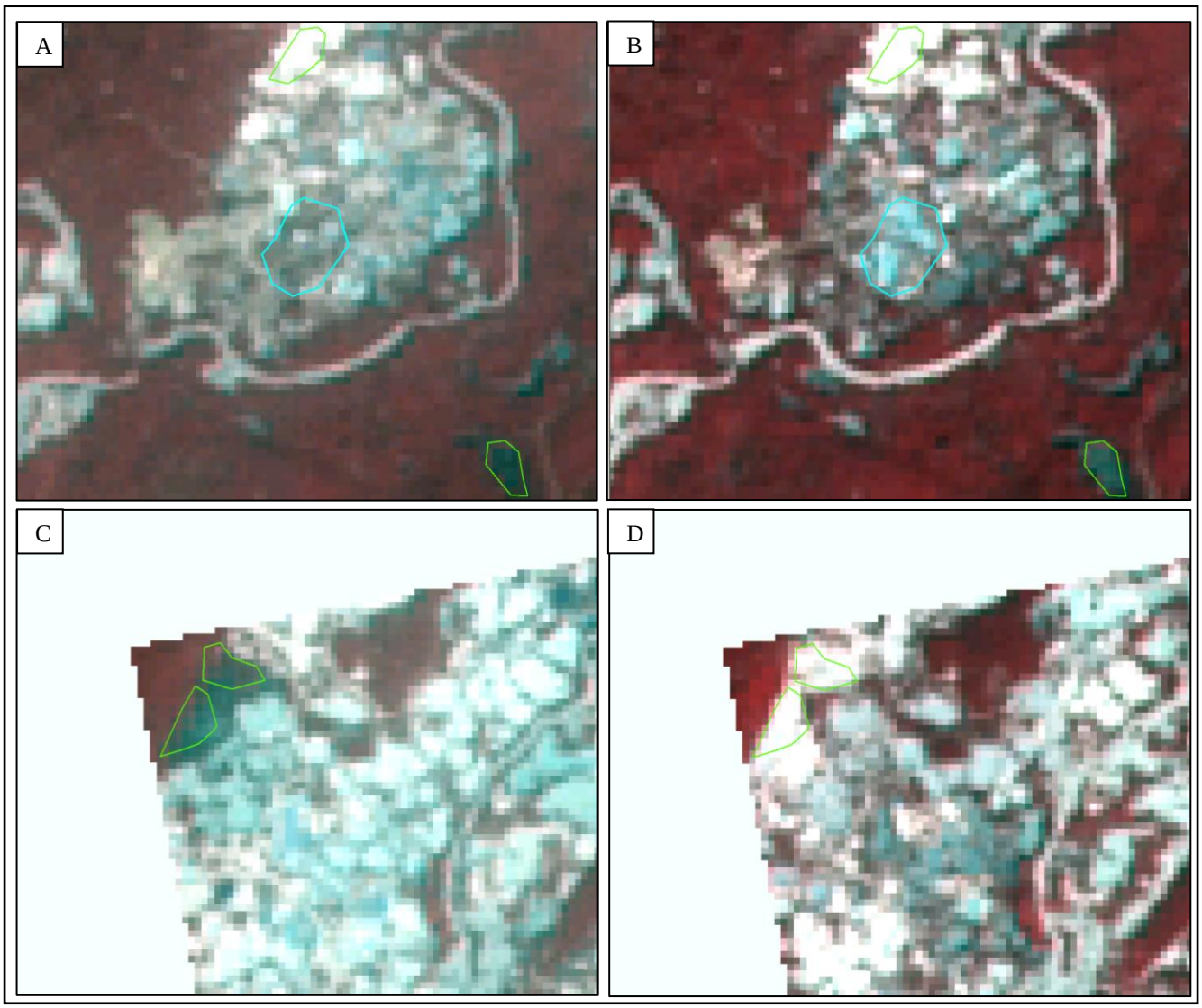

Figure 4.1 Examples of the digitizing of no change and change classes on the Landsat-8 imagery. The class of the blue polygon in A) is SSM in 2016 and the class of the blue polygon in B) is SSM in 2019, hence a change of class did not occurred and the "no change" class was assigned. The class of the polygons in C) is vegetation in 2016 and the class of the polygons in D) is SSM in 2019. A change of class occurred between C) and D) and therefore the "change" class was assigned.

4.3 CHANGE DETECTION

Experiment 3 is aimed to address Objective 6 to analyse whether change detection analysis has the potential to detect SSM. To achieve this the change detection analysis method applied is image differencing over a period of four years. A difference-image is created for each consecutive year as well as over the full period resulting in four difference-images. Difference-images were calculated per backscatter band of the Sentinel-1 imagery: therefore four difference images were created for VH and VV separately resulting in a total of eight difference-image products.

4.3.1 Methodology

Change detection by image differencing was done using the ENVI (v5.5) change analysis workflow which is presented in Figure 4.2. The goal is to map the extent of SSM change.

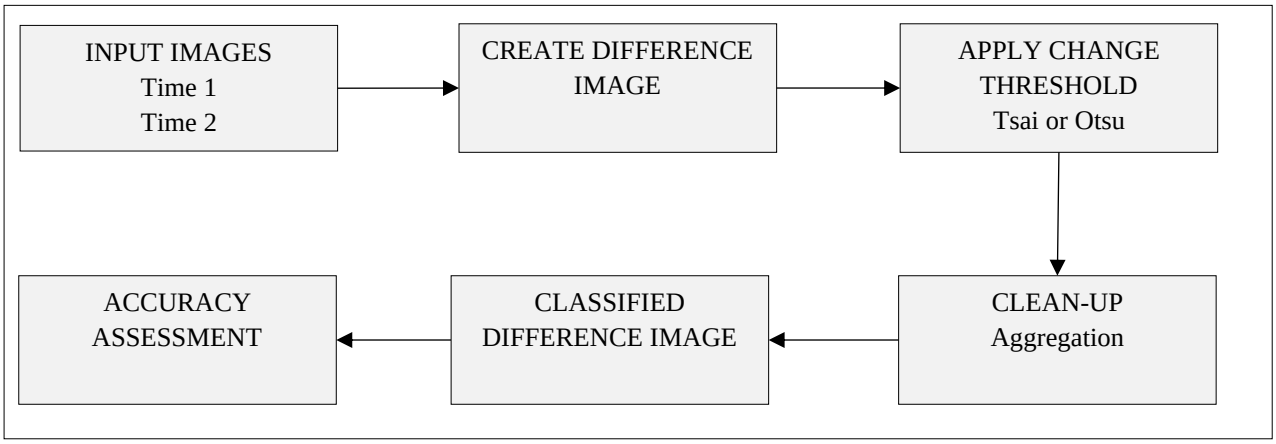

Figure 4.2 Workflow of the image differencing change detection analysis that was done in ENVI. For the input images Time 1 refers to the initial image and Time 2 to the final image.

4.3.2 Change Detection Difference Map

Change detection starts with two input images, the initial image (time 1) and the final image (time 2). The input images are single band images and can be of any data type. The difference image is computed by subtracting the time 1 image from the time 2 image (final minus initial). Higher values in the difference image are interpreted as positive change where the final state brightness was greater than the initial state brightness, and negative change is pixels that have lower values where the final state brightness was less than the initial state brightness (ENVI 1994). For SAR data an increase in pixel value indicates an increase in backscatter intensity while a decrease in pixel value is a decrease in backscatter intensity.

The computed difference image was then classified into “change” and “no change” classes applying automatic thresholding. Two automated thresholding algorithms were tested, Tsai and Otsu and the type of change was selected as increase and decrease. The increase is displayed in blue and a decrease in red (ENVI 1994). As a final step, aggregation was applied to the classified image. Aggregation is aimed at cleaning the thresholding results by aggregating regions of an assigned pixel size or smaller to an adjacent larger region. Different values of aggregation size were tested based on visual inspection as shown in Figure 4.3. The aggregation size of 10 pixels was decided on due to an aggregation value of greater than 10 resulted in a loss of accuracy and a value below 10 created background “noise”.

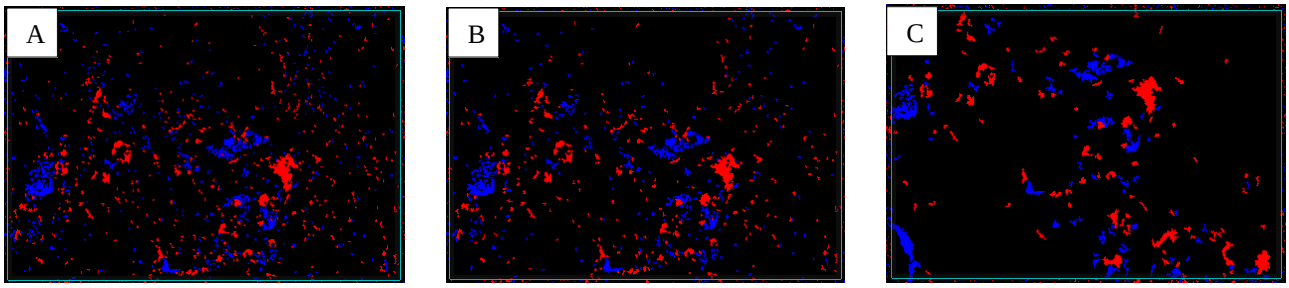

Figure 4.3 A subset of the Tsai classified change image of 2016-2019 VH where visual inspection was applied to analyse the effect of the aggregation size parameter. A) Aggregation=2; B) Aggregation=3; C) Aggregation=10. Blue indicates an increase in backscatter and red a decrease in backscatter.

4.3.3 Accuracy Assessment

The accuracy assessment was conducted by using the ground truth database vector files on the classified change maps for each respective difference-year. Through visual inspection, each polygon was assigned to the "change" or "no change" class to create the predicted class database. When more than 50% of the polygon is covered by blue or red then the polygon is assigned to the class "change", else if the polygon is assigned to the class "no change" (Figure 4.4).

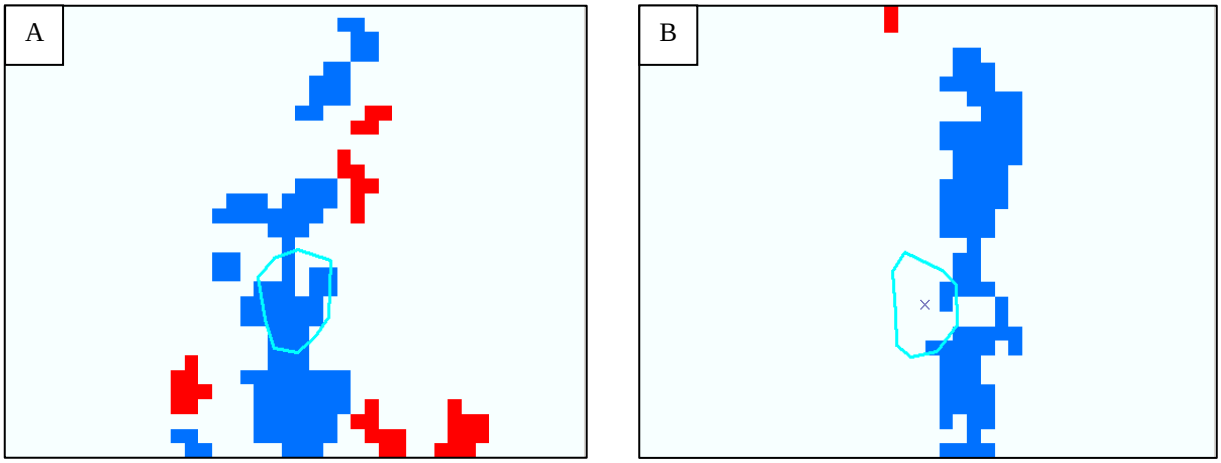

Figure 4.4 A) Example where more than 50% of the polygon is covered by blue or red and is assigned to the class "change". B) Example where less than 50% of the polygon is covered by blue or red and is assigned to the class "no change".

A confusion matrix, which compares the actual class database with the predicted class database, was created for each of the eight difference-images. From the confusion matrix, the following statistical measures were derived: overall accuracy and kappa coefficient.

4.4 RESULTS

A summary of the results of Experiment 3 is presented in this section where the potential of change detection on Sentinel-1 time series data for the detection of small-scale mines was analysed. The results of the two thresholding methods are presented for each time period. Table 4.2 lists the results of all the difference-years as well as the average values for all the years with regards to polarization and automatic threshold method. When the values are averaged for all years, VH has better overall accuracy and kappa for both threshold methods. The kappa coefficient for Tsai on the 2018-2019 difference image was the highest at 0.7 and highlighted in red. The confusion matrices for all change detection results are listed in Appendix B.

Table 4.2 Overall Accuracies (OA), kappa coefficients (K), mean, and standard deviation (σ) values for each difference-year as well as all the years averaged. The kappa coefficient for Tsai on the 2018-2019 difference image was the highest at 0.7 and highlighted in red.

Year	Thresholding								Average			
	VH				VV				OA		K	
	Tsai		Otsu		Tsai		Otsu					
	OA	K	OA	K	OA	K	OA	K	Mean	σ	Mean	σ
2016-2017	77.00	0.54	77.00	0.54	79.00	0.58	67.00	0.34	75.00	5.42	0.50	0.11
2017-2018	80.00	0.60	81.00	0.62	72.00	0.44	76.00	0.52	77.25	4.11	0.55	0.08
2018-2019	85.00	0.70	83.00	0.65	81.00	0.62	84.00	0.68	83.25	1.71	0.66	0.04
2016-2019	71.00	0.42	74.00	0.48	65.00	0.30	73.00	0.45	70.75	4.03	0.41	0.08
All years	78.25	0.57	78.75	0.57	74.25	0.49	75.00	0.50	76.56	2.27	0.53	0.05

A graph displaying the kappa coefficient of the average values of VH and VV for all years for Tsai and Otsu respectively is presented in Figure 4.5. VH achieved an overall accuracy of 78.25% and 78.75% for Tsai and Otsu respectively, where VV achieved an overall accuracy of 74.25% and 75.00% for Tsai and Otsu respectively. The kappa for VH were 0.56 and 0.57 for Tsai and Otsu respectively. The overall accuracy of Otsu is 6% more significant and the kappa is 4.7% more significant than the Tsai results. VH is, however, not consistently better than VV. Based on the average values Otsu performed better than Tsai for both VH and VV polarizations, however, this is also not consistent throughout the data as can be seen in the graphs of the kappa coefficients for Tsai and Otsu per year shown in Figure 4.6 and Figure 4.7. The significance results are listed in Appendix C.

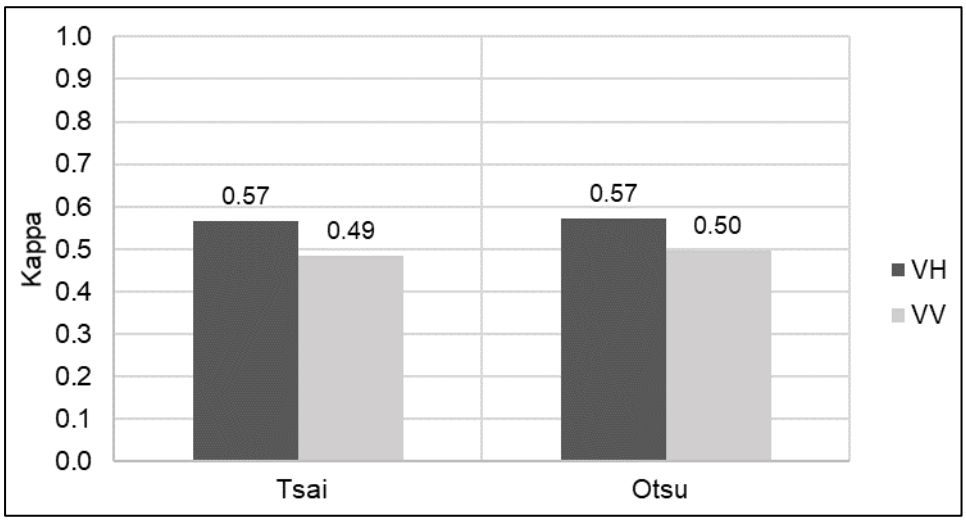

Figure 4.5 Graph displaying the Kappa coefficients of the averaged values of VH and VV over all the years for Tsai and Otsu respectively.

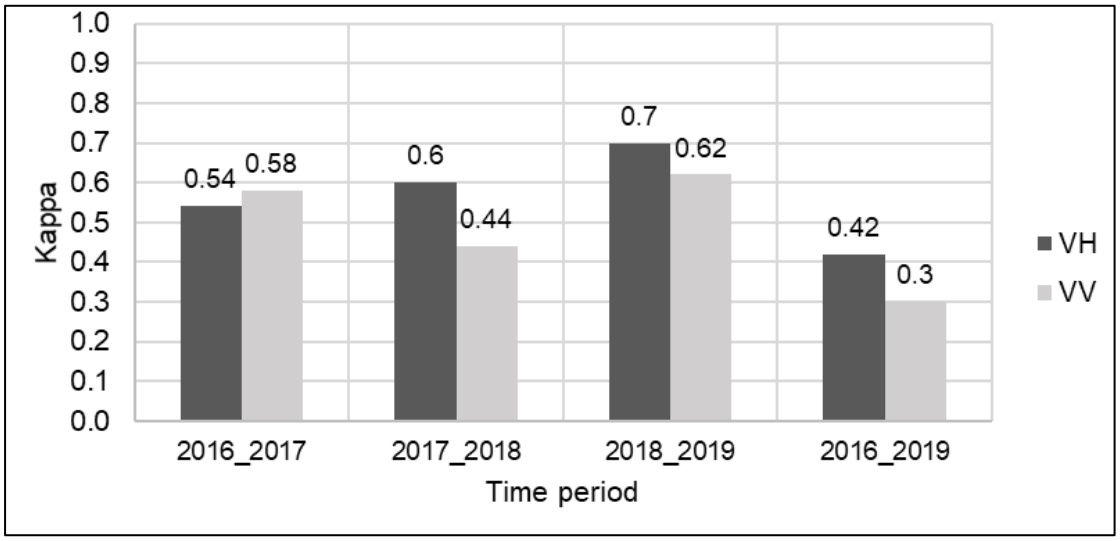

Figure 4.6 Graph displaying the Kappa coefficient for each time period of the Tsai thresholding.

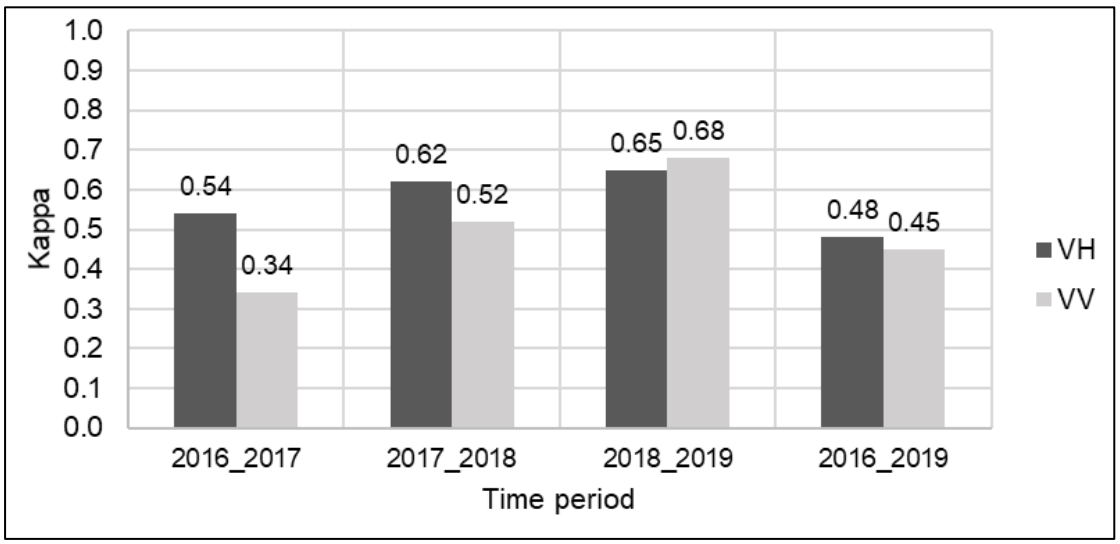

Figure 4.7 Graph displaying the Kappa coefficient for each time period of the Otsu thresholding.

The VV polarization only has a better kappa coefficient once for Tsai (2016-2017) and once for Otsu (2018-2019). The VH polarization follows the same trend for both Tsai and Otsu peaking in 2018-2019 and at the lowest values for 2016-2019. According to these values Otsu outperformed Tsai for most of the years. From the visual results (Figure 4.8) the Tsai threshold maps the small-scale mining activity better than the Otsu threshold. The Otsu threshold gives noisy results.

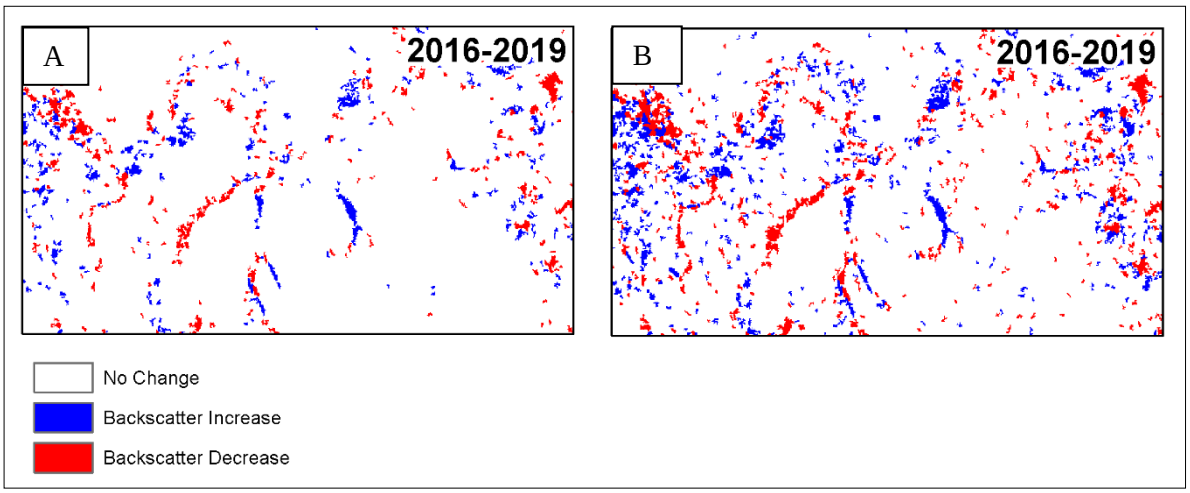

Figure 4.8 Visual comparison of Tsai and Otsu for a segment of the difference map 2016-2019. In A) is Tsai thresholding and in B) Otsu. The blue represents an increase in backscatter from 2016 to 2019 and the red represents a decrease in backscatter. Together the blue and red represent the class “change” whilst the white represents the class “no change”.

Another accuracy assessment test was done to compare the sensitivity of Tsai and Otsu with the Receiver Operating Characteristic (ROC) which compares the false positive rate with the true positive rate. According to the graph in Figure 4.9 the ROC for Otsu indicates that the probability for false positives is less than for Tsai even though Tsai achieved a higher probability for classifying true positives. Taking into consideration that both these values are close to the ideal ROC value of (0, 1) an Euclidean distance estimate revealed that Tsai is closer to the ideal ROC value by 20%. Therefore, this indicates that Tsai is overall a better automatic threshold method than Otsu with the acceptance of a higher false positive rate.

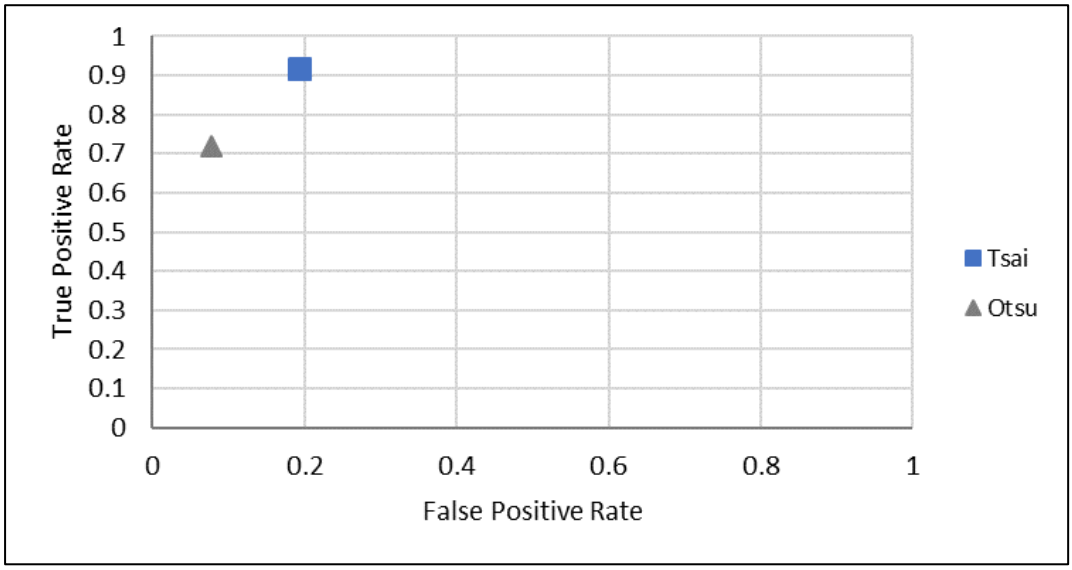

Figure 4.9 The Receiver Operating Characteristic values for Tsai and Otsu did for the difference map 2018-2019 VH polarization.

4.5 DISCUSSION

For the change detection analysis, the two polarizations of the Sentinel-1 GRD imagery were compared. Overall the VH polarization gave higher overall accuracies and kappa values than the VV polarization. This is likely because the VV polarization is more sensitive to surface water roughness and therefore introduces more variance in the change images. This is also evident in the difference images as shown in Figure 4.10 where the VH difference images in A) have greater contrast than the VV difference images in B) and therefore show more information for interpretation. The anomaly where the VV polarization has better kappa coefficients than the VH polarization only occurs once for Tsai and once for Otsu, this may be due to inconsistency during digitizing.

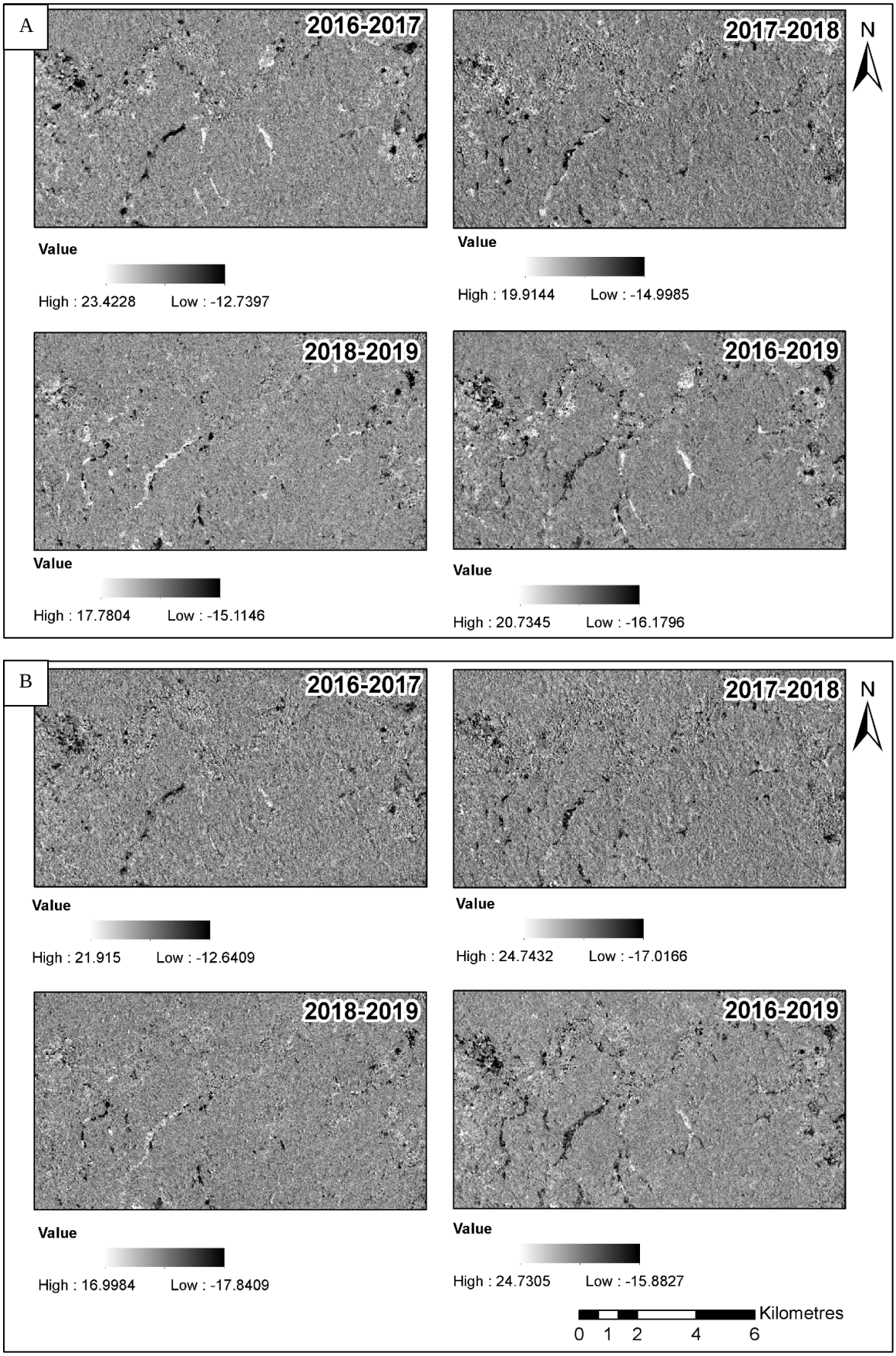

Figure 4.10 A comparison of each band of the Sentinel-1 difference images for all time periods wherein A) the VH difference and B) the VV difference images are shown. The images in A) have greater contrast than the images in B) and therefore show more information for interpretation.

In Experiment 3 the reliability and accuracy of each difference year were compared to the overall difference image (2016-2019). The difference year with the highest kappa coefficients occurred during 2018-2019 for both the Tsai and Otsu thresholding. The kappa coefficient systematically increases for each difference-year from 2016-2017 to 2018-2019 and the kappa coefficient for the overall-difference image (2016-2019) is rather low. A likely reason for the peak in the overall accuracy for 2018-2019 is that this was the last image to be digitised manually for the accuracy assessment. It is possible that the precision of the digitising of training and test samples increased with each difference image which started with the 2016-2019 image. Another reason for the inconsistency in accuracy over all of the difference-images can be due to seasonal variations where higher rainfall may have occurred during one year compared to another. The reason why analysing the change per year is more accurate than an overall change of all the years is because the regrowth of vegetation can take place and this can confuse the classification of change and no-change.

For the analysis of the two thresholds, Otsu outperformed Tsai for most of the years. This may be because the Otsu threshold allowed for more leniency than Tsai and therefore a better overall accuracy was obtained, as well as, the fact that Otsu classifies less false positives than Tsai. However, Tsai classified more true positives and was closer to the ideal ROC value which is more desirable and visually the Tsai threshold is preferable because of the less amount of noise present to create the change detection maps.

To conclude, the Otsu thresholding method had better reliability than the Tsai thresholding method, however, the Tsai thresholding method is preferred for the visual change maps. The 2018-2019 time period was the most reliable and accurate time period, likely due to an increase in the precision of the digitising of the training data. The VH polarization of Sentinel-1 gave better results than the VV polarization for most of the time periods. Change detection can detect SSM with SAR because the “change” class corresponded to the SSM activities. The potential of change detection with Sentinel-1 GRD time series has exceeded expectations by not just detecting SSM but active SSM can be distinguished from passive SSM.

5 CHAPTER 5: CONCLUSION

This chapter provides a summary of the findings of the experiments presented in Chapter 3 and 4 and the research aim and objectives are revisited. The research is evaluated through the contextualization of the study, the discussion of the limitations, and by assessing the impact of the research. Finally, recommendations for future work are made and the concluding remarks are given, including a review on the continuation of the research.

5.1 REVISITING THE AIM AND OBJECTIVES

The aim of this study was to assess the accuracy and reliability of applying SAR for the detection and mapping of small-scale mining in Ghana with supervised classification and change detection approaches. The evaluated approaches were applied to features derived from SAR satellite imagery and validated with optical satellite imagery. The conventional method for determining the spatial distribution patterns of SSM involves field visits and interviews which is time consuming, costly and dangerous considering the nature of SSM environments. The remote sensing methods used for mapping SSM to date relied on scarce cloud-free optical imagery and there is only one study that attempted the mapping of SSM with SAR 20 years ago. It is therefore important to identify methods and derivatives that have the potential of identifying SSM in areas with a high percentage of cloud cover. The main aim was therefore to investigate the potential of SAR and the remote sensing techniques, supervised classification and change detection, for the detection and mapping of SSM in a tropical area.

Objective 1 was to carry out a review of the remote sensing and image processing literature to assess whether these approaches can be used for SSM detection and mapping (Chapter 2). Literature showed that remote sensing with SAR holds much potential for mapping SSM, especially the studies focussing on deforestation monitoring and flood monitoring with SAR. The studies that used optical imagery for detecting SSM could not obtain enough cloud-free imagery to create a sustainable SSM monitoring system, as most of these studies occur in tropical regions such as Peru, the Democratic Republic of the Congo and Ghana. Also, the use of supervised machine learning methods for detecting SSM has not been explored. Although one study used SAR for detecting degradation areas caused by illegal mining, the study did not take into account additional spatial features such as texture measures. The change detection method (image differencing and thresholding) commonly used for flood mapping with SAR showed potential for detecting SSM in time series imagery because water mapping is a common indicator for both floods and SSM.

Objective 2 was to collect satellite imagery over an appropriate study area in which remote sensing techniques can be applied to detect and map SSM. Two types of SAR imagery were acquired for the comparison of SAR sensors in detecting SSM with classification (Chapter 3). Freely available Sentinel-1 imagery was collected to build two time-series databases, one for multi-temporally filtering for the classification analysis (Chapter 3) and the other for the change detection analysis (Chapter 4). The acquired SAR imagery (Sentinel-1 and KompSAT-5) and validation imagery (Sentinel-2 and Landsat-8) for classification and change detection were described in Chapter 3 and 4 respectively. The imagery was acquired for an overlapping area that included a section of the Ofin River close to the mining town Obuasi in Ghana.

Objective 3 was to analyse the accuracy and reliability of random forest classification applied to C-band Sentinel-1 single-date and X-band KompSAT-5 single-date images. **Objective 4** was to analyse the influence of multi-temporally filtering on the accuracy and reliability of random forest classification applied to Sentinel-1 imagery. The first experiment addressed the third and fourth objective by applying random forest classification to three databases in Chapter 3.

Objective 5 involved the comparison of several machine learning algorithms as applied to the multi-temporally filtered Sentinel-1 database, this was done in the second experiment in Chapter 3. The machine learning algorithms were RF, DT, SVM, C-SVM and KNN. The classification algorithms were tested on accuracy and reliability to determine which of the algorithms were the most effective for detecting SSM. The accuracy assessment was done with confusion matrices and the derived statistics.

Objective 6 was to analyse whether SSM can be detected with change detection on a Sentinel-1 time series. This was done in the third experiment in Chapter 4. The change detection method that was selected for this experiment was image differencing and thresholding was applied to the difference imagery to create change maps.

5.2 SUMMARY OF FINDINGS

The main findings of the study are as follows:

1. Single-date Sentinel-1 has the highest overall accuracy at 90.93% for the binary water classification scheme, however, the multi-temporally filtered Sentinel-1 dataset has the highest kappa coefficients at 0.65 and 0.82 for the multi-class classification scheme and binary-water classification scheme respectively. The single-date KompSAT-5 dataset yielded the lowest overall accuracy and kappa coefficients at 80.61 and 0.61 respectively for the binary-water classification scheme.

2. The random forest classifier outperformed all the classifiers with an average overall accuracy of 73.60% and 90.04% for the multi-class classification scheme and binary-water classification scheme respectively.
3. The support vector machine and kernel-support vector machine classifiers performed very similarly where the decision trees and k-nearest neighbour classifiers yielded the lowest overall accuracy and kappa coefficients.
4. The kappa coefficient for the Tsai thresholding method on the 2018-2019 difference image was the highest at 0.7. The 2018-2019 time period was the most reliable and accurate time period, likely due to an increase in the precision of the digitising of the training data.
5. The VH polarization of Sentinel-1 GRD achieved an overall accuracy of 78.25% and 78.75% for Tsai and Otsu respectively, where the VV polarization achieved an overall accuracy of 74.25% and 75.00% for Tsai and Otsu respectively. The performance of VH over VV is consistent with studies done by Clement, Kilsby & Moore (2018) and Bangira et al. (2019) because of the higher sensitivity to water and non-water areas by VV.
6. Statistically, Otsu gave better results with an average overall accuracy at 78.75% and Tsai at 78.25% for the VH polarization. However, visually, the Tsai threshold is preferred because Otsu creates noise in the image thus the Tsai results are more concise.
7. The change detection approach showed the possibility that active SSM sites can be distinguished from passive SSM sites where an increase in backscatter suggested a decrease in SSM activity and a decrease in backscatter suggested an increase in SSM activity.

From the classification results, it was evident that the comparison of the different SAR sensors the C-band Sentinel-1 image outperformed the X-band KompSAT-5 image in accuracy and reliability. The KompSAT-5 image performed substandard for both classification schemes with an OA of less than 60% and the kappa coefficient of less than 0.6. Both SAR sensors could only classify the waterbodies associated with SSM. Both single-product speckle filtered SAR and multi-temporally filtered SAR produced very accurate and reliable results, however, the S1-MT database had a smaller range in the difference between the results of the multi-class classification scheme and the binary-water classification scheme. For this reason, multi-temporal filtering improves the overall reliability of the classification results. The comparison of the machine learning classification algorithms showed that RF is the best-suited algorithm to map SSM with SAR imagery, however, SVM came a close second. The influence of the custom kernel for SVM was insignificant,

therefore can be deemed as unnecessary. The DT and KNN algorithms had the poorest performance and are not suitable for SSM mapping with SAR.

From the change detection results is was evident that change detection can detect SSM with SAR because the "change" class corresponded to the SSM activities. The potential of change detection with Sentinel-1 GRD time series has exceeded expectations by not just detecting SSM but active SSM can be distinguished from passive SSM.

The research presented in this thesis aimed to assess the accuracy and reliability of applying SAR for the detection and mapping of small-scale mining in Ghana. From the results, it was shown that Sentinel-1 imagery was able to detect and map SSM especially with the change detection methodology. The classification with the object-based image analysis approach was successful in classifying water bodies associated with SSM.

5.3 EVALUATION OF RESEARCH

This section evaluates the research in the context of other studies and critically assesses both the impact as well as the limitations of the research.

5.3.1 Contextualization

The mapping of illegal mining has only been attempted by Snapir, Simms & Waine (2017) where they used multi-temporally optical imagery. They were able to detect the galamsey sites with change detection in Ghana but recommended the use of SAR imagery because of the interference of cloud cover. They were not able to distinguish between active and abandoned mines. The change detection experiment done on SAR in this study showed that Sentinel-1 imagery has a high enough resolution to also pick up the smaller strips of galamsey that stems from the main river. This study also showed that with SAR imagery active and abandoned mines can be distinguished with change detection.

Bangira et al. (2019) compared different machine learning classifiers where they mapped different types of water bodies and the SVM classifier outperformed the RF classifier with an average overall accuracy of 91.7% compared to 79.5%. Their study incorporated SAR imagery, optical imagery, as well as indices, into the training of the classifiers. The results from the classification done in this study showed that RF outperformed SVM. A likely reason that SVM performed better than RF in Bangira et al. (2019)'s study is that the indices and optical imagery gave more information on the water body types, meaning that it was simpler for the SVM classifier to classify the data. RF can over classify and this may have been the case in their study.

Bangira et al. (2019) also assessed the Otsu threshold methods and made the point that for water body mapping using thresholds is simpler and yield accurate enough results for classification. From studies where floods were mapped with SAR imagery (e.g. Long, Fatoyinbo & Policelli 2014; Mason et al. 2014; Schlaffer et al. 2015; Clement, Kilsby & Moore 2018) threshold methods were used, therefore, suggesting that mapping SSM with thresholds is a simpler and more effective option.

The SAR VH performance compared to VV performance in this study is consistent with the results of Clement, Kilsby & Moore (2018) and Bangira et al. (2019) who mapped different types of water bodies with SAR. The VH polarization gave greater contrast between water and non-water objects than the VV polarization suggesting that VV is more sensitive to variations between water and non-water features.

5.3.2 Limitations

The classification methods employed in this study were only able to classify water bodies associated with SSM. The transferability of the classification to different regions or time periods was also not tested, thus the robustness of the machine learning classification for SSM mapping was not determined. The effect of the resolution or wavelength of the SAR data to detect SSM could not be confirmed since the Sentinel-1 imagery and the KompSAT-5 imagery were of different wavelengths and different resolutions.

The segmentation was run on SAR imagery and not on the optical imagery because of the regular cloud interference in optical imagery. Ideally, segmentation should be done on optical imagery but for the purpose of examining a detection and monitoring system that can regularly detect SSM segmentation was done on the Sentinel-1 multi-temporally filtered image. The other downside is that the resolution of the Sentinel-1 imagery also had an impact on the objects and the objects may not be as accurate as with a higher resolution image. The KompSAT-5 image was not used for the segmentation because Sentinel-1 was better radiometrically corrected than KompSAT-5.

For the change detection analysis on Sentinel-1 GRD data, the data was not filtered for speckle. Also, the Sentinel-1 imagery from Google Earth Engine was not coregistered as well as the imagery should have been. This may introduce error into the difference imagery. The accuracy assessment was done by manual digitising which introduces a human error that was clearly seen as the accuracy increased from the first difference image (2016-2019) to the last difference-image analysed (2018-2019). The overall accuracy increased with each difference-image that was digitised to create the training dataset, this could be due to an increase in precision of the digitising. Other factors that may have influenced the accuracy could not be determined because of the

manual digitising process. Therefore, for future analysis, applying segmentation and selecting the objects for the accuracy assessment training database for the change detection analysis will give more consistent results in the accuracy assessment of the difference-imagery, which can then be used to identify other factors that may lead to inconsistencies in the accuracy of the image differencing results. The determination of whether a polygon was to be assigned to the class "change" or "no-change" based on a 50% coverage threshold was also done visually.

5.3.3 Contribution and Impact

The synthesised results suggest that SAR has great potential for the detection and mapping of illegal mining in tropical regions. The change detection analysis showed the potential of detecting active and abandoned mines. This type of information is very useful for governments to have reliable temporal and spatial distribution patterns of illegal mining. Multi-temporally filtered Sentinel-1 imagery provides the most accurate results and makes it possible to have a monitoring system based on freely available data to monitor illegal mining in alluvial settings. The results confirmed that high-resolution commercial data is not necessarily required.

The research in this study is also novel in the sense that the use of a reliable classifier on SAR has not been attempted yet for the application of detecting SSM affected areas (Almeida-filho & Shimabukuro 2000). The approach to detect and map SSM in this study incorporated advanced supervised machine learning classification algorithms to map the water bodies associated with SSM. The effect of multi-temporal filtering on SAR imagery for detecting SSM has not been tested before. Change detection with SAR that resulted in thematic change maps that detected SSM has not been attempted before and that the intensity of the SAR backscatter from the change maps correlates inversely with the increase in SSM activity is a new discovery.

5.4 RECOMMENDATIONS FOR FUTURE WORK

The transferability of the classification techniques was not tested and therefore this could be valuable to explore when the training datasets of one area can be used to classify an image over a different but similar area. For the change detection analysis, a recommendation is to apply segmentation on the difference-images to select objects for the accuracy assessment. Also, instead of applying a threshold method to determine "change" or "no-change" classes, machine learning classifiers such as random forest can be tested. Lastly, the intensity of the change in classes can be investigated to confirm whether small-scale mines were abandoned or active.

5.5 CONCLUDING REMARKS

The aim of the study was achieved by proving that SAR is a potentially accurate and reliable solution for the detection of small-scale mining (SSM) in tropical regions such as Ghana. The multi-temporally filtered Sentinel-1 dataset gave the highest accuracies as well as smallest ranges in values for both the multi-class and binary water classification schemes. A binary classification scheme such as the binary-water classification scheme was a better fit for the detection of the water bodies associated with SSM than the multi-class classification scheme where classes were wrongly classified. The random forest machine learning classifier is capable of classifying SSM-related waterbodies reliably with highly variable input data. When comparing the classification approach with the change detection approach for the mapping of SSM the classification was only able to map the water bodies associated with SSM where the change detection analysis detected the SSM activities. The intensity of the SSM activity was also discoverable because of the inverse correlation between the increase in backscatter and the increase in SSM activity, however, this was not further investigated in this study.

In conclusion, SAR has great potential for the mapping of illegal mining in tropical areas such as Ghana when focussing on the SSM activities surrounding rivers. The change detection analysis detected SSM where the classification methods only detected water bodies associated with SSM. Further research should be done to refine the methodology of the change detection and the potential to quantify abandoned and active mines should be further investigated.

5.6 CONTINUATION/DISSEMINATION OF THIS RESEARCH

From the findings of this Master's thesis, two journal articles are planned for submission by the end of 2020. The broad topic for each paper is the following:

1. Machine learning classification for analysing the potential of mapping illegal mining in Ghana with Synthetic Aperture Radar.
2. Analysing the potential of change detection analysis for the detection and mapping of small-scale mining in tropical regions.

REFERENCES

Alhassan IA 2014. Galamsey and the making of a deep state in Ghana: implications for national security and development. *Research on Humanities and Social Science* 4: 47–56.

Almeida-Filho R & Shimabukuro YE 2000. Detecting areas disturbed by gold mining activities through JERS-1 SAR images, Roraima State, Brazilian Amazon. *International Journal of Remote Sensing* 21: 3357–3362.

Andrew JS 2003. Potential application of mediation to land-use conflicts in small-scale mining. *Journal of Cleaner Production* 11: 117-130.

Aplin P, Atkinson PM & Curran PJ 1999. Fine spatial resolution simulated satellite sensor imagery for land cover mapping in the United Kingdom. *Remote Sensing of Environment* 68: 206–216.

Aryee BNA, Ntibery BK & Atorkui E 2003. Trends in the small-scale mining of precious minerals in Ghana: a perspective on its environmental impact. *Journal of Cleaner Production* 11: 131-140.

Asner GP, Llactayo W, Tupayachi R & Luna ER 2013. Elevated rates of gold mining in the Amazon revealed through high-resolution monitoring. *Proceedings of the National Academy of Sciences* 110: 18454–18459.

Aubynn A 2009. Sustainable solution or a marriage of inconvenience? The coexistence of large-scale mining and artisanal and small-scale mining on the Abosso Goldfields concession in Western Ghana. *Resources Policy* 34: 64–70

Baatz M & Schape A 2000. Multiresolution Segmentation: An Optimization Approach for High Quality Multi-Scale Image Segmentation. In Strobl J, Blaschke T & Griesbner G (eds) *Angewandte Geographische Informations-Verarbeitung XII*, 12-23. Beiträge zum AGIT-Symposium Salzburg. Karlsruhe.

Bala G, Caldeira K, Wickett M, Phillips T, Lobell D, Delire C & Mirin A 2007. Combined climate and carbon-cycle effects of large-scale deforestation. *Proceedings of the National Academy of Sciences* 104: 6550–6555.

Baltsavias EP 2004. Object extraction and revision by image analysis using existing geodata and knowledge: Current status and steps towards operational systems. *ISPRS Journal of Photogrammetry and Remote Sensing* 58: 129–151.

Ban Y & Wu Q 2005. RADARSAT SAR Data for Landuse/Land-Cover Classification in the Rural-Urban Fringe of the Greater Toronto Area. In *The 8th AGILE International Conference on Geographic Information Science*, 26–28. Proceedings of the 8th AGILE International Conference on Geographic Information Science. Estoril: Association of Geographic Information Laboratories in Europe.

Ban Y, Hu H & Rangel IM 2010. Fusion of Quickbird MS and RADARSAT SAR data for urban land cover mapping: object-based and knowledge-based approach. *International Journal of Remote Sensing* 31: 1391–1410.

Bangira T, Alfieri S, Menenti M, Van Niekerk A & Vekerdy Z 2017. A spectral unmixing method with ensemble estimation of endmembers: application to flood mapping in the Caprivi floodplain. *Remote Sensing* 9: 1013–1037.

Bangira T, Alfieri SM, Menenti M & Van Niekerk A 2019. Comparing thresholding with machine learning classifiers for mapping complex water. *Remote Sensing* 11: 1351–1372.

Bansah KJ, Dumakor-Dupey NK, Kansake BA, Assan E & Bekui P 2018. Socioeconomic and environmental assessment of informal artisanal and small-scale mining in Ghana. *Journal of Cleaner Production* 202: 465–475.

Bazi Y, Bruzzone L & Melgani F 2005. An Unsupervised Approach Based on the Generalized Gaussian Model to Automatic Change Detection in Multitemporal SAR images. *IEEE International Geoscience and Remote Sensing Symposium* 43: 874–887.

Belgiu M & Drăguţ L 2014. Comparing supervised and unsupervised multiresolution segmentation approaches for extracting buildings from very high-resolution imagery. *ISPRS Journal of Photogrammetry and Remote Sensing* 96: 67–75.

Belward AS & Skøien JO 2015. Who launched what, when and why; trends in global land-cover observation capacity from civilian earth observation satellites. *International Society for Photogrammetry and Remote Sensing* 103: 115–128.

Benediktsson JA & Sveinsson JR 1997. Feature extraction for multisource data classification with artificial neural networks. *International Journal of Remote Sensing* 18: 727–740.

Bishop CM 2006. *Pattern Recognition and Machine Learning*. Springer: New York.

Blaschke T 2010. Object-based image analysis for remote sensing. *ISPRS Journal of Photogrammetry and Remote Sensing* 65: 2–16.

Blaschke T, Hay GJ, Kelly M, Lang S, Hofmann P, Addink E, Feitosa RQ, van der Meer F, van der Werff H, van Coillie F & Tiede D 2014. Geographic object-based image analysis – towards a new paradigm. *International Society for Photogrammetry and Remote Sensing* 87: 180–191.

Bourgeau-Chavez LL, Kasischke ES, Brunzell SM, Mudd JP, Smith K & Frick AL 2001. Analysis of space-borne SAR data for wetland mapping in Virginia riparian ecosystems. *International Journal of Remote Sensing* 22: 3665–3687.

Breiman L 2001. Random forests. *Machine Learning* 45: 5–32.

Câmara G, Souza RCM, Freitas UM & Garrido J 1996. Spring: Integrating remote sensing and GIS by object-oriented data modeling. *Computers & Graphics* 20: 395–403.

Campbell J & Wynne R 2011. *Introduction to Remote Sensing.* 5th ed. New York: Taylor & Francis.

Campbell J 2006. *Introduction to remote sensing*. London: Taylor & Francis.

Chen KS. Huang WP, Tsay DH & Amar F 1996. Classification of multifrequency polarimetric SAR imagery using a dynamic learning neural network. *IEEE Transactions on Geoscience and Remote Sensing* 34: 814–820.

Chen PH, Lin CJ & Schölkopf B 2005. A tutorial on ν-support vector machines. *Applied Stochastic Models in Business and Industry* 21: 111–136.

Chen X, Sun Q & Hu J 2018. Generation of Complete SAR Geometric Distortion Maps Based on DEM and Neighbor Gradient Algorithm. *Applied Sciences* 8: 2206.

Chini M, Hostache R, Giustarini L & Matgen P. A hierarchical split-based approach for parametric thresholding of SAR images: Flood inundation as a test case. *IEEE Transactions on Geoscience and Remote Sensing* 55: 6975–6988.

Cihlar J, Pultz TJ & Gray AL 1992. Change detection with synthetic aperture radar. *International Journal of Remote Sensing* 13: 401–414.

Clausi DA 2002. An analysis of co-occurrence texture statistics as a function of grey level quantization. *Canadian Journal of Remote Sensing* 28: 45–62.

Clement MA, Kilsby CG & Moore P 2018. Multi-temporally synthetic aperture radar flood mapping using change detection, *Journal of Flood Risk Management*, 11: 152–168.

Clifford MJ 2017. Assessing releases of mercury from small-scale gold mining sites in Ghana. *Extractive Industries and Society* 4: 497–505.

Coltuc D, Trouvé E & Bolon Ph 2001. Bias correction and speckle reduction in Time-Space Filtering of multi-temporal SAR images. In *Scanning the Present and Resolving the Future,* 2625–2627 Proceedings IEEE 2001 International Geoscience and Remote Sensing Symposium held 9-13 July 2001. Sydney: IEEE.

Congalton RG 1991. A Review of Assessing the Accuracy of Classifications of Remotely Sensed Data. *Remote Sensing of Environment* 37: 35–46.

Congalton RG, Oderwald RG & Mead RA 1983. Assessing Landsat Classification Accuracy Using Discrete Multivariate Analysis Statistical Techniques. *Photogrammetric Engineering and Remote Sensing* 49: 1671–1678.

Conradsen K, Nielsen AA & Skriver H 2016. Determining the Points of Change in Time Series of Polarimetric SAR Data. *IEEE Transactions on Geoscience and Remote Sensing* 54: 3007–3024.

Corbett T, O'Faircheallaigh C & Regan A 2017. "Designated areas" and the regulation of artisanal and small-scale mining. *Land Use Policy* 68: 393–401.

Cortes C & Vapnik V 1995. Support-Vector Networks. *Machine Learning* 20: 273–297.

Crawford G, Agyeyomah C, Botchwey G & Mba A 2015. The impact of Chinese involvement in small-scale gold mining in Ghana [online]. International Growth Centre. Available from https://www.theigc.org/wp-content/uploads/2016/08/Crawford-et-al-2015-Final-Report-1.pdf [Accessed 25 April 2018].

Crowson M, Hagensieker R & Waske B 2019. Mapping land cover change in northern Brazil with limited training data. *International Journal of Applied Earth Observation and Geoinformation* 78: 202–214.

Cui B, Zhang Y, Yan L & Cai X 2017. A SAR Intensity Images Change Detection Method Based on Fusion Difference Detector and Statistical Properties. In Li D, Gong J, Yang B, Wu H, Lindenbergh R, Boehm J, Rutzinger M, Yao W, Weinmann M, Zhang Y, Hänsch R, Shahbazi M, Haala N, Rothermel M, Wu L, Gui Z, Cheng X, Wu H, Li S, Kang Z, Khoshelham K, Peter M, Díaz-Vilariño L, Balz T, Osmanoglu B, Rocca F, Sörgel U & Heipke C (eds) *ISPRS Geospatial Week*, 439-443. ISPRS Annals of the Photogrammetry, Remote Sensing and Spatial Information Sciences held 18–22 September 2017. Wuhan: International Society for Photogrammetry and Remote Sensing.

Daily Graphic 2018. Special Report: The Cost of Galamsey – Ghana Extractive Industries Transparency Initiative [online]. Available from http://www.gheiti.gov.gh/site/index.php?option=com_content&view=article&id=187:special-report-the-cost-of-galamsey&catid=1:latest-news&Itemid=29 [Accessed 17 March 2018].

DataCamp 2019. Support Vector Machines in Scikit-learn [online]. Available from https://www.datacamp.com/community/tutorials/svm-classification-scikit-learn-python [Accessed 12 June 2019].

Du Y, Zhang Y, Ling F, Wang Q, Li W & Li X 2016. Water bodies' mapping from Sentinel-2 imagery with modified normalized difference water index at 10-m spatial resolution produced by sharpening the SWIR band. *Remote Sensing* 8: 354–373.

Dutra LV, Hernandez FP, Mazzocato ME, Souza RCM & Oliveira C 1999. Land cover classification based on multi-date JERS-1 imagery as a basis for deforestation detection. In Stein TI (eds) *Remote Sensing of the System Earth - a challenge for the 21st century*, 2759–2761. Proceedings of the International Geoscience and Remote Sensing Symposium held 28 June-2 July 1999. Hamburg: IEEE.

Elmes A, Ipanaqué JGY, Rogan J, Cuba N & Bebbington A 2014. Mapping licit and illicit mining activity in the Madre de Dios region of Peru. *Remote Sensing Letters* 5: 882–891.

El-Zaart A 2015. Synthetic Aperture Radar Images Segmentation Using Minimum Crossentropy with Gamma Distribution. *Signal & Image Processing : An International Journal* 6: 19–31.

Emmanuel A 2013. Impact of Illegal Mining on Water Resources for Domestic and Irrigation Purposes. *ARPN Journal of Earth Sciences* 2: 117–121.

Emmanuel O 2013. 'GALAMSEY' A Canker In Western Region [online]. Available from https://www.modernghana.com/news/472110/1/galamsey-a-canker-in-western-region.html [Accessed 16 March 2018].

ENVI 1994. *Environment for visualising images 5.5.* Harris Geospatial Solutions Inc. [Online Help]. Online available from https://www.harrisgeospatial.com [Accessed 30 October 2019].

ESA 2019. Interferometric Wide swath SLC - Sentinel-1 SAR Technical Guide - Sentinel Online [online]. Available from https://sentinel.esa.int/web/sentinel/technical-guides/sentinel-1-

sar/products-algorithms/level-1/single-look-complex/interferometric-wide-swath [Accessed 24 June 2019].

ESA Earth Online 2019. Radar Course 2 - Parameters affecting radar backscatter. ERS Radar Courses - ESA Operational EO Missions - Earth Online - ESA [online]. Available from https://earth.esa.int/web/guest/missions/esa-operational-eo-missions/ers/instruments/sar/applications/radar-courses/content-2/-/asset_publisher/qIBc6NYRXfnG/content/radar-course-2-parameters-affecting-radar-backscatter [Accessed 15 July 2019].

ESA Earthnet Online 2019. Scientific Background [online]. Available from https://earth.esa.int/handbooks/asar/CNTR1-1-2.html [Accessed 15 July 2019].

Ferring D, Hausermann H & Effah E 2016. Site-specific: Heterogeneity of small-scale gold mining in Ghana. *Extractive Industries and Society* 3: 171–184.

Flores A, Herndon K, Thapa RB & Cherrington AE 2019. *The SAR Handbook: Comprehensive Methodologies for Forest Monitoring and Biomass Estimation*. Huntsville: NASA

Foody GM 2020. Explaining the unsuitability of the kappa coefficient in the assessment and comparison of the accuracy of thematic maps obtained by image classification. *Remote Sensing of Environment* 239: 111630.

Forkuor G, Ullmann T & Griesbeck M 2020. Mapping and monitoring small-scale mining activities in Ghana using Sentinel-1 time series (2015-2019). *Remote Sensing* 12: 911.

Fu B, Wang Y, Campbell A, Li Y, Zhang B, Yin S, Xing Z & Jin X 2017. Comparison of object-based and pixel-based Random Forest algorithm for wetland vegetation mapping using high spatial resolution GF-1 and SAR data. *Ecological Indicators* 73: 105–117.

Fukunaga K 1990. *Introduction to statistical pattern recognition*. 2nd ed. San Diego: Academic Press.

Garzelli A & Zoppetti C 2017. Optimizing SAR change detection based on log-ratio features. In *9th International Workshop on the Analysis of Multitemporal Remote Sensing Images*, 1-4. MultiTemp workshop held 27-29 June 2017. Bruges: IEEE.

Gbireh A, Cobblah A & Suglo R 2007. Analysis of the Trends of Gold Mining in Ghana. *Ghana Mining Journal* 9: 38–49.

GhanaLegal 2018. Small-scale Gold Mining Law – 1989 (PNDCL 218) [online]. Available from http://laws.ghanalegal.com/acts/id/556/small-scale-gold-mining-law [Accessed 01 May 2018].

GhanaWeb 2016. Residents worried over abandoned galamsey pits [online]. Available from https://www.ghanaweb.com/GhanaHomePage/regional/Residents-worried-over-abandoned-galamsey-pits-467469 [Accessed 16 March 2018].

GhanaWeb 2018. Ghana: Geography, Location, weather etc. [online]. Available from https://www.ghanaweb.com/GhanaHomePage/geography/climate.php [Accessed 25 March 2018].

GhanaWeb 2019. Ghana: Geography, Location, weather etc. 2019. Ghana: Geography, Location, weather etc. [online]. Available from https://www.ghanaweb.com/GhanaHomePage/geography/climate.php [Accessed 15 July 2019].

Gilbertson JK & Van Niekerk A 2017. Value of dimensionality reduction for crop differentiation with multi-temporal imagery and machine learning. *Computers and Electronics in Agriculture* 142: 50–58.

Gilbertson JK, Kemp J & Van Niekerk A 2017. Effect of pan-sharpening multi-temporally Landsat 8 imagery for crop type differentiation using different classification techniques. *Computers and Electronics in Agriculture* 134: 151–159.

Giustarini L, Hostache R, Matgen P, Schumann GJ-P, Bates PD & Mason DC 2013. A Change detection approach to flood mapping in urban areas using TerraSAR-X. *IEEE Transgressions on Geoscience and Remote Sensing* 51: 2417–2430.

Gong M, Zhao J, Liu J, Miao Q & Jiao L 2016. Aperture Radar Images Based on Deep Neural Networks. *IEEE Transactions on Neural Networks and Learning Systems* 27: 125–138.

Gong M, Zhou Z & Ma J 2012. Change detection in synthetic aperture radar images based on image fusion and fuzzy clustering. IEEE Transactions on Image Processing 21: 2141–2151.

Google Earth Pro 2018. *Google Earth Pro 7.3.1.4507 (64-bit)* Google Inc.

Gorelick N, Hancher M, Dixon M, Ilyushchenko S, Thau D & Moore R 2017. Google Earth Engine: Planetary-scale geospatial analysis for everyone. *Remote Sensing of Environment*

Gyamfi E, Appiah-Adjei EK & Adjei KA 2019. Potential heavy metal pollution of soil and water resources from artisanal mining in Kokoteasua, Ghana. *Groundwater for Sustainable Development* 8: 450–456.

Gyamfi O, Sorenson PB, Darko G, Ansah E & Bak JL 2020. Human health risk assessment of exposure to indoor mercury vapour in a Ghanaian artisanal small-scale gold mining community. *Chemosphere* 241: 125014.

Haboudane D & Bahri EM 2007. Deforestation detection and monitoring in cedar forests of the Moroccan Middle-Atlas mountains. In *Sensing and Understanding Our Planet*, 4327–4330. Proceedings of the International Geoscience and Remote Sensing Symposium held 23-27 July 2007. Barcelona: IEEE.

Hall-Beyer M 2017. Practical guidelines for choosing GLCM textures to use in landscape classification tasks over a range of moderate spatial scales. *International Journal of Remote Sensing* 38: 1312–1338.

Han H, Hong SH, Kim HC, Chae TB & Choi HJ 2017. A study of the feasibility of using KOMPSAT-5 SAR data to map sea ice in the Chukchi Sea in late summer. *Remote Sensing Letters* 8: 468–477.

Hanley JA & McNeil BJ 1982. The Meaning and Use of the Area under a Receiver Operating Characteristic (ROC) Curve. *Radiology* 143: 29–36.

Hansen M, Potapov P, Moore R, Hancher M, Turubanova SA, Tyukavina A, Thau D, Stehman S V, Goetz SJ, Loveland TR, Kommareddy A, Egorov A, Chini L, Justice CO & Townshed JRG 2013. High-resolution global maps of 21st-century forest cover change. *Science* 342: 850-853.

Haralick RM 1979. Statistical and Structural Approaches to Texture. *Proceedings of the IEEE* 67: 786–804.

Haralick RM, Shanmugam K & Dinstein I 1973. Textural Features for Image Classification. *IEEE Transactions on Systems, Man and Cybernetics* 3: 610–621.

Hay GJ & Castilla G 2008. Geographic Object-Based Image Analysis (GEOBIA): A new name for a new discipline. In Blaschke T, Lang S & Hay G (eds) *Object Based Image Analysis*, 93–112. Berlin: Springer.

Hay GJ, Niemann KO & McLean GF 1996. An object-specific image-texture analysis of high-resolution forest imagery. *Remote Sensing of Environment* 55: 108–122.

Hentschel T, Hruschka F & Priester M 2002. Global Report on Artisanal and Small Scale Mining [online]. https://pubs.iied.org/pdfs/G00723.pdf [Accessed 20 April 2018].

Hess LL, Melack JM, Novo EMLM, Barbosa CCF & Gastil M 2003. Dual-season mapping of wetland inundation and vegetation for the central Amazon basin. *Remote Sensing of Environment* 87: 404–428.

Hilson G 2001. A contextual review of the Ghanaian small-scale mining industry. *Mining, Minerals and Sustainable Development* 76: 29.

Hilson G 2016. Farming, small-scale mining and rural livelihoods in Sub-Saharan Africa: A critical overview. *Extractive Industries and Society* 3: 547–563.

Hilson G, Goumandakoye H & Diallo P 2019. Formalizing artisanal mining "spaces" in rural sub-Saharan Africa: The case of Niger. *Land Use Policy* 80: 259–268.

Hilson G, Hilson A, Maconashie R, McQuilken J & Goumandakoye H 2017. Artisanal and small-scale mining (ASM) in sub-Saharan Africa: Re-conceptualizing formalization and "illegal" activity. *Geoforum* 83: 80–90.

Hirose K, Maruyama Y, Do Van Q, Tsukada M & Shiokawa Y 2001. Visualization of flood monitoring in the lower reaches of the Mekong River. In *22nd Asian Conference on Remote Sensing*, 9-15. Proceedings of the 22nd Asian Conference on Remote Sensing 5-9 November 2001. Singapore: Centre for Remote Imaging, Sensing and Processing.

Hoekman DH & Quiñones MJ 2000. Land cover type and biomass classification using AirSAR data for evaluation of monitoring scenarios in the Colombian Amazon. *IEEE Transactions on Geoscience and Remote Sensing* 38: 685–696

Hsu CW, Chang CC & Lin CJ 2003. A Practical Guide to Support Vector Classification [online]. Available from https://www.csie.ntu.edu.tw/~cjlin/papers/guide/guide.pdf [Accessed 12 June 2019].

Hu J, Ghamisi P & Zhu X 2018. Feature Extraction and Selection of Sentinel-1 Dual-Pol Data for Global-Scale Local Climate Zone Classification. *ISPRS International Journal of Geo-Information* 7: 379–399.

Hwang JI & Jung HS 2018. Automatic Ship Detection Using the Artificial Neural Network and Support Vector Machine from X-Band SAR Satellite Images. *Remote Sensing* 10: 1799–1821.

Ibrahim A 2018. Restore rivers to original path before rains set in - Anti-galamsey NGO [online]. Available from https://www.myjoyonline.com/news/2018/February-15th/restore-rivers-to-original-path-before-rains-set-in-anti-galamsey-ngo.php [Accessed 30 March 2018].

Jain AK, Duin RPW & Mao J 2000. Statistical pattern recognition: a review. *IEEE Transactions on Pattern Analysis and Machine Intelligence* 22: 4–37.

Jin H, Mountrakis G & Stehman SV 2014. Assessing integration of intensity, polarimetric scattering, interferometric coherence and spatial texture metrics in PALSAR-derived land cover classification. *ISPRS Journal of Photogrammetry and Remote Sensing* 98: 70–84.

Joshi N, Baumann M, Ehammer A, Fensholt R, Grogan K, Hostert P, Jepsen MR, Kuemmerle T, Meyfroidt P, Mitchard ETA, Reiche J, Ryan CM & Waske B 2016. A review of the application of optical and radar remote sensing data fusion to land use mapping and monitoring. *Remote Sensing* 8:1-23.

Kettig R & Landgrebe D 1976. Classification of multispectral image data by extraction and classification of homogeneous objects. *IEEE Transactions on Geoscience Electronics* GE-14: 19–26.

Knoblauch AM, Farnham A, Ouoba J, Zanetti J, Müller S, Jean-Richard V, Utzinger J, Wehrli B, Brugger F, Diagbouga S & Winkler MS 2020. Potential health effects of cyanide use in artisanal and small-scale gold mining in Burkina Faso. *Journal of Cleaner Production* 252: 119689.

Kranz O, Lang S & Schoepfer E 2017. 2.5D change detection from satellite imagery to monitor small-scale mining activities in the Democratic Republic of the Congo. *International Journal of Applied Earth Observation and Geoinformation* 61: 81–91.

Kusimi JM 2008. Assessing land use and land cover change in the Wassa West District of Ghana using remote sensing. *GeoJournal* 71: 249–259.

Lambin E, Turner B, Geist H, Agbola S, Angelsen A, Bruce J, Coomes O, Dirzo R, Fischer G & Folke C 2001. The causes of land-use and land-cover change: moving beyond the myths. *Global Environmental Change* 11: 261–269.

Lang MW, Townsend PA & Kasischke ES 2008. Influence of incidence angle on detecting flooded forests using C-HH synthetic aperture radar data. *Remote Sensing of Environment* 112: 3898–3907.

Lang S 2008. Object-based image analysis for remote sensing applications: Modeling reality - Dealing with complexity. In Blaschke T, Lang S & Hay GJ (eds) *Object Based Image Analysis*, 1–25. Heidelberg: Springer.

Lê TT, Atto AM & Trouve E 2015. Change analysis using multitemporal Sentinel-1 SAR images.

Lee JS, Jurkevich I, Dewaele P, Wambacoq P & Oosterlink A 1994. Speckle filtering of synthetic aperture radar images: a review, *Remote Sensing Reviews* 8: 313–340.

Levine MD & Nazif AM 1985. Rule-based image segmentation: A dynamic control strategy approach. *Computer Vision, Graphics and Image Processing* 32: 104–126.

Lillesand T, Chipman J & Kiefer R 2008. *Remote sensing and image interpretation*. 6th ed. New York: John Wiley & Sons.

Lobo A, Chick O & Casterad A 1996. Classification of Mediterranean crops with multisensor data: Per-pixel versus per-object statistics and image segmentation. *International Journal of Remote Sensing* 17: 2385–2400.

Long F, Zhang H & Feng DD 2003. Fundamentals of content-based image retrieval. In Feng DD, Siu WC, Zhang HJ (eds) *Multimedia Information Retrieval and Management*, 1–26. Berlin: Springer.

Long S, Fatoyinbo TE & Policelli F 2014. Flood extent mapping for Namibia using change detection and thresholding with SAR. *Environmental Research Letters* 9: 035002.

Longepe N, Rakwatin P, Isoguchi O, Shimada M, Uryu Y & Yulianto K 2011. Assessment of ALOS PALSAR 50 m Orthorectified FBD Data for Regional Land Cover Classification by Support Vector Machines. *IEEE Transactions on Geoscience and Remote Sensing* 49: 2135–2150.

Lopes A, Nezry E, Touzi R & Laur H 1993. Structure detection and statistical adaptive speckle filtering in SAR images. *International Journal of Remote Sensing* 14: 1735–1758.

Lu J, Giustarini L, Xiong B, Zhao L, Jiang Y & Kuang G 2014. Automated flood detection with improved robustness and efficiency using multi-temporally SAR data. *Remote Sensing Letters* 5: 240–248.

Lynch J, Maslin M, Balzter H & Sweeting M 2013. Choose satellites to monitor deforestation. *Nature* 496: 293–294.

Ma L, Li M, Ma X, Cheng L, Du P & Liu Y 2017. A review of supervised object-based land-cover image classification. *ISPRS Journal of Photogrammetry and Remote Sensing* 130: 277–293.

Mahdianpari M, Salehi B, Mohammadimanesh F & Motagh M 2017. Random forest wetland classification using ALOS-2 L-band, RADARSAT-2 C-band, and TerraSAR-X imagery. *ISPRS Journal of Photogrammetry and Remote Sensing* 130: 13–31.

Malenovský Z, Rott H, Cihlar J, Schaepman ME, García-Santos G, Fernandes R & Berger M 2012. Sentinels for Science: Potential of Sentinel-1, -2, and -3 missions for scientific observations of ocean, cryosphere, and land, *Remote Sensing of Environment* 120:91–101.

Manavalan R 2017. SAR image analysis techniques for flood area mapping-literature survey. *Earth Science Informatics* 10: 1–14.

Mansourpour M, Rajabi MA & Blais JAR 2006. Effects and Performance of Speckle Noise Reduction Filters on Active Radar and SAR Images [online]. Available from http://people.ucalgary.ca/~blais/Mansourpour2006.pdf [Accessed 25 June 2018].

Mantey J, Owusu- Nimo F, Nyarko KB & Aubynn A 2017. Operational dynamics of "Galamsey" within eleven selected districts of western region of Ghana. *Journal of Mining and Environment* 8: 11–34.

Maowei J, Xiaojing L, Shunchuan W, Yongtao G & Linlin G 2011. Use of SAR interferometry for monitoring illegal mining activities: A case study at Xishimen Iron Ore Mine. *Mining Science and Technology* 21: 781–786.

Martinis S & Rieke C 2015. Backscatter analysis using multi-temporally and multi-frequency SAR data in the context of flood mapping at River Saale, Germany. *Remote Sensing* 7: 7732–7752.

Martinis S, Twele A & Voigt S 2009. Towards operational near real-time flood detection using a split-based automatic thresholding procedure on high-resolution TerraSAR-X data. Natural Hazards and Earth System Science 9: 303–314.

Martinis S, Twele A & Voigt S 2009. Towards operational near real-time flood detection using a split-based automatic thresholding procedure on high-resolution TerraSAR-X data. *Natural Hazards and Earth System Sciences* 9: 303–314.

Mas J, Velázquez A, Díaz-Gallegos J, Mayorga-Saucedo R, Alcántara C, Bocco G, Castro R, Fernández T & Pérez-Vega A 2004. Assessing land use/cover changes: a nationwide multidate spatial database for Mexico. *International Journal of Applied Earth Observation and Geoinformation* 5: 249–261.

Mason DC, Guistarini L, Garcia-Pintado J & Cloke HL 2014. Detection of flooded urban areas in high-resolution Synthetic Aperture Radar images using double scattering. *International Journal of Applied Earth Observation and Geoinformation* 28: 150–159.

Matgen P, Hostache R, Schumann G J-P, Pfister L, Hoffmann L & Savenije H 2011. Towards an automated SAR-based flood monitoring system: lessons learned from two case studies. *Physics and Chemistry of the Earth Parts A/B/C* 36: 241–252.

Mather P & Koch M 2011. *Computer Processing of Remotely-Sensed Images*. 4th ed. Chichester: John Wiley & Sons, Ltd.

McKeown DM, Harvey WA & Wixson LE 1989. Automating knowledge acquisition for aerial image interpretation. *Computer Vision, Graphics, and Image Processing* 46: 37–81.

Mcquilken J & Hilson G 2016. Sustainable markets Artisanal and small-scale gold mining in Ghana Evidence to inform an 'action dialogue' [online]. Available from http://pubs.iied.org/pdfs/16618IIED.pdf.

Micklethwaite K 2016. Violence and illegal mining tarnish gold supply chains [online]. Available from https://maplecroft.com/portfolio/new-analysis/2016/09/15/latin-america-violence-and-illegal-mining-tarnish-gold-supply-chains/ [Accessed 25 April 2018].

Moody KH, Hasan KM, Aljic S, Blakeman VM, Hicks LP, Loving DC, Moore ME, Hammett BS, Silva-González Mó, Seney CS, Kiefer AM 2019. Mercury emissions from Peruvian gold shops: Potential ramifications for Minamata compliance in artisanal and small-scale gold mining communities. *Environmental Research* 182: 109042.

Muro J, Canty M, Conradsen K, Hüttich C, Nielsen AA, Skriver H, Remy F, Strauch A, Thonfeld F & Menz G 2016. Short-term change detection in wetlands using Sentinel-1 time series. *Remote Sensing* 8: 795-809.

Myburgh G & Van Niekerk A 2013. Effect of Feature Dimensionality on Object-based Land Cover Classification : A Comparison of Three Classifiers. *South African Journal of Geomatics* 2: 13–27.

Myburgh G & Van Niekerk A 2014. Impact of training set size on object-based landcover classification: A comparison of three classifiers, *International Journal of Applied Geospatial Research* 5: 49–67.

Obeng EA, Oduro KA, Obiri BD, Abukari H, Guuroh RT, Djagbletey GD, Appiah-Korang J & Appiah M 2019. Impact of illegal mining activities on forest ecosystem services: local communities' attitudes and willingness to participate in restoration activities in Ghana. *Heliyon* 5: e02617.

Oberthür T, Hirdes W, Höhndorf A, Schmidt Mumm A, Vetter U, Weiser T, Davis DW, Blenkinsop TG, Amanor JA & Loh G 1995. A review of gold mineralisation in the Ashanti

Belt of Ghana and its relation to the crustal evolution of the terrane. *Communications of the Geological Survey of Namibia* 10: 121- 127.

Oberthür T, Weiser T, Amanor JA & Chryssoulis SL 1997. Mineralogical siting and distribution of gold in quartz veins and sulfide ores of the Ashanti mine and other deposits in the Ashanti belt of Ghana: Genetic implications. *Mineralium Deposita* 32: 2–15.

Otamonga JP & Poté JW 2020. Abandoned mines and artisanal and small-scale mining in Democratic Republic of the Congo (DRC): Survey and agenda for future research. *Journal of Geochemical Exploration* 208: 106394.

Otsu N 1979. A threshold selection method from gray-level histograms. *IEEE Transactions on Systems, Man, and Cybernetics* 9: 62–66.

Owusu EE & Dwomoh G 2012. The Impact of Illegal Mining on the Ghanaian Youth: Evidence From Kwaebibirem District In Ghana. *Research on Humanities and Social Sciences* 2: 86–93.

Owusu-Koranteng D & Owusu-Koranteng H 2017. The menace of mining and water pollution [online]. Available from https://www.ghanaweb.com/GhanaHomePage/NewsArchive/The-menace-of-mining-and-water-pollution-526482 [Accessed 07 April 2018].

Owusu-Nimo F, Mantey J, Nyarko KB, Appiah-Effah E & Aubynn A 2018. Spatial distribution patterns of illegal artisanal small scale gold mining (Galamsey) operations in Ghana: A focus on the Western Region. *Heliyon* 4: 1-36.

Pal R & Pal K 1993. A review on image segmentation techniques. *Pattern Recognition* 26: 1277–1294.

Parihar N, Das A, Rathore VS, Nathawat MS & Mohan S 2014. Analysis of L-band SAR backscatter and coherence for delineation of land-use/land-cover. *International Journal of Remote Sensing* 35: 6781–6798.

Pedersena RH, Mutagwabab W, Jønssonc JB, Schoneveldd G, Jacobe T, Chachag M, Wengh X & Njau MG 2019. Mining-sector dynamics in an era of resurgent resource nationalism: Changing relations between large-scale mining and artisanal and small-scale mining in Tanzania. *Resources Policy* 62: 339–346.

Pedregosa F, Varoquaux G, Gramfort A, Michel V & Thirion B 2011. Scikit-learn: Machine Learning in Python. *Journal of Machine Learning Research* 12: 2825–2830.

Peres CA 2001. Synergistic effects of subsistence hunting and habitat fragmentation on Amazonian forest vertebrates. *Conservation Biology* 15: 1490–1505.

Pierce LE, Dobson MC & Ulaby F 1994. Knowledge-based land-cover classification using ERS-l / JERS-1 composites. In *Surface and Atmospheric Remote Sensing: Technologies, Data Analysis and Interpretation*, 1599–1601. Proceedings of the International Geoscience and Remote Sensing Symposium held 8-12 August 1994. Pasadena: IEEE.

Principe JC, Kim M & Fisher JW 1998. Target discrimination in synthetic aperture radar using artificial neural networks. *IEEE Transactions on Image Processing* 7: 1136–1149.

Quegan S, Toan, T L, Yu J J, Ribbes F & Floury N 2000. Multitemporal ERS SAR analysis applied to forest mapping. *IEEE Transactions on Geoscience and Remote Sensing* 38: 741-753.

Radke RJ, Andra S, Al-Kofahi O & Roysam B 2005. Image change detection algorithms: A systematic survey. IEEE Transactions on Image Processing 14: 294–307.

Rana VK &Suryanarayana TMV 2019. Evaluation of SAR speckle filter technique for inundation mapping. *Remote Sensing Applications: Society and Environment* 16: 100271.

Reiche J, de Bruin S, Hoekman D, Verbesselt J & Herold M 2015. A Bayesian approach to combine Landsat and ALOS PALSAR time series for near real-time deforestation detection. *Remote Sensing* 7: 4973–4996.

Reiche J, Hamunyela E, Verbesselt J, Hoekman D &Wageningen MH 2018. Improving near-real-time deforestation monitoring in tropical dry forests by combining dense Sentinel-1 time series with Landsat and ALOS-2 PALSAR-2. *Remote Sensing of Environment* 204: 147–161.

Ribbes F, Toan TL, Bruniquel J, Floury N, Stussi N, Liew SC & Wasrin UR 1997. Deforestation monitoring in tropical regions using multitemporal ERS/JERS SAR and InSAR data. In *Remote Sensing - A Scientific Vision for Sustainable Development*, 1560–1562. Proceedings of the International Geoscience and Remote Sensing Symposium held 3-8 August 1997. Singapore: IEEE.

Richards JA, Woodgate PW & Skidmore AK 1987. An explanation of enhanced radar backscattering from flooded forests. *International Journal of Remote Sensing* 8: 1093–1100.

Rodriguez-Galiano VF, Ghimire B, Rogan J, Chica-Olmo M & Rigol-Sanchez JP 2012. An assessment of the effectiveness of a random forest classifier for land-cover classification. *ISPRS Journal of Photogrammetry and Remote Sensing* 67: 93–104.

Ryherd S & Woodcock CE 1996. Combining spectral and texture data in the segmentation of remotely sensed images. *Photogrammetric Engineering & Remote Sensing* 62: 181–194.

Saatchi SS, Soares JV & Alves DS 1997. Mapping deforestation and land use in Amazon rainforest by using SIR-C imagery. *Remote Sensing of Environment* 59: 191–202.

Santoro M & Wegmüller U 2012. *Multi-temporally SAR metrics applied to map water bodies*. In *Remote Sensing for a Dynamic Earth*, 5230–5233. Proceedings of the International Geoscience and Remote Sensing Symposium held 22-27 July 2012. Munich: IEEE.

Schiewe J 2002. Segmentation of high-resolution remotely sensed data - concepts, applications and problems. In Armenakis C & Lee YC (eds) *Geospatial Theory, Processing and Applications*, 1-6. Proceedings of Joint ISPRS Commission IV Symposium held 9–12 July 2002. Ottawa: ISPRS.

Schlaffer S, Chini M, Giustarini L, Matgen P 2017. Probabilistic mapping of flood-induced backscatter changes in SAR time series. *International Journal of Applied Earth Observation and Geoinformation* 56: 77–87.

Schlaffer S, Matgen P, Hollaus M & Wagner W 2015. Flood detection from multi-temporally SAR data using harmonic analysis and change detection. *International Journal of Applied Earth Observation and Geoinformation* 38: 15–24.

Scikit-learn developers 2012. User Guide for Scikit Learn version 0.12. Scikit Learn User Guide 0.12 [online]. Accessed from https://www.scribd.com/document/205251894/Scikit-Learn-User-Guide-0-12 [Accessed 12 June 2019].

Sephton AJ, Brown LMJ, Macklin JT, Partington KC, Veck NJ & Rees WG 1994. Segmentation of Synthetic-Aperture Radar imagery of sea ice. *International Journal of Remote Sensing* 15: 803-825.

Serfor-Armah Y, Nyarko BJB, Adotey DK, Adomako D & Akaho EHK 2004. The impact of small-scale mining activities on the levels of mercury in the environment: The case of Prestea and its environs. *Journal of Radioanalytical and Nuclear Chemistry* 262: 685–690.

Shen X, Anagnostoua EN, Allenc GH, Brakenridged GR & Kettnerd AJ 2019. Near-real-time non-obstructed flood inundation mapping using synthetic aperture radar. *Remote Sensing of Environment* 221: 302–315.

Shimabukuro YE, Amaral S, Ahern FJ & Pietsch RW 1998. Land cover classification from RADARSAT data of the Tapajós National Forest, Brazil. *Canadian Journal of Remote Sensing* 24: 393–401.

SI-Imaging Services Co., Ltd. 2019. Products – SIIS [online]. Available from http://www.si-imaging.com/products/#1478507064219-34e51d03-67d9 [Accessed 24 June 2019].

Singh A 1989. Digital change detection techniques using remotely sensed data. *International Journal of Remote Sensing* 10: 989–1003.

Smith AJB, Henry G & Frost-Killian S 2016. A Review of the Birimian Supergroup- and Tarkwaian Group-Hosted Gold Deposits of Ghana. *Episodes* 39: 177–197.

SNAP 2017. *Sentinel Application Platform, Sentinel-1 Toolbox 6.0.0.* Array Systems Computing Inc. and contributors.

Snapir B, Simms DM & Waine TW 2017. Mapping the expansion of galamsey gold mines in the cocoa growing area of Ghana using optical remote sensing. *International Journal of Applied Earth Observation and Geoinformation* 58: 225–233.

Srinivasan GN & Shobha G 2008. Statistical Texture Analysis. *World Academy of Science Engineering, and Technology* 36: 1264–1269.

Statistics How To 2019. Z-table (Right of Curve or Left) - Statistics How To [online]. Available from https://www.statisticshowto.datasciencecentral.com/tables/z-table/ [Accessed 27 June 2019].

Story M & Congalton R 1986. Accuracy assessment: a user's perspective. *Photogrammetric Engineering & Remote Sensing* 43: 1135–1137.

Strahler A, Woodcock C & Smith J 1986. On the nature of models in remote sensing. *Remote Sensing of Environment* 20: 121–139.

Tan Q, Bi S, Hu J & Liu Z 2004. *Measuring lake water level using multi-source remote sensing images combined with hydrological statistical data*. In *Science for Society: Exploring and Managing a Changing Planet*, 4885–4888. Proceedings of the International Geoscience and Remote Sensing Symposium. Anchorage: IEEE.

Teschner BA 2012. Small-scale mining in Ghana: The government and the galamsey, *Resources Policy*, 37: 308–314.

Today Newspaper 2016. Galamsey killing Oda Forest Reserve but gov't looks unconcerned [online]. Available from https://www.todaygh.com/galamsey-killing-oda-forest-reserve-govt-looks-unconcerned/ [Accessed 16 March 2018].

Tsai WH 1985. Moment-preserving thresholding: a new approach, *Computer Vision, Graphics, & Image Processing*, 29: 377–393.

Turner B, Lambin E & Reenberg A 2007. The emergence of land change science for global environmental change and sustainability. *Proceedings of the National Academy of Sciences* 104: 20666–20671.

Valarmathi R & Suganya N 2015. An Efficient Approach for Change Detection in SAR Images. Middle-East Journal of Scientific Research Signal Processing and Security 23: 280–285.

Veiga MM, Maxson PA & Hylander LD 2006. Origin and consumption of mercury in small-scale gold mining. *Journal of Cleaner Production* 14: 436–447.

Verhulp J & Van Niekerk A 2017. Transferability of decision trees for land cover classification in a heterogeneous area. South African Journal of Geomatics 6: 30–46.

Vogel C, Musamba J & Radley B 2018. A miner's canary in eastern Congo: Formalisation of artisanal 3T mining and precarious livelihoods in South Kivu. *Extractive Industries and Society* 5: 73–80.

Walker WS, Stickler CM, Kellndorfer JM, Kirsch KM & Nepstad DC 2010. Large-area classification and mapping of forest and land cover in the Brazilian Amazon: a comparative analysis of ALOS/PALSAR and Landsat data sources. *IEEE Journal of Selected Topics in Applied Earth Observations and Remote Sensing* 3: 594–604.

Wang Y & Imhoff ML 1993. Simulated and observed LHH radar backscatter from tropical mangrove forests. *International Journal of Remote Sensing* 14: 2819–2828.

Wang Y, Hess LL, Filoso S & Melack JM 1995. Understanding the radar backscattering from flooded and non-flooded Amazonian forests: Results from canopy backscatter modelling. *Remote Sensing of Environment* 54: 324–332.

Waske B & Van der Linden 2008. Classifying multilevel imagery from SAR and optical sensors by decision fusion. IEEE Transactions on Geoscience and Remote Sensing 46: 1457–1466.

Weather Spark 2018. Average Weather in Accra, Ghana, Year-Round [online]. Available from https://weatherspark.com/y/42322/Average-Weather-in-Accra-Ghana-Year-Round [Accessed 11 April 2018].

Woodhouse IH 2005. *Introduction to Microwave Remote Sensing*. Boca Raton: CRC Press.

World Weather & Climate Information. 2019. Climate and average weather in Ghana [online]. Available from https://weather-and-climate.com/average-monthly-Rainfall-Temperature-Sunshine-in-Ghana [Accessed 22 December 2019].

Wulder M 1998. Optical remote-sensing techniques for the assessment of forest inventory and biophysical parameters. *Progress in Physical Geography* 22: 449–476.

Xu H, Tian Z & Ding M 2008. Segmentation of synthetic aperture radar image using multiscale information measure-based spectral clustering. *Chinese Optics Letters* 6: 248-250.

Yamada Y 2001. Detection of flood-inundated area and relation between the area and micro-geomorphology using SAR and GIS. In *Scanning the Present and Resolving the Future*, 3282–3284. Proceedings of the International Geoscience and Remote Sensing Symposium. Sydney: IEEE.

Yankson PWK & Gough KV 2019. Gold in Ghana: The effects of changes in large-scale mining on artisanal and small-scale mining (ASM). *Extractive Industries and Society* 6: 120–128.

Yard EE, Horton J, Schier JG, Caldwell K, Sanchez C, Lewis L & Gastaňaga C 2012. Mercury Exposure among Artisanal Gold Miners in Madre de Dios, Peru: A Cross-Sectional Study. *Journal of Medical Toxicology* 8: 441–448.

Zhang Y & Ju Y 2011. Unsupervised Multiresolution Segmentation of SAR Imagery Based on Region-Based Hierarchical Model. In Deng H, Miao D, Lei J & Wang FL (eds) *Artificial Intelligence and Computational Intelligence*. Berlin: Springer.

Zhu L, Zhang P, Li D, Zhu X & Wang C 2015. A novel change detection method based on high-resolution SAR images for river course. *Optik* 126: 3659–3668.

APPENDIX A

Supplementary material for Chapter 3 (Confusion matrices for Experiments 1 and 2).

Table A1 Random forest multi-class classification on S1 confusion matrix.

	Water	Vegetation	Bare ground	Built-up	TOTALS	PA %	EO %
Water	67	0	10	1	**79**	85.06	14.94
Vegetation	1	55	13	11	**79**	69.32	30.68
Bare ground	15	16	39	9	**79**	49.28	50.72
Built-up	3	14	10	52	**79**	66.40	33.60
TOTALS	**85**	**85**	**72**	**74**	**316**		
UA %	78.61	64.52	54.23	71.02			
EC %	21.39	35.48	45.77	28.98			
Overall accuracy	67.51						
Overall kappa	0.57						

Table A2 Random forest multi-class classification on K5 confusion matrix.

	Water	Vegetation	Bare ground	Built-up	TOTALS	PA %	EO %
Water	53	2	20	4	**79**	66.58	33.42
Vegetation	6	33	16	24	**79**	41.38	58.62
Bare ground	25	15	26	12	**79**	33.06	66.94
Built-up	4	24	11	40	**79**	50.58	49.42
TOTALS	**88**	**74**	**73**	**80**	**316**		
UA %	59.65	43.89	35.63	49.93			
EC %	40.35	56.11	64.37	50.07			
Overall accuracy	47.90						
Overall kappa	0.31						

Table A3 Random forest multi-class classification on S1-MT confusion matrix.

	Water	Vegetation	Bare ground	Built-up	TOTALS	PA %	EO %
Water	69	0	9	1	**79**	87.34	12.66
Vegetation	1	57	13	8	**79**	72.43	27.57
Bare ground	12	17	45	5	**79**	57.13	42.87
Built-up	3	8	7	61	**79**	77.47	22.53
TOTALS	**85**	**82**	**74**	**75**	**316**		
UA %	81.22	69.70	61.12	81.50			
EC %	18.78	30.30	38.88	18.50			
Overall accuracy	73.60						
Overall kappa	0.65						

Table A4 Decision trees multi-class classification on S1-MT confusion matrix.

	Water	Vegetation	Bare ground	Built-up	TOTALS	PA %	EO %	
Water	60	2	12	4	**79**	76.49		23.51
Vegetation	2	46	19	12	**79**	58.42		41.58
Bare ground	12	19	38	9	**79**	48.34		51.66
Built-up	5	12	9	53	**79**	67.35		32.65
TOTALS	**79**	**79**	**79**	**79**	**316**			
UA %	76.68	58.13	48.18	67.74				
EC %	23.32	41.87	51.82	32.26				
Overall accuracy	62.65							
Overall kappa	0.50							

Table A5 KNN multi-class classification on S1-MT confusion matrix.

	Water	Vegetation	Bare ground	Built-up	TOTALS	PA %	EO %
Water	65	2	11	1	**79**	81.65	18.35
Vegetation	4	57	14	4	**79**	71.76	28.24
Bare ground	18	22	34	4	**79**	42.83	57.17
Built-up	4	19	9	47	**79**	59.11	40.89
TOTALS	**91**	**100**	**68**	**57**	**316**		
UA %	70.97	56.61	49.45	82.58			
EC %	29.03	43.39	50.55	17.42			
Overall accuracy	62.65						
Overall kappa	0.50						

Table A6 SVM multi-class classification on S1-MT confusion matrix.

	Water	Vegetation	Bare ground	Built-up	TOTALS	PA %	EO %
Water	65	1	12	1	**79**	82.03	17.97
Vegetation	1	56	16	7	**79**	70.71	29.29
Bare ground	10	17	46	6	**79**	58.11	41.89
Built-up	4	12	7	56	**79**	70.83	29.17
TOTALS	**79**	**86**	**81**	**70**	**316**		
UA %	81.87	65.18	56.53	80.03			
EC %	18.13	34.82	43.47	19.97			
Overall accuracy	70.42						
Overall kappa	0.61						

Table A7 C-SVM multi-class classification on S1-MT confusion matrix.

	Water	Vegetation	Bare ground	Built-up	TOTALS	PA %	EO %
Water	66	1	11	1	**79**	83.44	16.56
Vegetation	2	57	15	5	**79**	72.12	27.88
Bare ground	14	17	43	5	**79**	54.23	45.77
Built-up	4	11	8	56	**79**	70.81	29.19
TOTALS	**86**	**85**	**78**	**68**	**316**		
UA %	76.94	66.84	55.27	82.78			
EC %	23.06	33.16	44.73	17.22			
Overall accuracy	62.65						
Overall kappa	0.50						

Table A8 Random forest binary-water classification on S1 confusion matrix.

	Water	Non-water	TOTALS	PA %	EO %
Water	72	7	**79**	91.44	8.56
Non water	9	70	**79**	88.65	11.35
TOTALS	**81**	**77**	**158**		
UA %	88.96	91.19			
EC %	11.04	8.81			
Overall accuracy	90.93				
Overall kappa	0.80				

Table A9 Random forest binary-water classification on K5 confusion matrix.

	Water	Non-water	TOTALS	PA %	EO %
Water	65	14	**79**	81.97	18.03
Non water	16	63	**79**	79.25	20.75
TOTALS	**81**	**77**	**158**		
UA %	79.80	81.46			
EC %	20.20	18.54			
Overall accuracy	80.61				
Overall kappa	0.61				

Table A10 Random forest binary-water classification on S1-MT confusion matrix.

	Water	Non-water	TOTALS	PA %	EO %
Water	73	6	**79**	93.02	6.98
Non water	9	70	**79**	88.84	11.16
TOTALS	**82**	**76**	**158**		
UA %	89.29	92.71			
EC %	10.71	7.29			
Overall accuracy	90.04				
Overall kappa	0.82				

Table A11 Decision trees binary-water classification on S1-MT confusion matrix.

	Water	Non-water	TOTALS	PA %	EO %
Water	68	11	**79**	86.58	13.42
Non water	10	69	**79**	86.73	13.27
TOTALS	**79**	**79**	**158**		
UA %	86.71	86.60			
EC %	13.29	13.40			
Overall accuracy	86.65				
Overall kappa	0.73				

Table A12 KNN binary-water classification on S1-MT confusion matrix.

	Water	Non-water	TOTALS	PA %	EO %
Water	69	10	**79**	86.81	13.19
Non Water	11	68	**79**	85.79	14.21
TOTALS	**79.805**	**78.195**	**158**		
UA %	85.94	86.68			
EC %	14.06	13.32			
Overall accuracy	86.30				
Overall kappa	0.73				

Table A13 SVM binary-water classification on S1-MT confusion matrix.

	Water	Non-water	TOTALS	PA %	EO %
Water	71	8	**79**	89.69	10.31
Non water	9	70	**79**	88.96	11.04
TOTALS	**80**	**78**	**158**		
UA %	89.04	89.61			
EC %	10.96	10.39			
Overall accuracy	89.33				
Overall kappa	0.79				

Table A14 C-SVM binary-water classification on S1-MT confusion matrix.

	Water	Non-water	TOTALS	PA %	EO %
Water	72	7	**79**	91.35	8.65
Non water	10	69	**79**	86.99	13.01
TOTALS	**82.443**	**75.557**	**158**		
UA %	87.53	90.95			
EC %	12.47	9.05			
Overall accuracy	89.17				
Overall kappa	0.78				

APPENDIX B

Supplementary material for Chapter 4 (Confusion matrices for Experiment 3).

B1 2016-2017

Table B1 2016-2017 VH Tsai confusion matrix.

	No Change	Change	TOTALS	PA %	EO %
No Change	38	12	**50**	76.00	24.00
Change	11	39	**50**	78.00	22.00
TOTALS	**49**	**51**	**100**		
UA %	77.55	80.00			
EC %	22.45	23.53			
Overall accuracy	77.00				
Overall kappa	0.54				

Table B2 2016-2017 VH Otsu confusion matrix.

	No Change	Change	TOTALS	PA %	EO %
No Change	36	14	**50**	72.00	28.00
Change	9	41	**50**	82.00	18.00
TOTALS	**45**	**55**	**100**		
UA %	80.00	74.55			
EC %	20.00	25.45			
Overall accuracy	77.00				
Overall kappa	0.54				

Table B3 2016-2017 VV Tsai confusion matrix.

	No Change	Change	TOTALS	PA %	EO %
No Change	47	3	**50**	94.00	6.00
Change	18	32	**50**	64.00	36.00
TOTALS	**65**	**35**	**100**		
UA %	72.31	91.43			
EC %	27.69	8.57			
Overall accuracy	79.00				
Overall kappa	0.58				

Table B4 2016-2017 VV Otsu confusion matrix.

	No Change	Change	TOTALS	PA %	EO %
No Change	36	14	**50**	72.00	28.00
Change	19	31	**50**	62.00	38.00
TOTALS	**55**	**45**	**100**		
UA %	65.45	68.89			
EC %	34.55	31.11			
Overall accuracy	67.00				
Overall kappa	0.34				

B2 2017-2018

Table B5 2017-2018 VH Tsai confusion matrix.

	No Change	Change	TOTALS	PA %	EO %
No Change	45	5	**50**	90.00	10.00
Change	15	35	**50**	70.00	30.00
TOTALS	**60**	**40**	**100**		
UA %	75.00	87.50			
EC %	25.00	12.50			
Overall accuracy	80.00				
Overall kappa	0.60				

Table B6 2017-2018 VH Otsu confusion matrix.

	No Change	Change	TOTALS	PA %	EO %
No Change	43	7	**50**	86.00	14.00
Change	12	38	**50**	76.00	24.00
TOTALS	**55**	**45**	**100**		
UA %	78.18	84.44			
EC %	21.82	15.56			
Overall accuracy	81.00				
Overall kappa	0.62				

Table B7 2017-2018 VV Tsai confusion matrix.

	No Change	Change	TOTALS	PA %	EO %
No Change	46	4	**50**	92.00	8.00
Change	24	26	**50**	52.00	48.00
TOTALS	**70**	**30**	**100**		
UA %	65.71	86.67			
EC %	34.29	13.33			
Overall accuracy	72.00				
Overall kappa	0.44				

Table B8 2017-2018 VV Otsu confusion matrix.

	No Change	Change	TOTALS	PA %	EO %
No Change	42	8	**50**	84.00	16.00
Change	16	34	**50**	68.00	32.00
TOTALS	**58**	**42**	**100**		
UA %	72.41	80.95			
EC %	27.59	19.05			
Overall accuracy	76.00				
Overall kappa	0.52				

B3 2018-2019

Table B9 2018-2019 VH Tsai confusion matrix.

	No Change	Change	TOTALS	PA %	EO %
No Change	46	4	**50**	92.00	8.00
Change	11	39	**50**	78.00	22.00
TOTALS	**57**	**43**	**100**		
UA %	92.00	90.70			
EC %	19.30	9.30			
Overall accuracy	85.00				
Overall kappa	0.70				

Table B10 2018-2019 VH Otsu confusion matrix.

	No Change	Change	TOTALS	PA %	EO %
No Change	36	14	**50**	72.00	28.00
Change	3	47	**50**	94.00	6.00
TOTALS	**39**	**61**	**100**		
UA %	92.31	77.05			
EC %	7.69	22.95			
Overall accuracy	83.00				
Overall kappa	0.65				

Table B11 2018-2019 VV Tsai confusion matrix.

	No Change	Change	TOTALS	PA %	EO %
No Change	47	3	**50**	94.00	6.00
Change	16	34	**50**	68.00	32.00
TOTALS	**63**	**37**	**100**		
UA %	74.60	91.89			
EC %	25.40	8.11			
Overall accuracy	81.00				
Overall kappa	0.62				

Table B12 2018-2019 VV Otsu confusion matrix.

	No Change	Change	TOTALS	PA %	EO %
No Change	38	12	**50**	90.48	24.00
Change	4	46	**50**	79.31	8.00
TOTALS	**42**	**58**	**100**		
UA %	76.00	92.00			
EC %	9.52	20.69			
Overall accuracy	84.00				
Overall kappa	0.68				

B4 2016-2019

Table B13 2016-2019 VH Tsai confusion matrix.

	No Change	Change	TOTALS	PA %	EO %
No Change	40	10	**50**	80.00	20.00
Change	19	31	**50**	62.00	38.00
TOTALS	**59**	**41**	**100**		
UA %	67.80	75.61			
EC %	32.20	24.39			
Overall accuracy	71.00				
Overall kappa	0.42				

Table B14 2016-2019 VH Otsu confusion matrix.

	No Change	Change	TOTALS	PA %	EO %
No Change	33	17	**50**	66.00	34.00
Change	9	41	**50**	82.00	18.00
TOTALS	**42**	**58**	**100**		
UA %	78.57	70.69			
EC %	21.43	29.31			
Overall accuracy	74.00				
Overall kappa	0.48				

Table B15 2016-2019 VV Tsai confusion matrix.

	No Change	Change	TOTALS	PA %	EO %
No Change	42	8	**50**	84.00	16.00
Change	27	23	**50**	46.00	54.00
TOTALS	**69**	**31**	**100**		
UA %	60.87	74.19			
EC %	39.13	25.81			
Overall accuracy	65.00				
Overall kappa	0.30				

Table B16 2016-2019 VV Otsu confusion matrix.

	No Change	Change	TOTALS	PA %	EO %
No Change	37	13	**50**	74.00	26.00
Change	14	36	**50**	72.00	28.00
TOTALS	**51**	**49**	**100**		
UA %	72.55	73.47			
EC %	27.45	26.53			
Overall accuracy	73.00				
Overall kappa	0.45				

APPENDIX C

Supplementary material for Chapter 4 (Statistical significance for Experiment 3).

Table C1 Area under the curve statistics of the overall accuracy for Tsai and Otsu thresholding.

	VH TSAI	VH OTSU	VV TSAI	VV OTSU	MEAN (μ)	STD DEV (σ)
OA average	78.25	78.75	74.25	75.00	76.56	2.27
z-value	0.74	0.96	-1.02	-0.69		
Area (probability)	0.77	0.83	0.46	0.25		

Table C2 Area under the curve statistics of the kappa for Tsai and Otsu thresholding.

	VH TSAI	VH OTSU	VV TSAI	VV OTSU	MEAN (μ)	STD DEV (σ)
Kappa Average	0.57	0.57	0.49	0.50	0.53	0.05
z-value	0.78	0.94	-1.00	-0.72		
Area (probability)	0.78	0.83	0.16	0.24		

Table C3 Area under the curve statistics of the overall accuracy for each time period.

	2016-2017	2017-2018	2018-2019	2016-2019	MEAN (μ)	STD DEV (σ)
OA average	75.00	77.25	83.25	70.75	76.56	5.21
z-value	-0.30	0.13	1.28	-1.12		
Area (probability)	0.39	0.55	0.90	0.13		

Table C4 Area under the curve statistics of the kappa for each time period.

	2016-2017	2017-2018	2018-2019	2016-2019	MEAN (μ)	STD DEV (σ)
Kappa Average	0.50	0.55	0.66	0.41	0.53	0.10
z-value	-0.29	0.19	1.25	-1.15		
Area (probability)	0.39	0.58	0.89	0.13		